

UiO : **University of Oslo**

Helle Bakke

Impact of nanoflare heating in the lower solar atmosphere

Thesis submitted for the degree of Philosophiae Doctor

Institute of Theoretical Astrophysics
Faculty of Mathematics and Natural Sciences

Rosseland Centre for Solar Physics



2023

© **Helle Bakke, 2023**

*Series of dissertations submitted to the
Faculty of Mathematics and Natural Sciences, University of Oslo
No. 2670*

ISSN 1501-7710

All rights reserved. No part of this publication may be
reproduced or transmitted, in any form or by any means, without permission.

Cover: UiO.
Print production: Graphic center, University of Oslo.

“An expert is a person who has made all the mistakes that can be made in a very narrow field.”
–Niels Bohr

Abstracts

English abstract

Understanding the mechanisms responsible for the extremely high temperatures of the corona is a major challenge in solar physics. One of the leading candidates is called the nanoflare heating mechanism. Nanoflares are small-scale heating events associated with magnetic reconnection in the solar atmosphere. The nanoflare heating mechanism is based on the theory that small-scale reconnection events contribute to heating through their frequent occurrence. Even though nanoflares are energetic events, the energy released is below the detection threshold of current instrumentation and observational evidence is still lacking. This thesis focuses on the analysis of nanoflares in one-dimensional (1D) and three-dimensional (3D) numerical simulations, and investigates how small-scale heating events leave observable signatures in the lower atmosphere.

During magnetic reconnection, electrons are accelerated to non-thermal energies and travel along the magnetic field where they lose energy through interactions with the ambient plasma. Heating occurs at the sites where the electron energy is deposited, which further leads to changes in parameters such as temperature, velocity, and density. The atmospheric response to heating gives rise to signatures in the spectral lines forming at the sites where energy is deposited, but also at the heights of large gradients in temperature and velocity. In this thesis, we focus on chromospheric spectra that are readily accessible by ground-based telescopes, and investigate the diagnostic potential for the presence and properties of nanoflares through analysis of synthetic spectra in numerical simulations.

Our results show that the atmospheric response to low-energy electrons produce large gradients in temperature and velocity, giving rise to significant signatures in the synthetic spectra. A comparison of our numerical results to an observation of a small-scale coronal heating event reveals both differences and similarities between the synthetic and observed spectra. Through analysis of the observed flare profiles, we find a correlation between the Doppler shift and width of the profiles. Based on the results from our numerical models, this correlation implies that there is a presence of low-energy non-thermal electrons in the flaring loops. The analysis of this work suggests that chromospheric lines in the visible can be used as diagnostics of nanoflares in the solar atmosphere.

Norsk sammendrag

Hvorfor er temperaturen i solas korona flere millioner grader når overflaten bare er noen tusen grader? Det å forstå mekanismene som er ansvarlige for den ekstreme temperaturen i koronaen er en stor utfordring i solfysikk. En av de ledende kandidatene er oppvarming via nanobluss, som er små, energirike begivenheter assosiert med magnetisk gjentilkobling i solas atmosfære. Denne mekanismen er basert på teorien om at magnetisk gjentilkobling på liten skala, altså nanobluss, bidrar til oppvarmingen av koronaen ettersom de forekommer jevnlig i solas atmosfære. Selv om nanobluss er energirike begivenheter frigjøres det ikke nok energi til at de kan oppdages med nåværende instrumenter, og direkte observasjoner av nanobluss mangler fremdeles. Denne avhandlingen fokuserer på å analysere nanobluss i endimensjonale (1D) og tredimensjonale (3D) numeriske simuleringer, og utforsker hvordan små, energirike begivenheter fører til observerbare signaturer i solas nedre atmosfære.

Under magnetisk gjentilkobling akselereres elektroner til ikke-termiske energier, og denne energien frigjøres gjennom kollisjoner med plasma i omgivelsene når elektronene beveger seg langs magnetfeltet. Oppvarming oppstår som et resultat av den frigjorte energien, og fører til endringer i blant annet temperatur, hastighet og tetthet. Atmosfærens respons til oppvarmingen gir opphav til signaturer i spektrallinjene som dannes ved de høydene der energien frigjøres, men også ved høyder der gradientene i temperatur og hastighet er store. I denne avhandlingen tar vi for oss spektrallinjer som dannes i kromosfæren og som kan observeres av bakkebaserte teleskoper, og utforsker det diagnostiske potensialet for tilstedeværelsen og egenskapene til nanobluss gjennom analyse av syntetiske spektrallinjer.

Resultatene våre viser at atmosfærens respons til akselererte elektroner med lav energi produserer store gradienter i temperatur og hastighet som gir opphav til signaturer i de syntetiske spektrallinjene. En sammenligning av resultatene fra de numeriske modellene våre og et observert bluss av liten skala avslører både forskjeller og likheter mellom de syntetiske og observerte spektrallinjene. Gjennom analyse av spektrallinjene fra blusset finner vi en korrelasjon mellom Dopplershift og linjebredde. Basert på resultatene fra simuleringene våre impliserer denne korrelasjonen en tilstedeværelse av ikke-termiske elektroner med lav energi i de magnetiske løkkene som er assosiert med blusset. Analysen som er gjennomført i denne avhandlingen gir grunn til å tro at spektrallinjer som dannes i kromosfæren, og som er befinnet seg i den synlige delen av det elektromagnetiske spekteret, kan brukes som diagnostikk av nanobluss i solas atmosfære.

Preface

The Sun is a spherical ball of hot plasma centred in our solar system. It is a main sequence star that produces energy in its core by converting hydrogen into helium via the process of nuclear fusion, and the energy is transported to the surface by the process of either radiation or convection. The solar atmosphere is located outside the visible surface of the Sun. It is divided into the photosphere, chromosphere, transition region, and corona, where each atmospheric layer has different properties such as temperature and density. The solar corona is continuously studied through observations and numerical modelling because its temperatures are magnitudes higher than that of the lower atmosphere. It is widely accepted that the corona is heated by processes connected to the magnetic field, and one of the proposed heating mechanisms is related to small-scale reconnection events in the solar atmosphere.

Instabilities in the magnetic field can cause the field lines to reconnect, releasing energy in bursts called solar flares. Solar flares range from small brightenings to large, violent events, and are categorised based on the amount of energy released. Large flares are confined to active regions of the Sun, which vary with the solar cycle, and are too rare to consistently heat the corona to millions of degrees. Small-scale reconnection events are more frequent as they also occur outside of active regions, and heating by nanoflares is one of the prime candidates in understanding the coronal temperatures. The general consensus is that flare energy is transported by electrons from the thermal background that are accelerated to non-thermal energies during magnetic reconnection. As the electrons travel along the magnetic field, energy is transferred to the ambient plasma through Coloumb collisions. This gives rise to observable signatures in spectral lines that form in the sites where the non-thermal electrons deposit their energy. These signatures are generally found in spectra from hard X-ray observations of active regions, but observations of small-scale events with nanoflare energies are rare because the signatures are typically below the detection threshold. Due to the limited accessibility of hard X-ray studies of small-scale events, the distribution and properties of nanoflares in the solar atmosphere remain poorly understood.

This thesis focuses on the study and analysis of nanoflares in simulations, and how small-scale reconnection events leave observable signatures in the lower atmosphere. I begin with an introduction to the Sun in Chapter 1, giving a brief overview of the solar interior and the properties of the solar atmosphere. I end the chapter with a note on the heating of the upper atmosphere before moving on to Chapter 2, where I introduce solar flares and the nanoflare heating mechanism. I give an overview of the physical properties related to nanoflares, and explain the difficulties in observing small-scale reconnection events. This

is followed by Chapter 3, where I introduce the simulations that are central to this work, and put the nanoflare heating mechanism in a numerical perspective. Finally in Chapter 4, I provide a summary of the papers that form the basis for this thesis.

This thesis is submitted in partial fulfillment of the requirements for the degree of *Philosophiae Doctor* at the University of Oslo. The research presented here was conducted at the Rosseland Centre for Solar physics, which is a part of the Institute of Theoretical Astrophysics at the University of Oslo, under the supervision of professor Luc Rouppe van der Voort and professor Boris V. Gudiksen. This research was supported by the Research Council of Norway, project numbers 250810 and 325491, and through its Centres of Excellence scheme, project number 262622. Computational resources have been provided by Sigma2 – the National Infrastructure for High-Performance Computing and Data Storage in Norway.

Acknowledgements

What a long, strange trip it has been. I started my academic journey almost ten years ago, and naively thought I could study astrophysics without ever having seen an integral or knowing what a vector was. In addition, I remember stating to my friends and family that I wanted to study astrophysics to avoid programming. Understatement of the century, right? I have to admit that after the first few weeks of University, all I wanted was to quit. Luckily, I found a group of friends that helped me with my shortcomings, and their friendship and encouragement made me continue on the academic path. My family also largely contributed to me sticking to my plan of *at least* getting a Bachelor's degree, and I am so grateful that they did. During my sixth semester at the University, I was introduced to the topic of solar physics and knew that this was what I wanted to pursue. Now, a-few-too-many years later, I am about to finish my Ph.D. in solar physics, and it honestly feels a bit surreal. That said, I would never have been able to finish this thesis without all the amazing people around me, and would like to express my gratitude to those who have helped me along this journey.

First, I would like to thank my supervisor, Luc. I am grateful for every advice and suggestion that has pushed me in the right direction. Your attention to detail is impeccable, and I am glad that we share the value of a good figure. Presenting results has been particularly important to me, and it has been nice to know that you find it just as important. Thank you for the fruitful discussions about the research of this thesis, and for your excellent guidance and supervision. It has been a pleasure working with you.

Thanks are also due to my co-supervisor, Boris. Your guidance with Bifrost has been indispensable. I also appreciate the advice you have given me about work, but also about work-life balance. When you helped me structure my days during the pandemic, I felt a weight lift off my shoulders. You also told me that work is not everything, and that it is important to rest. For that, I am truly thankful.

I would like to thank Mats for our discussions about simulations and radiative transfer that have helped me understand the basis of this work. You have been the absolute best boss, and I am grateful that you included me to the RoCS environment and let me be a part of a truly rewarding work place.

Sweetest Benedikte, I am so grateful to have you in my life and to call you my friend. You have helped me through the rough times, but also been there to experience the joy of this work with me. Thank you for always taking the time to chat with me, and for having my back.

Room 216! Becca, Sneha, Øystein, Nicolas, and Frederik – thank you for our chats about everything and nothing, for creating an environment where we can

Acknowledgements

help and support each other, and for making me laugh everyday. Without you, work would not have been as fun.

A huge thank you to Renate and Becca. We have become close friends over the past few years, and I have appreciated sharing this journey with you. I have especially enjoyed our pancake breakfasts, which have acted as a therapy session in periods of frustration, but also as an outlet for fun and relaxation (which often times have been desperately needed). Our trip to Italy was so much fun, and I cannot wait to make more happy memories with you.

Thank you also to my closest friend, Helene. We met at the beginning of University, and I am eternally grateful for the friendship we have created over the past ten years. Ever since I embarked on this journey, you have cheered me on and given me reasons to continue. Even though our academic paths have diverged, you have made sure to share your love and support by suggesting “iskaffepause” whenever we are both at the University. You are one of my biggest supporters, and I am so thankful to have you in my life.

I would also like to thank my family for their constant support and encouragement during my education. Thank you, pappa, for endless conversations about motors and birds and fruit trees. Thank you, Trond and Anette, for feeding me coffee and snacks every time I stop by. Thank you, Robin, for the constant support along the way. You know how fun, exciting, difficult, and painful this process can be, and I have appreciated your tips and tricks to make it all easier. I would also like to thank Kjersti, for constantly feeding me cat images to put a smile on my face every day.

Finally, I want to thank Aleksander for being a constant in my life. You are my rock. Thank you for listening to all the joy and frustration this work has brought me, and for believing in me even though I have felt like giving up. I want to thank you for everything you have done for me, especially in these last few months – from coffee and food to “forced” breaks that have been much needed. Your love and kindness is unmatched, and I am forever grateful for you. Elsker deg.

• **Helle Bakke**

Oslo, September 2023

List of papers

Paper I

Chromospheric emission from nanoflare heating in RADYN simulations

Helle Bakke, Mats Carlsson, Luc Rouppe van der Voort, Boris V. Gudiksen, Vanessa Polito, Paola Testa, and Bart De Pontieu

In: *Astronomy & Astrophysics*. Vol. 659, no. 186 (2022)

DOI: 10.1051/0004-6361/202142842

arXiv: 2201.11961

Paper II

Accelerated particle beams in a 3D simulation of the quiet Sun.

Lower atmospheric spectral diagnostics

Helle Bakke, Lars Frogner, Luc Rouppe van der Voort, Boris V. Gudiksen, and Mats Carlsson

In: *Astronomy & Astrophysics*. Vol. 675, no. 103 (2023)

DOI: 10.1051/0004-6361/202346765

arXiv: 2306.02752

Paper III

High Resolution Observations of the Low Atmospheric Response to Small Coronal Heating Events in Active Regions

Paola Testa, Helle Bakke, Luc Rouppe van der Voort, and Bart De Pontieu

Accepted for publication in *The Astrophysical Journal*

arXiv: 2308.15417

Publications not included in this thesis

- **Non-thermal electrons from solar nanoflares. In a 3D radiative MHD simulation**
Helle Bakke, Lars Frogner, and Boris V. Gudiksen
In: *Astronomy & Astrophysics*. Vol. 620, no. L5 (2018)
DOI: 10.1051/0004-6361/201834129
arXiv: 1811.12404
- **Accelerated particle beams in a 3D simulation of the quiet Sun**
Lars Frogner, Boris V. Gudiksen, and Helle Bakke
In: *Astronomy & Astrophysics*. Vol. 643, no. A27 (2020)
DOI: 10.1051/0004-6361/202038529
arXiv: 2005.14483

Contents

| | |
|---|-----------|
| Abstracts | iii |
| Preface | v |
| Acknowledgements | vii |
| List of papers | ix |
| Publications not included in this thesis | xi |
| Contents | xiii |
| List of figures | xv |
| 1 The Sun | 1 |
| 1.1 The solar interior | 1 |
| 1.2 The solar atmosphere | 2 |
| 1.3 Heating of the upper atmosphere | 7 |
| 2 The nanoflare heating mechanism | 11 |
| 2.1 Brief introduction to solar flares | 11 |
| 2.2 Heating of the upper atmosphere by nanoflares | 13 |
| 2.3 Detecting nanoflares | 14 |
| 3 Simulating nanoflares | 19 |
| 3.1 Modelling of the nanoflare energy distribution | 19 |
| 3.2 Numerical models | 20 |
| 3.3 Synthetic observables | 26 |
| 4 Summary and outlook | 33 |
| Bibliography | 37 |
| Papers | 44 |
| I Chromospheric emission from nanoflare heating in RADYN simulations | 45 |
| II Accelerated particle beams in a 3D simulation of the quiet Sun. | |
| Lower atmospheric spectral diagnostics | 61 |
| | xiii |

**III High Resolution Observations of the Low Atmospheric
Response to Small Coronal Heating Events in Active Regions 79**

List of figures

- 1.1 High-resolution wide-band image observed on 25 May, 2017 with the Swedish 1-m Solar Telescope on La Palma, Spain, showing the distinct granulation pattern that visually defines the lower photosphere. The bright points between the granules are sites of strong magnetic fields. Courtesy of Luc Rouppe van der Voort. 2

- 1.2 Simple illustration of how the solar magnetic field is generated through the global solar dynamo model. The inner and outer circles represent the tachocline and solar surface, respectively. The differential rotation of the Sun converts poloidal field to toroidal field that is stored at the tachocline region. Turbulence in the toroidal field produces magnetic loops in the poloidal plane. The right-most figure shows a large-scale poloidal field. The figure is re-used from Bakke 2018. 3

- 1.3 Stratification of the average quiet Sun temperature from the VAL semi-empirical model. The region up to 525 km forms the photosphere, while the chromosphere ranges from 525 km up to around 2000 km and is marked by the gradual increase in temperature. The steep increase in temperature from 2000 km is called the transition region, and represents the transition from the chromosphere to the corona. The million-degree corona extends far beyond the height range shown in this figure. The horizontal bars indicate the approximate formation heights of a few spectral lines that are central to this thesis. The figure is inspired by the famous quiet Sun temperature distribution figure in Vernazza, Avrett, and Loeser 1981, and is made using the atmospheric parameters for VAL Model C. 4

| | | |
|-----|---|----|
| 1.4 | Coordinated observations of an active region on 26 June, 2022 with the Swedish 1-m Solar Telescope (SST; top row), the Interface Region Imaging Spectrograph (IRIS; bottom left), and the Atmospheric Imaging Assembly on board the Solar Dynamics Observatory (AIA; bottom right). The observations are taken at different wavelengths, where the emission is dependent on temperature. The emitted light therefore originates from different heights in the atmosphere, and each panel aims to represent different parts of the atmosphere: the photosphere (Ca II 8542Å wide-band), chromosphere (Ca II 8542Å line core), transition region (IRIS/SJI 1400Å), and corona (AIA 171Å). The AIA 171Å panel includes insets of the SST and IRIS fields of view seen as the green and blue boxes, respectively. The bottom panels are on a logarithmic scaling. SST images are courtesy of Luc Rouppe van der Voort. IRIS and AIA images are courtesy of Jonas Thoen Faber. | 6 |
| 2.1 | Standard model of a solar flare where reconnection happens at the top of a coronal loop. As the magnetic field lines reconnect, electrons are accelerated to non-thermal energies. They travel along the loop towards the footpoints, where the impact with the ambient plasma through Coloumb collisions gives rise to hard X-rays. Hot plasma fills the flaring loops through the process of evaporation, and soft X-rays are emitted as a result of particles interacting with the high-temperature plasma. The figure is adapted from similar flare cartoons in the literature. | 12 |
| 2.2 | Observation of a microflare on 4 September 2016. A hot loop of more than 7 MK is visible as the bright area in the SDO/AIA 94Å channel (green background image), while the SDO/AIA 171Å channel (yellow inset) shows the active region with hot, magnetic loops filled with plasma just below 1 MK. The small impact region is shown in fine detail in the image taken with the Swedish 1-m Solar Telescope (grey inset) on La Palma. The figure was created as an outreach activity for the European Solar Telescope: “The Science of EST” (see https://est-east.eu/the-science-of-est). . . | 17 |
| 3.1 | Electron energy distributions for different values of E_C with fixed total energy of the electron beam and spectral index $\delta = 7$. The figure aims to illustrate the difference in power-law distributions of electron beams dominated by low-energy (5 keV), intermediate-energy (10–15 keV), and high-energy (20–25 keV) electrons. . . . | 20 |

| | | |
|-----|---|----|
| 3.2 | Simple sketch of the RADYN setup for flare modelling. The loop is modelled as a quarter circle, and assumed symmetric around the apex. The electron beam is injected at the top of the loop, assuming this is where magnetic reconnection, and hence also the flare, is occurring. The radiative transfer is calculated for a 1D atmosphere along z | 22 |
| 3.3 | Temperature (solid) and electron number density (dashed) for two different initial loop conditions in RADYN simulations from Politto et al. 2018 and Paper I. The half-loop length is 15 Mm, and the initial temperatures and electron densities are aimed at reproducing active region loops at different heating stages. The 1 MK loop represents an empty strand where heating has not yet occurred, while the 3 MK loop represents a previously heated loop with higher density that is filled with hot plasma. | 23 |
| 3.4 | Reconnection factor K in a vertical cross-section at $y = 10.65$ Mm in the 3D Bifrost simulation from Paper II. The figure is inspired by Fig. 3 in Frogner, Gudiksen, and Bakke 2020. | 25 |
| 3.5 | Atmospheric response to low-energy ($E_C = 5$ keV) and high-energy ($E_C = 15$ keV) electrons in two of the RADYN simulations from Paper I. These models have a spectral index $\delta = 7$ and fixed electron energy flux. The top and bottom panels show the evolution of temperature and vertical velocity in the two models, respectively, where each time step is represented by the individual colours in the colourbar. Negative velocities correspond to plasma flows directed up towards the loop apex, while positive velocities correspond to flows directed downwards. The figure illustrates the difference in the atmospheric response to electrons depositing their energy at coronal heights (5 keV) and electrons that are able to penetrate deeper into the atmosphere and deposit their energy in the lower regions (15 keV). Note the large difference in velocity from the y -axes in the bottom panels. | 28 |
| 3.6 | Atmospheric response to nanoflare heating in RADYN using an input atmosphere extracted from a Bifrost simulation. From left to right, the top panels show the temperature and vertical velocity while the bottom panels show the electron number density and electron beam heating rate. The negative velocities correspond to upward motion of plasma, while positive velocities correspond to downflows. In this experiment, the spectral index was set to $\delta = 4$, the low-energy cutoff was set to $E_C = 2.8$ keV, and the electron energy flux was extracted from the Bifrost code and varies for each time step. The electron beam was continuously injected for the entire time series, where each colour of the colourbar represents the individual time steps. | 29 |

| | | |
|-----|---|----|
| 3.7 | Synthetic Mg II k, Ca II H, Ca II 854.2 nm, H α , and H β chromospheric lines from the RADYN simulations in Paper I. The solid and dotted lines represent the loops with temperatures of 1 MK and 3 MK, respectively. The line profiles are shown at different stages throughout the flare, namely during the pre-heating ($t = 0$ s), heating ($t = 7$ s), and post-heating ($t = 15$ s) phases. | 30 |
| 3.8 | Intensity formation of Si IV 139.4 nm at a specific location in the Bifrost simulation from Paper II. Multiplication of the first three panels produces the contribution function in the bottom right panel. The quantities are given in the top left corners, and they are shown in greyscale as functions of frequency from line centre (in units of Doppler offset) and atmospheric height. The $\tau_\nu = 1$ height (purple solid), which represents the formation height of the line, and vertical velocity (red dotted) are displayed in all panels. Negative velocities correspond to upflows, while positive velocities correspond to downflows. The S_ν panel also shows the source function at $v_D = 0$ (yellow dashed) and Planck function (green dashed) in units of brightness temperature. The Si IV 139.4 nm intensity profile (pink dashed) is shown in units of brightness temperature in the C_{I_ν} panel. | 32 |
| 4.1 | Spectral evolution of H α from one of the RADYN simulations in Paper I and from an SST observation of a small coronal heating event that is the subject of Paper III. The top panels show intensity maps of the SST/CHROMIS Ca II K line core at an instance in time during the flare, where the orange crosses represent three different locations at which the H α spectrum is taken. The bottom panels show the spectral evolution of H α , where the line profile is indicated at a specific time during the flare (marked along the y -axis). The time step for the RADYN simulation is chosen at 7 s, while the time step for the observation is chosen at 6.8 min which is the same time as the intensity maps in the top panels are shown. We note that the duration of the simulated flare is much shorter compared to the observed flare, as can be seen from the y -axis in the bottom panels. | 35 |

Chapter 1

The Sun

1.1 The solar interior

The solar interior is divided into three regions, namely the core, the radiative zone, and the convection zone. Energy generated by nuclear fusion in the core is transported by radiative diffusion across the radiative zone, which stretches from $0.25R_{\odot}$ to $0.7R_{\odot}$ (where R_{\odot} is the radius of the Sun). The photons are continuously absorbed and (re-)emitted, and because of the high density (especially at the bottom of the radiative zone), the mean free path of the photons is only a few millimetres. In fact, it takes approximately 170 000 years for the photons to travel through the radiative zone. When the photons reach the convection zone, the temperature has dropped from seven million to two million Kelvin. At this temperature, the opacity increases due to the formation of neutral hydrogen and helium (which were otherwise fully ionised in the radiative zone) as well as partially ionised heavier elements. Heat gets trapped, and as the temperature gradient increases, the plasma becomes unstable and starts to convect. This convection process transports energy via rising plasma cells. The plasma cells cool down when they reach the surface, leaving an observable pattern of hot, bright cells surrounded by cool, dark lanes. This pattern is called granulation, and is shown in Figure 1.1.

1.1.1 Magnetic field

The Sun's magnetic field is responsible for everything from sunspots and solar flares to space weather and the interplanetary magnetic field. The generation and interior structure of the solar magnetic field is not yet understood, but a popular theory is known as the global solar dynamo. The solar magnetic field changes dramatically in a cyclical manner, indicating that it is continuously generated within the Sun. For the global solar dynamo model to be successful, it has to explain the 11-year solar cycle in which coronal loops, solar flares, ejections of solar material, and the number and size of sunspots fluctuate in a synchronised manner from active to quiet to active again. The global solar dynamo is believed to be located at the bottom of the convection zone, in a region referred to as the tachocline. The plasma in the convection zone consists of electrically charged particles that move around due to convective motions, generating magnetic fields through Ampere's law. In turn, the magnetic fields generate electric fields through Faraday's law. To put it simply, the Sun will continue to generate magnetic fields as long as this loop is not interrupted. However, complicated plasma flows are needed in order for the magnetic field to be generated. The complicated flows are obtained through the solar differential rotation, which is demonstrably an important ingredient in global solar dynamo

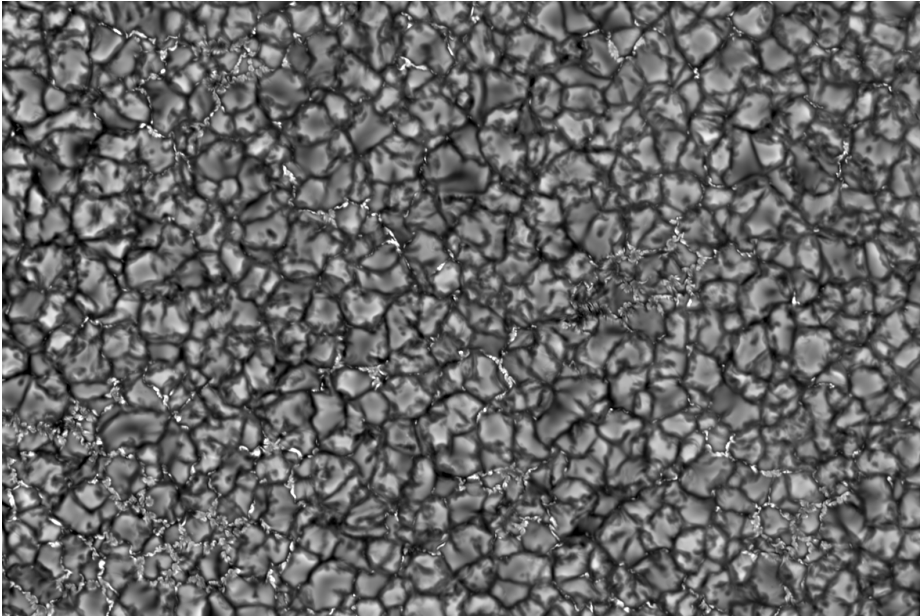


Figure 1.1: High-resolution wide-band image observed on 25 May, 2017 with the Swedish 1-m Solar Telescope on La Palma, Spain, showing the distinct granulation pattern that visually defines the lower photosphere. The bright points between the granules are sites of strong magnetic fields. Courtesy of Luc Rouppe van der Voort.

theory. Because the solar rotation is faster at the equator than at the poles, poloidal magnetic fields (aligned from north to south or south to north) are transformed into toroidal magnetic fields (aligned from east to west or west to east) by the differential rotation. The re-conversion from toroidal to poloidal fields is not yet understood, but a theory is that the toroidal field is shredded by convection as it rises to the surface, generating a poloidal field. An illustration of the global solar dynamo can be seen in Figure 1.2.

1.2 The solar atmosphere

The solar atmosphere hosts a variety of physical phenomena that are continuously studied in order to understand its properties. The atmosphere is defined as the part of the Sun from which photons can escape, and consists of three layers with different properties such as temperature, density, and optical depth. For simplicity, the solar atmosphere can be seen as a stratified region where the layers are bound to specific height ranges and the physical conditions change smoothly (see Figure 1.3). In reality, the solar atmosphere is highly dynamic in space and time, and the different atmospheric layers are not confined to a specific

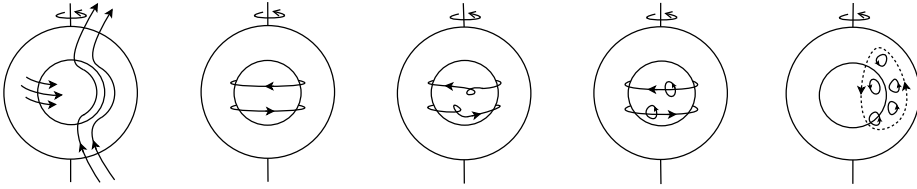


Figure 1.2: Simple illustration of how the solar magnetic field is generated through the global solar dynamo model. The inner and outer circles represent the tachocline and solar surface, respectively. The differential rotation of the Sun converts poloidal field to toroidal field that is stored at the tachocline region. Turbulence in the toroidal field produces magnetic loops in the poloidal plane. The right-most figure shows a large-scale poloidal field. The figure is re-used from Bakke 2018.

height range. Temperature and density are continuously changing as hot and cold plasma moves through the atmosphere through different physical processes. Another way to depict the boundaries between the different atmospheric layers is through plasma beta, which is defined as

$$\beta = \frac{P_g}{B^2/2\mu_0}. \quad (1.1)$$

Plasma beta (β) is the ratio between gas pressure, P_g , and magnetic pressure, $B^2/2\mu_0$. As the equation states, when $\beta > 1$ the gas pressure dominates the magnetic pressure, and when $\beta < 1$ the magnetic pressure dominates. In more extreme cases, the ratio can become either very small or very large. If $\beta \ll 1$, the magnetic field dominates the plasma motion, and if $\beta \gg 1$, the magnetic field is moved with the bulk plasma flow. To put it simply, this means that either the plasma follows the magnetic field, or the magnetic field follows the plasma. Consequently, plasma beta provides insight into the plasma properties, and hence the properties of the different atmospheric layers.

1.2.1 The photosphere

The photosphere is the innermost layer of the solar atmosphere. It can be regarded as the solar surface, at least when observed in visible light. Its name originates from Ancient Greek, where *photos* means light and *sphaira* means sphere, essentially referencing a light-emitting, spherical surface. The photosphere is the densest layer of the solar atmosphere, and emits most of the solar radiation. According to the VAL model (Vernazza, Avrett, and Loeser 1981) in Figure 1.3, the photosphere is approximately 500 km thick, with a temperature around 6600 K at the bottom and a minimum temperature around 4300 K at roughly 525 km above the surface. Here, the surface is defined as the height where the optical depth, τ , equals to unity at the reference wavelength 500 nm. Optical depth is a measure of the extent to which radiation is blocked or free to travel along the line of sight.

1. The Sun

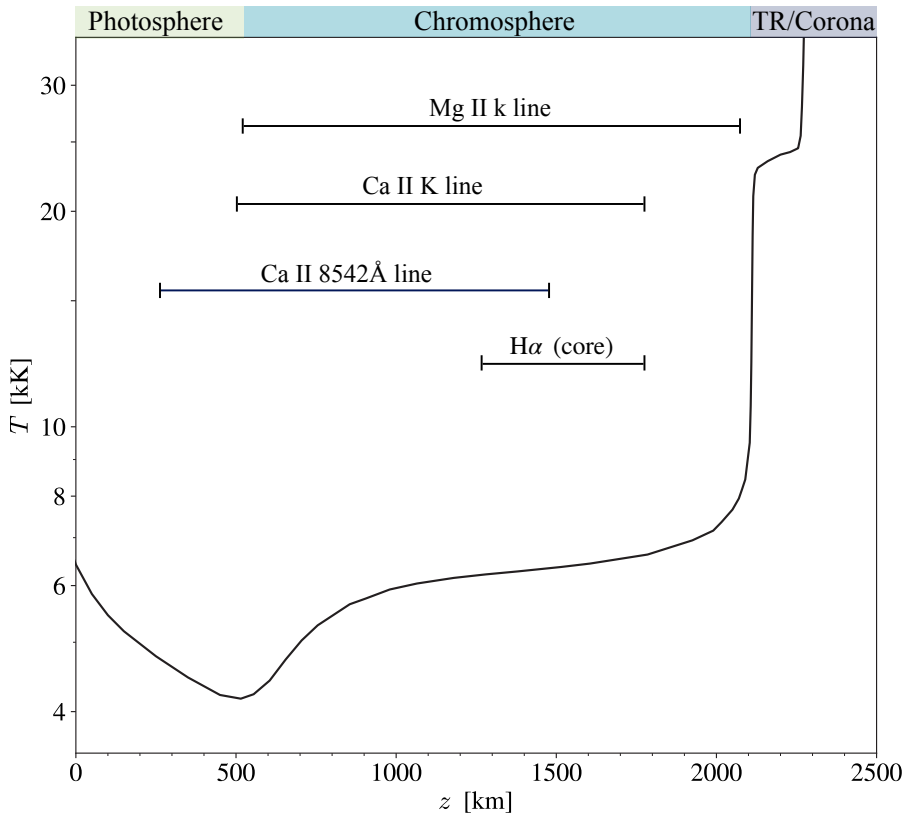


Figure 1.3: Stratification of the average quiet Sun temperature from the VAL semi-empirical model. The region up to 525 km forms the photosphere, while the chromosphere ranges from 525 km up to around 2000 km and is marked by the gradual increase in temperature. The steep increase in temperature from 2000 km is called the transition region, and represents the transition from the chromosphere to the corona. The million-degree corona extends far beyond the height range shown in this figure. The horizontal bars indicate the approximate formation heights of a few spectral lines that are central to this thesis. The figure is inspired by the famous quiet Sun temperature distribution figure in Vernazza, Avrett, and Loeser 1981, and is made using the atmospheric parameters for VAL Model C.

The majority of the visible surface is covered in a granulation pattern (see Figure 1.1 and the top left panel of Figure 1.4). Granules represent the top of hot plasma cells that rise from the convection zone, and they are what cause the distinct appearance of the photosphere. As the plasma cells reach the bottom of the photosphere, they expand and cool down before returning to convective stability. The centre of each granule is bright due to the hot plasma,

while the boundaries, or inter-granular lanes, are dark due to the falling, cool material (Priest 2014). The granules vary in size and brightness, and effectively contribute to the photospheric layer being non-uniform. Granular networks also host different magnetic field strengths, as magnetic flux tubes emerge from the solar interior through the photosphere. The emerging flux tubes occur on a wide range of scales, from granular magnetic loops with small fluxes to large active regions with high fluxes that dramatically alter the granulation pattern as they appear. The latter are hosts to sunspots, which are dark regions of even stronger magnetic field. The strength of the flux tubes decreases with height, causing the ratio of gas pressure to magnetic pressure (β) to vary throughout the photosphere. In the flux tubes $\beta < 1$, indicating that the magnetic field dominates the plasma motion, while in the neighbouring regions $\beta \gtrsim 1$ and the gas pressure is dominating the magnetic pressure.

1.2.2 The chromosphere

The chromosphere is the layer of the solar atmosphere that lies directly above the photosphere. The Greek word *chroma* means colour, and again including *sphaira* meaning sphere, the chromosphere can be directly translated to *coloured sphere*. The name is attributed to the bright red colour that can be observed around the disk during solar eclipses. According to the VAL model, the temperature in the lower chromosphere starts at approximately 4300 K and gradually rises to temperatures of 10^4 K at the boundary to the transition region. As the temperature slowly increases, the density decreases rapidly with height. The slow increase in temperature comes from the fact that energy transported from the photosphere to the chromosphere goes into the process of ionising the plasma rather than increasing the temperature drastically. The VAL model portrays the chromosphere as an approximately 1500 km thick homogeneous layer, but in reality the chromosphere is highly dynamic and non-uniform. A depiction of the chromosphere can be seen in the top right panel of Figure 1.4, showing the Ca II 8542Å line core in an active region.

The large decrease in density with height causes the ratio of gas pressure to magnetic pressure to vary significantly throughout the chromosphere. At the bottom of the chromosphere, the gas pressure dominates the magnetic pressure of the plasma, and $\beta > 1$. As the emerging magnetic field fans out with height, the magnetic pressure decreases. However, the rate at which the magnetic pressure declines is slower than that of the gas pressure, meaning that at some point the two will be equal, and $\beta = 1$. In the upper chromosphere, the magnetic pressure has become greater than the gas pressure, and $\beta < 1$. In addition to the transition from high to low β with height, the chromosphere also transitions from partially ionised to fully ionised and optically thick to optically thin, making it especially difficult to model.

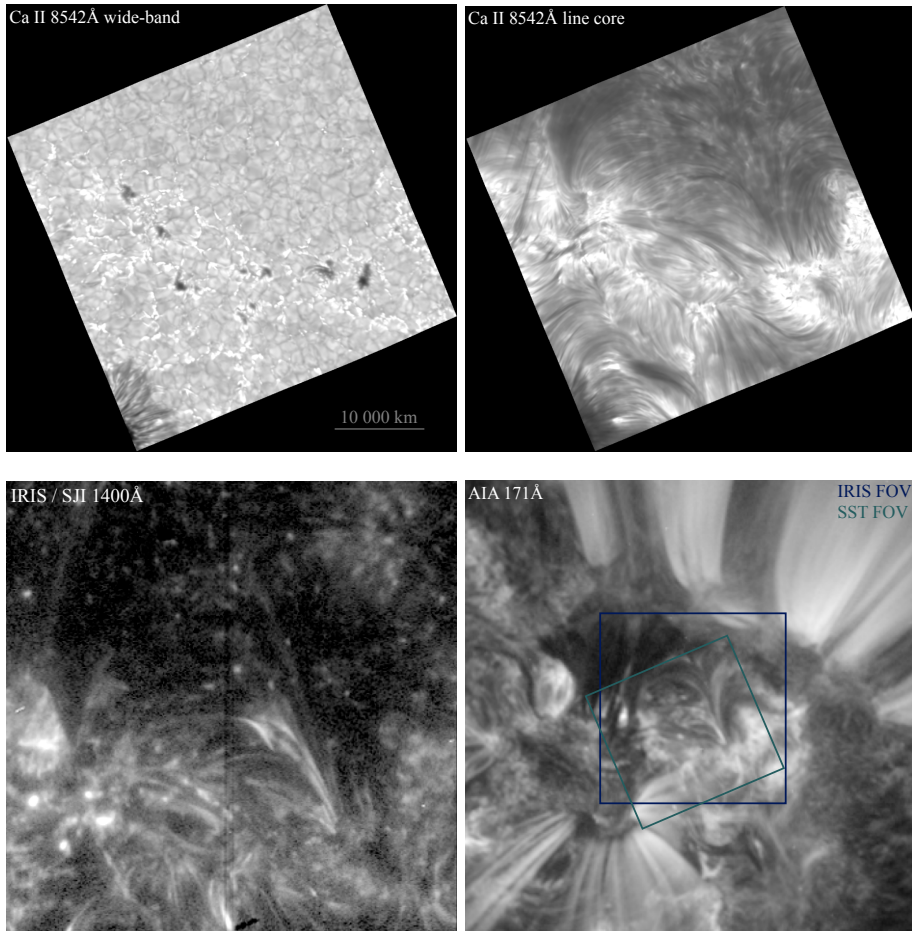


Figure 1.4: Coordinated observations of an active region on 26 June, 2022 with the Swedish 1-m Solar Telescope (SST; top row), the Interface Region Imaging Spectrograph (IRIS; bottom left), and the Atmospheric Imaging Assembly on board the Solar Dynamics Observatory (AIA; bottom right). The observations are taken at different wavelengths, where the emission is dependent on temperature. The emitted light therefore originates from different heights in the atmosphere, and each panel aims to represent different parts of the atmosphere: the photosphere (Ca II 8542Å wide-band), chromosphere (Ca II 8542Å line core), transition region (IRIS/SJI 1400Å), and corona (AIA 171Å). The AIA 171Å panel includes insets of the SST and IRIS fields of view seen as the green and blue boxes, respectively. The bottom panels are on a logarithmic scaling. SST images are courtesy of Luc Rouppe van der Voort. IRIS and AIA images are courtesy of Jonas Thoen Faber.

1.2.3 The transition region and corona

The transition region is most commonly referred to as the narrow layer between the chromosphere and corona. In reality, the transition region represents the plasma as it is being heated up or cooled down, which in turn produces a thin and irregular region where the temperature varies from around 10^4 K to somewhere on the order of 10^6 K. As the temperature increases, hydrogen and helium becomes fully ionised, while the heavier elements ionise to greater degrees. Upon reaching the corona, most of the elements are fully ionised due to the high temperature. The corona is the outermost layer of the solar atmosphere, and takes its name from the Latin word for *crown* as it can be observed during solar eclipses as a crown around the disk. It is characterised by temperatures on the order of 10^6 K, and the low density of the plasma makes the corona optically thin. The plasma motions are also completely dominated by the magnetic pressure, giving $\beta \ll 1$.

The magnetic field that emerges from the solar interior gives rise to magnetic structures that can be observed in the corona. This can be seen in Figure 1.4, where the Ca II 8542Å wide-band image shows footpoints of magnetic fields emerging through the chromosphere (Ca II 8542Å line core), transition region (IRIS/SJI 1400Å), and finally the corona (AIA 171Å). The magnetic fields can be both open and closed, each having distinct visual and structural properties in the corona. In open magnetic fields, the low temperature and concentration of plasma lead to less emission than in other parts of the corona. These features are called coronal holes, and get their name from their dark appearance. Strong closed field lines, called coronal loops, are another defining feature of the corona. Coronal loops are rooted to magnetic field footpoints of opposite polarity. They are bright structures where plasma is being heated to coronal temperatures. The most spectacular coronal loops are rooted to sunspots near the edges of active regions, but cooler loops also appear in quiet regions where the magnetic field is less strong. Coronal loops are hosts to other phenomena such as solar flares and coronal mass ejections, where flares are large energy releases caused by the reconnection of magnetic field lines that can lead to the outburst of plasma into space.

1.3 Heating of the upper atmosphere

So far, the solar interior and a brief overview of the solar atmosphere and its layers have been introduced. Before moving on, it is important to touch on the subject of chromospheric and coronal heating. Understanding the mechanisms that are responsible for heating the upper atmosphere from around 6 000 K in the photosphere to 10^4 K in the chromosphere and 10^6 K in the corona is a major challenge in the field of solar physics (see e.g. reviews by Klimchuk 2006, 2015; Reale 2014; Testa, Saar, and Drake 2015). Observations and state-of-the-art numerical models are continuously studied and compared in order to provide insight into the different heating mechanisms at work. The challenge is to find the heating mechanisms that are important in the different parts of the chromosphere

1. The Sun

and corona, as many sources of heating are most likely present simultaneously. As of now, the leading candidates are magnetohydrodynamic (MHD) waves and magnetic reconnection, both of which cause heating via dissipation. Magnetic reconnection is believed to be the most likely mechanism of coronal heating, as a variety of observations have provided evidence of reconnection in the corona such as jets, flares, and active region transient brightenings. However, reconnection is much less effective in regions where the magnetic field is weak, such as the outer corona and coronal holes. In these regions, MHD waves remain the most likely cause of heating.

There exists a variety of waves generated by processes related to the magnetic field. In particular, there is evidence that incompressible waves, such as Alfvénic waves, could be important in heating the corona (McIntosh et al. 2011; Matsumoto 2016). Unfortunately, the limited spatial and temporal resolution of current observations make it difficult to establish their contribution to the total heating of the corona. Numerical models of wave heating aim to predict signatures in the corona that can be readily observed. These models mainly revolve around resonant absorption of kink-mode waves and the subsequent heating from the dissipating wave, and Alfvén waves generated in the photosphere that dissipate as they propagate into the corona while carrying energy. However, the waves dissipate on scales much smaller than can be observed directly, and wave heating models currently remain poorly constrained by observations.

In areas of stronger magnetic fields, such as active regions, magnetic reconnection is believed to play a larger role in coronal heating. When magnetic field lines reconnect, magnetic energy is converted into kinetic energy. As the field lines are pushed closer together, current sheets are formed that store the kinetic energy which is partially converted into heat as the current sheets dissipate. Due to the complexity of the solar magnetic field, current sheets may form in many different ways before they dissipate and contribute to the heating of the upper atmosphere. Examples of current sheet formation are instabilities in the magnetostatic equilibrium, flux emergence, and braiding of coronal loops. Braiding is a fairly popular subject in the search for heating events in active regions, and while braided loops have been observed (Cirtain et al. 2013) it is uncertain how commonly heating from such events occur in the corona as direct observational evidence of heating from braiding have been difficult to obtain. Models have predicted that braiding can lead to outflowing jets of high velocity (Hansteen et al. 2015), and such jets have later been detected in cool plasma (Antolin et al. 2021). However, it is still uncertain whether or not these jets are commonly occurring in the corona. Additionally, Robinson and Carlsson 2023 suggest that braiding of magnetic field lines in the quiet Sun do not hold enough magnetic energy to transfer into jets, indicating that different heating mechanisms are most likely at works in different parts of the solar atmosphere. Another prime candidate in understanding the high temperature of the corona is the nanoflare heating mechanism (Parker 1988). This mechanism is based on the theory that small-scale reconnection events driven by braiding of the magnetic field lines occur frequently in the corona, contributing to the heating more or less constantly. The role of magnetic reconnection as a potential source of heating of

the upper atmosphere and the details of the nanoflare heating mechanism are explored in the next chapter.

Chapter 2

The nanoflare heating mechanism

2.1 Brief introduction to solar flares

Solar flares are brightenings associated with magnetic reconnection in the solar atmosphere. As field lines reconnect, magnetic energy is converted into kinetic energy and heat. The released energy is transported through the atmosphere by either thermal conduction or electrons that are accelerated to non-thermal energies from the thermal background during reconnection. As the non-thermal electrons travel along the magnetic field, energy is lost via Coulomb collisions with the ambient plasma (e.g. Brown 1971). In turn, the collisions produce radiation through bremsstrahlung (“breaking radiation”). Most of the energy is radiated by the chromosphere, where bremsstrahlung from electrostatic interactions between the electrons and the background particles produces hard X-ray (HXR) radiation. As the chromosphere is heated, it expands as the flaring loops are filled with hot plasma, increasing both temperature and density. At this point, bremsstrahlung from particles interacting with the high-temperature plasma produces soft X-ray (SXR) radiation. Figure 2.1 illustrates an idealised flare, with reconnection occurring at the top of a coronal loop (see e.g. Martens and Kuin 1989; Shibata et al. 1995). The coronal plasma eventually cools and drains back to the chromosphere, decreasing both temperature and density.

The size of solar flares are categorised based on their SXR flux. The classification includes the letters A, B, C, M, and X, with X-class flares being the largest. The released energy generally varies from about 10^{27} erg in the smallest observed events to approximately 10^{32} erg in the largest flares (although, flares of even larger thermal energy releases were predicted in Emslie et al. 2012 and Aschwanden et al. 2015). The detected SXR spectrum usually lasts for the duration of the flare due to continuous particle interactions at the top of the flaring loops. HXRs from the same event are also often detected, but while the SXR spectrum declines smoothly from its initial flare spike, the HXR spectrum often consists of a single spike that lasts significantly shorter than the duration of the event. However, not all reconnection events produce large brightenings that can be detected through X-ray observations. The HXR spectrum observed during flares can be explained by a single non-thermal electron population with a power-law distribution (Krucker, Hudson, et al. 2010). Flares of lower energies are expected to occur based on the power-law nature of the flare distribution, but they are often hidden in regions of high flaring activity. Additionally, small-scale events such as nanoflares (10^{24} – 10^{25} erg) are difficult to detect through HXR observations because signatures from the accelerated non-thermal electrons are typically below the detection threshold. Because of this, there is limited knowledge about the presence and properties of small-scale events with nanoflare

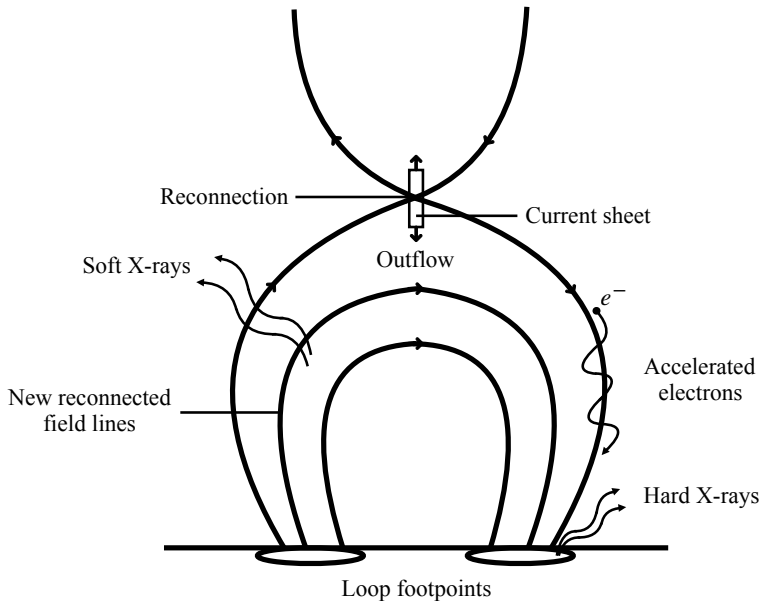


Figure 2.1: Standard model of a solar flare where reconnection happens at the top of a coronal loop. As the magnetic field lines reconnect, electrons are accelerated to non-thermal energies. They travel along the loop towards the footpoints, where the impact with the ambient plasma through Coloumb collisions gives rise to hard X-rays. Hot plasma fills the flaring loops through the process of evaporation, and soft X-rays are emitted as a result of particles interacting with the high-temperature plasma. The figure is adapted from similar flare cartoons in the literature.

energies and lower. With the general consensus that flares are associated with magnetic reconnection and that the flare distribution follows a power-law, it is possible to contribute to the understanding of small-scale events through modelling and predictions.

2.1.1 Magnetic reconnection

Magnetic reconnection is important for understanding solar flares. It is the reconfiguration of magnetic field lines in a plasma, and in solar physics it involves energy releases and acceleration of electrons to non-thermal energies. The simplest explanation of magnetic reconnection is seen in 2D, where magnetic field lines of opposite directions are pressed together. As the field lines reconnect, they spring out horizontally and create an X-type shape of the configuration (such as the one illustrated in Figure 2.1). This is called a separatrix surface, where regions of topologically different field lines are separated. In this region, where the magnetic field is being pressed together and carried into a diffusion region, a

current sheet is created that produces outflows at the ends of the current sheet. There exists a number of different 2D models that explain reconnection in flare loops fairly well, but a major drawback of these models is that 2D reconnection can only occur at an X-point. In reality, reconnection can occur at any location where magnetic gradients become large. Here, electric currents build up, creating particle acceleration sites. By definition, 3D magnetic reconnection occurs in regions where $\mathbf{E} \cdot \mathbf{B} \neq 0$. Over the years, a vast amount of 3D reconnection regimes have been proposed, but this thesis focuses mainly on the effects of reconnection rather than the mechanism itself.

2.2 Heating of the upper atmosphere by nanoflares

The nanoflare heating mechanism is based on a theory by Eugene Parker (Parker 1988) speculating that the corona is continuously heated by frequently occurring flares with energies around 10^{24} erg or less. The theory is plausible, especially considering that the solar magnetic field stretches through the entire atmosphere and that reconnection in principle can happen at any location where $\mathbf{E} \cdot \mathbf{B} \neq 0$. However, without observational proof it is difficult to validate the nanoflare heating mechanism. A reason for this is that it is challenging to correctly determine the flare energy distribution, i.e.

$$P = \int_{E_{\min}}^{E_{\max}} f(E) dE = \frac{C}{2 - \delta} [E^{2-\delta}]_{E_{\min}}^{E_{\max}}, \quad (2.1)$$

where $f(E)$ is a power-law distribution of energies, E is the energy, E_{\min} and E_{\max} are the minimum and maximum energies in the distribution, respectively, δ is the spectral index, and C is a constant. Due to the lack of observational evidence, it is difficult to determine whether the physical processes that we know are important in large flares are also relevant for smaller flares down to nanoflare scale and smaller. It is therefore uncertain whether or not nanoflares are able to efficiently accelerate electrons to non-thermal energies. It follows that nanoflares may or may not be able to heat the upper atmosphere by way of electron energy transport, hence their contributions to this heating mechanism are still largely uncertain. For the smallest flares to fit the requirement of heating the corona, the distribution must have a power-law index $\delta > 2$ such that the low-energy part of the distribution contains most of the energy (Hudson 1991). In order to properly understand the role of flares in coronal heating, it is crucial to accurately estimate the power-law index δ . However, this requires that the energy inferred from observations is accurate, which cannot always be assumed because the information can potentially be subject to errors and biases. The power-law flare distribution in Equation (2.1) also continues into the unobservable low-energy range, meaning that it is difficult to prove that nanoflares heat the upper atmosphere since it is unclear if the value of the power-law index is maintained down to the physical limit of the distribution (Hannah, Hudson, Battaglia, et al. 2011).

2. The nanoflare heating mechanism

Major effort is continuously put into investigating small-scale heating events. In particular, microflares ($\sim 10^{26}$ – 10^{28} erg) have been studied in detail with instruments such as the Reuven Ramaty High-Energy Solar Spectroscopic Imager (RHESSI; Lin et al. 2002) and the Nuclear Spectroscopic Telescope ARray (NuSTAR; Harrison et al. 2013), showing evidence of HXR non-thermal emission. This suggests that flare physics are similar across a wide range of energies, possibly also including nanoflare-sized events and smaller. Observations of microflares also provide further constraints on the power-law index of small-scale events, contributing to isolate the essential physics required to understand the properties of nanoflares. Observations of microflares with RHESSI have revealed that the spectral index δ of the non-thermal electron distribution increases with decreasing flare energy (Hannah, Hudson, Battaglia, et al. 2011). In more recent observations of microflares with NuSTAR, Glesener et al. 2020 find that the spectral index of a microflare depositing energy at a rate of $\sim 2 \cdot 10^{27}$ erg s $^{-1}$ is around 6.3 ± 0.7 , while Wright et al. 2017 find that $\delta \geq 7$ for a microflare with a heating rate of $\sim 2.5 \cdot 10^{25}$ erg s $^{-1}$ during its impulsive phase. These findings suggest that the spectral index of the non-thermal electron distribution arising from nanoflares should at least be greater than or equal to 7, but it is difficult to make a conclusion without observational proof.

Measures have also been taken to constrain the HXR emission in the quiet Sun. After all, the nanoflare heating mechanism takes root in the theory that small-scale events of nanoflare-size occur frequently in the quiet Sun. Using almost 12 days of RHESSI observations, Hannah, Hudson, Hurford, et al. 2010 have estimated the upper limits of photon flux during a period of solar cycle minimum. With their upper limits of HXR emission in the quiet Sun, they find it unlikely that nanoflares associated with non-thermal electrons are involved in the heating of the corona because it would require a steep electron energy distribution that expands to very low energies in the thermal range. New upper limits have later been investigated with observations from the Focusing Optics X-ray Solar Imager (FOXSI; Krucker, Christe, et al. 2014; Christe et al. 2016; Musset et al. 2019) sounding rocket. Buitrago-Casas et al. 2022 find that the upper limits set by the FOXSI-2 and FOXSI-3 observations are in agreement with what was found by Hannah, Hudson, Hurford, et al. 2010 but they argue that the observation time was short and that observations of low solar activity extending over months will increase the sensitivity of the emission assessment (this is also the conclusion made in Marsh et al. 2017, who searched for HXR emission in the quiet solar corona with NuSTAR). Hence HXR studies of the quiet Sun still have the opportunity to cast light on the presence and properties of nanoflares and their contribution to coronal heating.

2.3 Detecting nanoflares

Detecting small-scale events is not a straight forward task. In larger flares, more magnetic energy is converted into kinetic energy that is transferred to the electrons, meaning that energy deposited on impact with the ambient plasma

is larger. More energetic electrons therefore lead to stronger signatures that can be detected through HXR observations. As previously mentioned, HXR observations of nanoflares are difficult to obtain because the signatures from the non-thermal electrons are below the detection threshold. HXR observations of nanoflares are therefore currently not available. In order to gain insight on the effects of small-scale events, it is possible to look for signatures of non-thermal electrons in spectral lines forming at the heights where the electron energy is deposited. In an ideal coronal nanoflare event, electrons are accelerated to non-thermal energies at the top of a coronal loop. Energy is then transported to the lower atmosphere by the non-thermal electrons as they travel along the loop. The travelling electrons are usually referred to as an electron beam, which has a non-thermal energy distribution as in Equation (2.1). As the electrons travel along the magnetic field, they deposit energy through collisions with the ambient plasma. High-energy electrons usually penetrate deeper into the atmosphere before depositing their energy, while low-energy electrons usually deposit their energy in the corona. In either case, the effects arising from the deposited energy should in principle leave an observable signature in the spectra forming at the heights subject to heating by the electrons. These effects will be discussed in more detail in Chapter 3, but in short (and put very simply) they entail an atmospheric response to the heating that affects the formation of the spectral lines.

Unfortunately, it is still problematic to obtain signatures of nanoflares directly from the corona. The high thermal conductivity of the corona has a tendency to smooth out temperature gradients, and hence also signatures from heating events. Instead, the transition region has become subject to observational studies because the rapid changes in temperature, density, and volume make it highly responsive to heating. Testa, De Pontieu, Martínez-Sykora, et al. 2013 have investigated the properties of moss, which is the upper transition region emission of hot active region loops, using extreme ultraviolet (EUV) imaging data of the High-resolution Coronal Imager (Hi-C; Kobayashi et al. 2014) instrument. Their results show high levels of temporal variability in the moss, with high-intensity brightenings on short (~ 15 s) time scales. They also find a correlation between the magnetic and coronal features, suggesting that the moss variability is due to reconnection in the corona and the subsequent energy release from small-scale events such as nanoflares. Even though Hi-C provides observations of the corona at very high spatial resolution (~ 200 km), it does not provide the spectral information needed to determine properties of the plasma (such as plasma flows). The Interface Region Imaging Spectrograph (IRIS; De Pontieu et al. 2014) on the other hand, provides observations of chromospheric and transition region emission at high spatial, temporal, and spectral resolution, making it possible to investigate the lower atmospheric response to heating events. Testa, De Pontieu, Allred, et al. 2014 continued their studies by investigating short-lived brightenings at the footpoints of hot loops by analysing IRIS observations together with coronal observations taken with the Atmospheric Imaging Assembly (AIA; Lemen et al. 2012) on board the Solar Dynamics Observatory (SDO; Pesnell, Thompson, and Chamberlin 2012). They find that the moss brightenings have a typical duration

2. The nanoflare heating mechanism

of 20–60 s. The overlying loops are brightening after a few minutes, indicating a clear association between the moss brightenings and heating of the loops. They also find that many of the brightenings are associated with upflows of plasma, which are indicated by negative Doppler velocities ($v_D < 0$), commonly referred to as blueshifts, of the Si IV spectra as observed with IRIS. They also compare the observed spectra with state-of-the-art numerical models (which will be discussed in more detail in the next chapter) in order to constrain the properties of nanoflares. That means comparing the observations to the numerical models and using the physical conditions (such as the different parameters going into the non-thermal electron energy distribution) of the simulated nanoflares to gain knowledge on the observed events.

A comparison between observations and simulations was also performed by Winebarger et al. 2013, who analysed a set of rapidly evolving loops in an inter-moss region observed with Hi-C and compared their findings with a three-dimensional radiative magnetohydrodynamic (MHD) simulation of the solar atmosphere. By combining the high spatial resolution of Hi-C and the multi-temperature coverage from AIA, they performed a detailed analysis of the properties of the loops such as size, life times, temperature, and density. They find that the loops consist of cool and dense plasma, and that the short life times in combination with the amount of energy radiated from the loops suggest that they are impulsively heated by nanoflares. They then move on to studying the evolution of loops in an advanced numerical simulation, and find that the high density, low temperature, and short life times of these loops are comparable to that of the Hi-C observations. Further investigation of the simulations shows that the loops occur as a result of magnetic reconnection at chromospheric or low coronal heights. Additionally, the loops tend to occur at magnetic field footpoints that are close in proximity, which is a condition that is also fulfilled in the observations. They conclude that the simulations strongly support their interpretation of cool and dense transition region loops caused by nanoflares. These findings are particularly interesting, as the numerical models used in this study, as well as the flare model mentioned above, are highly relevant since the work of this thesis evolves around the usage of both.

Figure 2.2 shows an example of a small-scale heating event occurring in an active region on 4 September 2016. The figure was created as an outreach activity for the European Solar Telescope (EST; Quintero Noda et al. 2022) and the particular event is studied and analysed in detail in Paper III. The event was also observed with IRIS, providing an excellent opportunity to investigate both the EUV and the Ca II K emission, where the latter is in the visible part of the spectrum. The combination of numerical models and observations covering a wide range of the emission spectrum is beneficial in the continued study of nanoflares and their impact on the lower atmosphere, and hence also their role in the heating of the upper atmosphere.

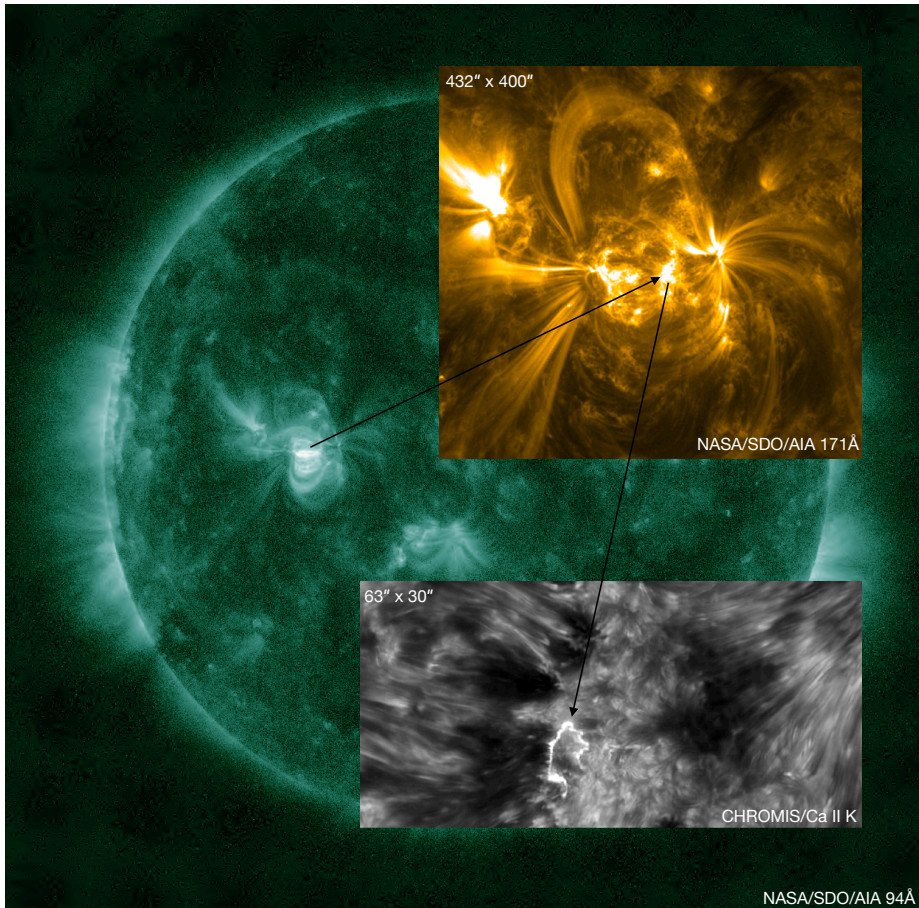


Figure 2.2: Observation of a microflare on 4 September 2016. A hot loop of more than 7 MK is visible as the bright area in the SDO/AIA 94Å channel (green background image), while the SDO/AIA 171Å channel (yellow inset) shows the active region with hot, magnetic loops filled with plasma just below 1 MK. The small impact region is shown in fine detail in the image taken with the Swedish 1-m Solar Telescope (grey inset) on La Palma. The figure was created as an outreach activity for the European Solar Telescope: “The Science of EST” (see <https://est-east.eu/the-science-of-est>).

Chapter 3

Simulating nanoflares

3.1 Modelling of the nanoflare energy distribution

The combination of observations and numerical models can be an extremely powerful tool when constraining the properties of coronal nanoflares. The lack of observational evidence makes numerical models necessary in order to understand the physical conditions of nanoflares such as the non-thermal electron energy distribution. The electrons accelerated in a solar flare have an energy distribution that follows a power-law. As described earlier, the power-law index δ might be a function of the total energy released in the flare, and for small flares the power-law index could be around 7. The accelerated electrons are produced from the thermal distribution at the flare site, so naturally there is a lower energy to the non-thermal electrons. It is generally assumed that there exists a low-energy cutoff E_C of the electron energy distribution that corresponds to the intersection between the power-law and thermal energy distributions. The increase in spectral index with decreasing flare energy was discussed in the previous chapter, and implies that the electron energy distribution should be steep for heating events of nanoflare-size. The low-energy cutoff E_C therefore becomes especially important as it represents the energy that most electrons in the distribution have. This can be seen in Figure 3.1, which shows an example of five energy distributions with different values of the low-energy cutoff E_C that represents electron beams dominated by low-, intermediate-, and high-energy electrons. The electron beams in these models have a total energy that is fixed and a large spectral index that creates a steep power-law distribution. Each distribution starts at its respective E_C value and declines exponentially with increasing energy. Most of the electrons in the low-energy distribution ($E_C = 5$ keV) have energies between 5 and 6 keV, and few electrons with energies above 9 keV. As E_C increases, there are more higher-energy electrons in the distributions, but less electrons with $E = E_C$.

The distance the accelerated non-thermal electrons travel after the simulated reconnection event is highly dependent on the spectral index δ of the energy distribution. The smaller the value of δ , the larger the distance travelled by the electrons (Allred, Kowalski, and Carlsson 2015). Consequently, larger values of δ lead to a faster rate of energy deposited in the loop. However, the rate of energy deposited in the loop also relies on the value of E_C , as low-energy electrons are more likely to lose their energy early on compared to higher-energy electrons. This means that electrons following a distribution such as the $E_C = 5$ keV case in Figure 3.1 most likely deposit their energy shortly after the reconnection event, especially when the distribution is steep due to a high spectral index, as is currently required from an observational point of view in regards to nanoflares.

Choosing the amount of electron beam energy in a simulated nanoflare

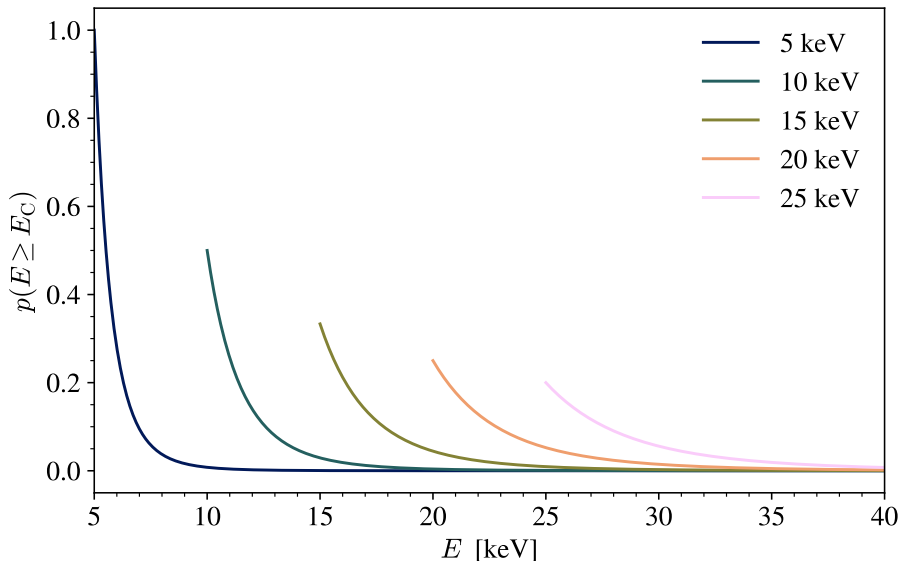


Figure 3.1: Electron energy distributions for different values of E_C with fixed total energy of the electron beam and spectral index $\delta = 7$. The figure aims to illustrate the difference in power-law distributions of electron beams dominated by low-energy (5 keV), intermediate-energy (10–15 keV), and high-energy (20–25 keV) electrons.

depends on the type of model used. The following section introduces the two different numerical models that are central to the work in this thesis. These models are vastly different, as one simulates flaring events in a one-dimensional (1D) system, while the other is a three-dimensional (3D) model that simulates a portion of the Sun ranging from the top of the convection zone to the corona. While the 3D model in principle is more realistic than the 1D model, they are both useful in determining the properties of nanoflares and contribute to the understanding of the nanoflare heating mechanism.

3.2 Numerical models

Numerical simulations are under constant development in a variety of fields, both scientific and other, and are an effective tool to investigate environments and conditions that cannot be directly physically measured in laboratory conditions. In the field of solar physics, researchers are constantly working to model the Sun as accurately and precisely as possible, preferably with three dimensions and with high spatial and temporal resolution. A major obstacle is computing power, and to keep the simulation runs manageable and within the limits of available resources, compromises are required such as reduced area of coverage,

reduced resolution, or fewer dimensions with more advanced physics, to name a few. However, not all simulations aim to compute and model the same problem. While the solar community would definitely benefit from a numerical model of the whole Sun, that is still years in the works. In the meantime, excellent state-of-the-art numerical models aimed at different physical conditions such as flares, radiative transfer, or magnetohydrodynamics are used. This section presents two numerical models with different usage that have been essential to this work, especially in Paper I and Paper II.

3.2.1 RADYN

The RADYN numerical code was developed to solve radiation transport in a 1D atmosphere (Carlsson and Stein 1992, 1995, 1997), and was later extended to include flare-accelerated particles that propagate along flux tubes and heat the atmosphere (e.g. Abbett and Hawley 1999; Allred, Hawley, et al. 2005, 2006; Cheng, Ding, and Carlsson 2010; Allred, Kowalski, and Carlsson 2015). RADYN solves the equations of charge and population conservation coupled to the non-linear equations of radiation hydrodynamics in a 1D atmosphere. The conditions are treated out of local thermodynamic equilibrium (commonly referred to as non-LTE), and the radiative transport equations are solved for the lines that dominate in the chromosphere, namely hydrogen (H), helium (He), and calcium (Ca II). Continua from other atomic species are treated in local thermodynamic equilibrium (LTE) as background metal opacities, and optically thin losses are calculated using the CHIANTI 7.1 atomic database (Dere et al. 1997). In order to resolve shocks and steep gradients in the flaring atmosphere, RADYN employs an adaptive grid (Dorfi and Drury 1987) where the grid cell sizes vary over the simulation domain and allows for a higher density of smaller grid cells in regions where this is required. This method defines a resolution operator that is strongly dependent on the absolute value of the gradients arising from the radiative hydrodynamic variables, especially temperature, velocity, and atomic level populations. These gradients can be large at different heights, and are therefore given weights since they require the most grid sensitivity. This makes it possible to properly resolve the transition region and the shocks forming in the loop, as well as the non-LTE population densities such that convergence of the radiative transfer equations is more likely to be reached.

The work in Paper I employs the version of RADYN described in Allred, Kowalski, and Carlsson 2015 to simulate nanoflares under varying conditions. This version of RADYN models flux tubes that are assumed to be symmetric around the loop apex. This means that only half of the full loop is modelled, with boundaries at one footpoint and at the loop apex. Figure 3.2 shows a simple sketch of the RADYN flare model setup. The geometry of the half-loop, which is modelled as a quarter circle, is used to vary the gravitational acceleration along the z -axis. The radiative transfer is computed along the 1D atmosphere, but is considered to be along the z -axis as the radiation emerges along the vertical direction. The spectral diagnostics of interest in this thesis are formed in the extreme lower end of the atmosphere where the loop geometry is almost

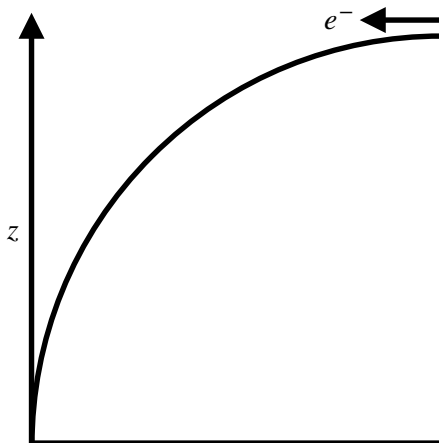


Figure 3.2: Simple sketch of the RADYN setup for flare modelling. The loop is modelled as a quarter circle, and assumed symmetric around the apex. The electron beam is injected at the top of the loop, assuming this is where magnetic reconnection, and hence also the flare, is occurring. The radiative transfer is calculated for a 1D atmosphere along z .

vertical (see Figure 3.2), hence the assumption of the radiation emerging along z is not too bad. The non-thermal electrons are injected at the top boundary, following from the idealised flare scenario where reconnection happens at the top of coronal loops. The distribution of flare-accelerated particles is calculated using the Fokker–Planck equations coupled with the results from the radiative transfer, and the electron beam spectrum follows a power-law that takes energy flux, spectral index, and low-energy cutoff as input values. RADYN allows for flare modelling in an isolated system, which is beneficial when trying to determine the effects of the non-thermal electrons. As such, the user is able to specify a large variety of input parameters in order to create a particular flaring environment. The initial loop conditions, such as temperature, density, and loop length, determines the initial atmosphere (see Figure 3.3). The cross-sectional area of the loop contributes to determining the electron beam energy flux through

$$F = \frac{E}{At}, \quad (3.1)$$

where F is the flux, E is the total energy deposited in the loop, A is the cross-section of the loop, and t is the duration of the heating event. With RADYN, it is possible to recreate certain conditions as inferred from observations to either reproduce or predict the impact the non-thermal electrons have on the solar atmosphere.

RADYN flare simulations are central to the work in Paper I, and build upon the research in Testa, De Pontieu, et al. 2014, Polito et al. 2018, and Testa,

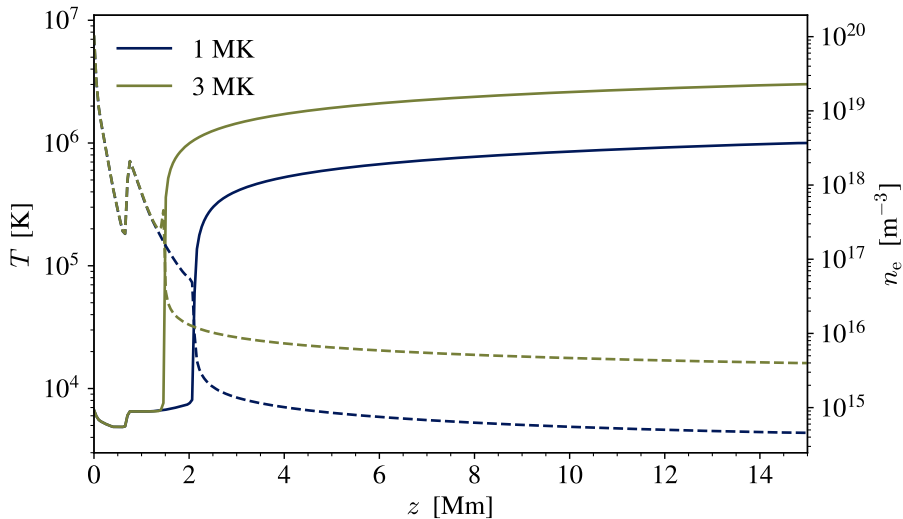


Figure 3.3: Temperature (solid) and electron number density (dashed) for two different initial loop conditions in RADYN simulations from Polito et al. 2018 and Paper I. The half-loop length is 15 Mm, and the initial temperatures and electron densities are aimed at reproducing active region loops at different heating stages. The 1 MK loop represents an empty strand where heating has not yet occurred, while the 3 MK loop represents a previously heated loop with higher density that is filled with hot plasma.

Polito, and De Pontieu 2020. Common for their work is that the RADYN flare simulations have loop heating times that are consistent with IRIS observations of transition region moss showing that short-lived footpoint brightenings have life times of about 10–30 s. While their parameter survey is quite extensive and consisting of a variety of models with either heating by non-thermal electrons or thermal conduction, or hybrid models with both, the study in Paper I is limited to focus only on heating by non-thermal electrons in the shortest (15 Mm) loops. This is because the loop length (or rather half-loop length) is comparable to that of the loops in the following 3D model that is subject to the work in Paper II.

3.2.2 Bifrost with non-thermal electron beams

Bifrost is a radiative magnetohydrodynamic (MHD) code that models a region of the solar atmosphere in three dimensions (Gudiksen et al. 2011). It solves the resistive MHD partial differential equations in 3D, including radiative transfer and field-aligned thermal conduction. The details of the Bifrost code will not be discussed here, but some background of the module used in this work is necessary. As master students, Lars Frogner and myself worked on different parts of a common project related to the Bifrost code. Lars was tasked to develop a module

3. Simulating nanoflares

including a method for treating energy transport by accelerated electrons, and I was tasked to find a method for determining where magnetic field lines reconnect, and hence also the electron acceleration sites. The results were first published in Bakke, Frogner, and Gudiksen 2018, and the method was expanded upon and further discussed in Frogner, Gudiksen, and Bakke 2020 and Frogner and Gudiksen 2022.

Electrons are accelerated by electric currents that form when magnetic field lines reconnect, and the first step of the method is to locate the reconnection sites. According to Biskamp 2005, the criterion for conserving the magnetic topology is

$$\|\mathbf{B} \times (\nabla \times \mathbf{S})\| = 0, \quad (3.2)$$

where \mathbf{S} is the projection of the electric field onto the magnetic field,

$$\mathbf{S} = \left(\frac{\mathbf{E} \cdot \mathbf{B}}{\mathbf{B} \cdot \mathbf{B}} \right) \mathbf{B}. \quad (3.3)$$

Reconnection takes place if the magnetic topology is no longer conserved, or in other words, where Equation (3.2) is violated. The criterion for identifying reconnection sites can then be expressed as

$$K = \|\mathbf{B} \times (\nabla \times \mathbf{S})\| \neq 0, \quad (3.4)$$

and reconnection occurs once K exceeds a certain threshold K_{\min} . The threshold is needed because the value of K can never become exactly zero due to the numerical precision in Bifrost, and therefore every point in the simulation would be classified as a reconnection site. Figure 3.4 shows how the reconnection factor K varies in a simulated Bifrost atmosphere. K scales linearly with the magnetic field, meaning that the value of K is larger in the top of the convection zone and photosphere, and generally decreases with height. Therefore, setting the value of K_{\min} has a few implications. A low value of K_{\min} allows for the inclusion of more reconnection sites as the number of sites increases with decreasing K_{\min} , but it also means that less energetic particle distributions are produced on average. It also becomes computationally expensive to include more reconnection sites, and hence simulate more electron beams. Fortunately, the total energy in the included electron beams starts to stagnate when K_{\min} becomes very small, making it possible to choose a reasonable threshold that keeps the computational cost manageable while also including a sufficient amount of electron beams.

The next step is to determine the electron energy distribution. The low-energy cutoff E_C is calculated numerically by finding the intersection between the thermal and non-thermal energy distributions. This leads to different values of E_C for the individual electron beams that are roughly proportional to temperature. For electron beams accelerated in the corona where the temperature is around 10^6 K, the low-energy cutoff E_C is of the order of 1 keV. As with the RADYN numerical code, the spectral index δ is a free global parameter. The total non-thermal energy flux corresponds to a fraction of the magnetic energy released in a reconnection event. This fraction is taken from the energy that is otherwise

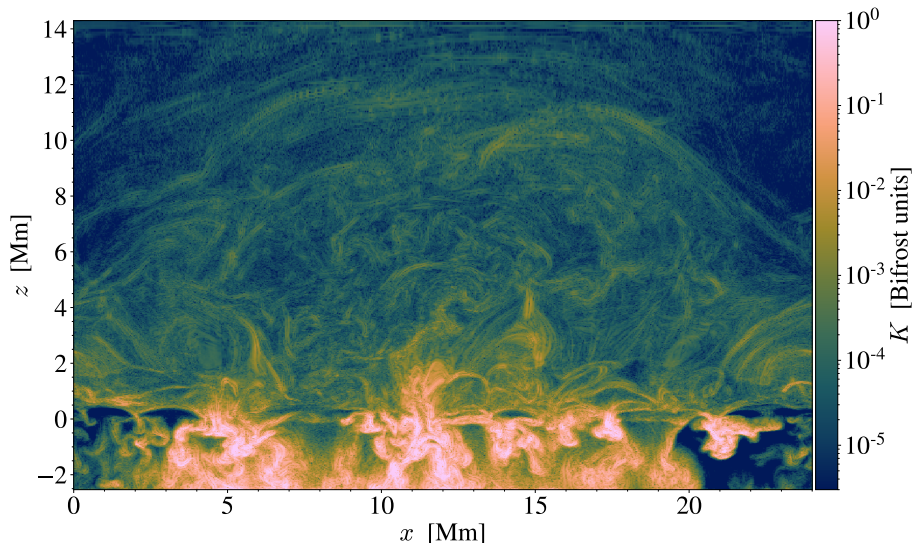


Figure 3.4: Reconnection factor K in a vertical cross-section at $y = 10.65$ Mm in the 3D Bifrost simulation from Paper II. The figure is inspired by Fig. 3 in Frogner, Gudiksen, and Bakke 2020.

converted to Joule heating in Bifrost models without accelerated electrons. The fraction is fixed, and studies of flare observations typically suggest values between 10% (Emslie, Kucharek, et al. 2004; Emslie, Dennis, et al. 2012) and 50% (Lin and Hudson 1971) of the total energy released during the flare.

The final step of the method is to trace the non-thermal electron beams as they travel along the magnetic field. As mentioned in Chapter 2, the non-thermal electrons lose energy through Coulomb collisions with the ambient plasma along the way, which in turn heats the local plasma. An in-depth description of the method, as well as the analytical expressions going into the calculation, is found in Frogner, Gudiksen, and Bakke 2020. In addition to the steps presented here, the model is also tuned to exclude short-range beams and low-energy beams. In some cases, the electrons deposit their energy immediately after reconnection. This can be due to collisions, but also if the energy transferred to the electrons is low. In both cases, the signatures of heating are evened out by other mechanisms of energy transport such as thermal conduction, plasma advection, or radiative transfer. By excluding the low-energy beams, the computational cost is reduced even further (it is already lowered by setting a suitable threshold on the reconnection factor, as mentioned above). The Bifrost simulations that have currently been run with the electron beam module (see Frogner, Gudiksen, and Bakke 2020 and Paper II) qualify as quiet, and the electron beams produced from this level of reconnection are rather weak due to the relatively low amount of energy transferred to the electrons. This

ended up being a large part of the discussion in Paper II, as there were no clear indications of the electron beams impacting the lower atmosphere significantly. Even so, the research was a step in the right direction, and serves as a guide for future Bifrost simulations including accelerated electrons.

3.3 Synthetic observables

So far, two different numerical simulations of non-thermal electron beams have been discussed. The impact the electrons have on the atmosphere can be analysed by looking at the atmospheric response to the deposited energy. From an observational perspective, flares can be detected through their emitted X-ray radiation. However, signatures from the non-thermal electrons accelerated from magnetic reconnection during the flare can be detected in spectral lines forming at the sites where the energy is deposited. This forms the basis of the work in this thesis, where nanoflare-sized heating events are investigated through numerical simulations and the impact of the non-thermal electrons are studied through the atmospheric response which further gives rise to signatures in synthetic spectral lines. In this way, numerical models can provide insight on what spectral line features to look for in observations.

3.3.1 Spectral synthesis with RH1.5D

There exists a number of numerical codes that are able to synthesise spectral profiles. The work in this thesis employs the RH1.5D radiative transfer code (Uitenbroek 2001; Pereira and Uitenbroek 2015), which solves the non-LTE radiative transport equations for spectral lines in partial redistribution (PRD). PRD is important in the synthesis of spectral lines where there is a correlation between the absorbed and re-emitted radiation, and a more accurate treatment of photon scattering is required. The observant reader may wonder why RADYN was not used for the spectral synthesis, as this also includes detailed radiative transfer. RADYN assumes complete redistribution (CRD) of the radiation, which, oppositely to PRD, means that the frequencies of the ingoing and outgoing photons are independent. This is usually a good assumption when modelling photospheric lines, but the work in this thesis is mainly focused on chromospheric spectra where PRD is generally assumed in the synthesis of Mg II h and k (Milkey and Mihalas 1974; Leenaarts et al. 2013a,b) and Ca II H and K (Vardavas and Cram 1974; Shine, Milkey, and Mihalas 1975; Bjørgen et al. 2018). RH1.5D also calculates the spectra from 1D, 2D, or 3D numerical simulations on a column-by-column basis (or in 1.5D), meaning that spectra can be synthesised from both RADYN and Bifrost simulations using the same model atoms.

The 1.5D approach is especially handy when synthesising spectra from 3D Bifrost simulations, as problematic regions can be dealt with individually through various optimisation strategies such as increasing the number of iterations or adjusting parameters so that convergence is reached. Additionally, if convergence is not reached it will not affect the neighbouring columns. This way of treating

the columns is beneficial as it makes the computation faster. In full 3D radiative transfer, a single problematic column increases the computation time as it creates a bottle neck where other columns need to wait for convergence to be reached. With the complexity of Bifrost atmospheres, RH1.5D is very well suited to handle potential columns that crash or have a hard time reaching convergence. In the spectral synthesis performed in Paper II, only about 100 out of several 100 000 columns did not converge, which is considered a great success!

3.3.2 Spectral diagnostics

The atmospheric response to the non-thermal electrons gives rise to signatures in the spectral lines that can readily be detected through observations. However, since direct signatures from nanoflare heating are difficult to determine, the aim of this thesis has been to provide guidance on future observations by analysing the impact of non-thermal electrons in synthetic spectra. The work in this thesis began as a continuation of the numerical investigation of nanoflare-heated loops in RADYN simulations by Polito et al. 2018 and Testa, Polito, and De Pontieu 2020. While they mainly focused on the upper chromospheric and transition region lines that are covered by IRIS, the work in Paper I was aimed at extending their analysis by including Ca II lines in the visible that are readily accessible by ground-based telescopes. Ground-based telescopes generally allow for higher spatial resolution compared to observations from space (this was investigated in Paper III through spatial analysis of a small-scale coronal heating event observed with both SST and IRIS), and the impact of electron beam heating on spectra forming deeper in the atmosphere was analysed in detail to hopefully expand the list of possible diagnostics for the properties of nanoflares.

The spectral diagnostics in this thesis consisted of synthesising the Mg II h and k, Ca II H and K, Ca II 854.2 nm, H α , and H β chromospheric lines, as well as the transition region Si IV resonance lines. By including a variety of spectral lines forming at different heights in the atmosphere, it is possible to study the response to the non-thermal electrons depositing their energy along the loop. When the electrons deposit their energy, the temperature and density increases. The following effects depend on the sites where the energy is deposited. The impact of the low-energy cutoff E_C in the electron energy distribution has already been discussed, in particular that low-energy electrons have shorter travel distance compared to higher-energy electrons as they more easily lose their energy through Coulomb collisions with the ambient plasma. Figure 3.5 presents the atmospheric response to low-energy and high-energy electrons in two of the RADYN models from Paper I in order to showcase the effect of the cutoff energy E_C . In the case where low-energy electrons are accelerated in the corona (left column), most of the electrons, which have energies close to E_C (see Figure 3.1), will deposit their energy at coronal heights. The increase in temperature causes an increase in pressure, which further leads to upward motions of hot plasma filling the loops. The hot plasma eventually cools, causing the plasma to flow down towards the chromosphere. Electron beams with higher-energy electrons (right column) are able to penetrate deeper into the atmosphere and deposit

3. Simulating nanoflares

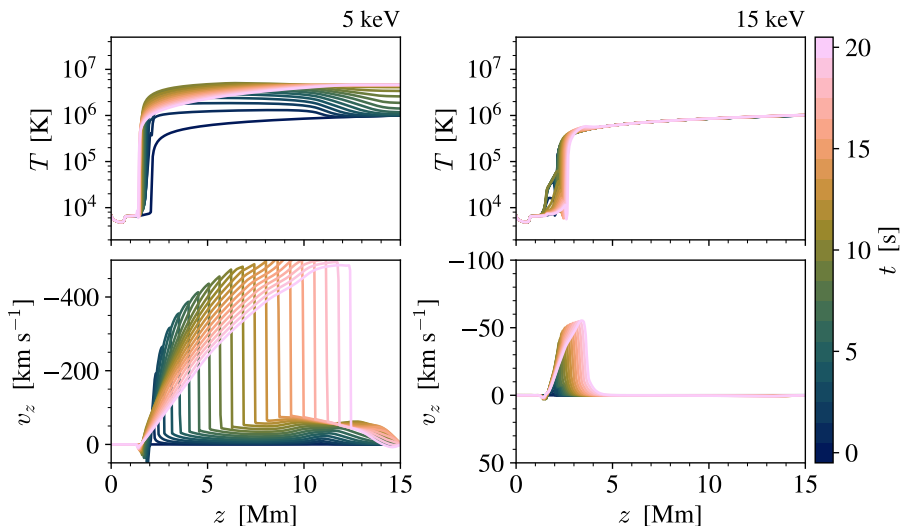


Figure 3.5: Atmospheric response to low-energy ($E_C = 5$ keV) and high-energy ($E_C = 15$ keV) electrons in two of the RADYN simulations from Paper I. These models have a spectral index $\delta = 7$ and fixed electron energy flux. The top and bottom panels show the evolution of temperature and vertical velocity in the two models, respectively, where each time step is represented by the individual colours in the colourbar. Negative velocities correspond to plasma flows directed up towards the loop apex, while positive velocities correspond to flows directed downwards. The figure illustrates the difference in the atmospheric response to electrons depositing their energy at coronal heights (5 keV) and electrons that are able to penetrate deeper into the atmosphere and deposit their energy in the lower regions (15 keV). Note the large difference in velocity from the y -axes in the bottom panels.

energy at lower heights. While the temperature increases at the site of deposited energy, the plasma is denser and harder to accelerate meaning that the upflows of hot plasma into the loops are weaker. Another low-energy case is seen in Figure 3.6, which shows an example of a RADYN flare simulation where a Bifrost atmosphere including accelerated electrons was extracted to use as input. The beam consists of low-energy electrons ($E_C = 2.8$ keV), and the energy distribution has a spectral index $\delta = 4$. The energy distribution is less steep than in the previously shown examples, but most of the electrons still deposit their energy in the corona as can be seen from the temperature (top left panel) and the beam heating rate (bottom right panel).

The formation of spectral lines are highly dependent on changes in temperature and velocity in the atmosphere. Increases in temperature usually lead to emission of the line, while strong velocity gradients contribute to shifting the line to either positive (redshift) or negative (blueshift) Doppler offsets. An

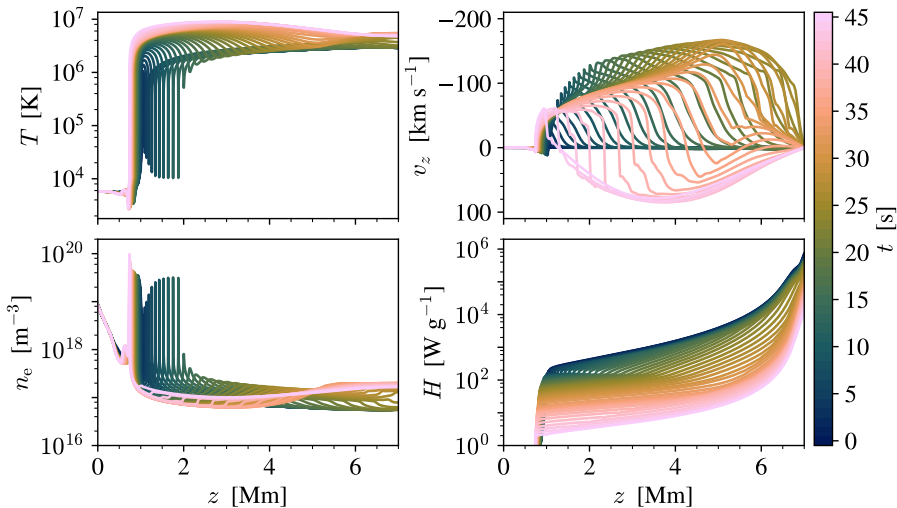


Figure 3.6: Atmospheric response to nanoflare heating in RADYN using an input atmosphere extracted from a Bifrost simulation. From left to right, the top panels show the temperature and vertical velocity while the bottom panels show the electron number density and electron beam heating rate. The negative velocities correspond to upward motion of plasma, while positive velocities correspond to downflows. In this experiment, the spectral index was set to $\delta = 4$, the low-energy cutoff was set to $E_C = 2.8$ keV, and the electron energy flux was extracted from the Bifrost code and varies for each time step. The electron beam was continuously injected for the entire time series, where each colour of the colourbar represents the individual time steps.

example of chromospheric lines synthesised from the RADYN flare simulations in Paper I can be seen in Figure 3.7. The figure shows the evolution of Mg II k, Ca II H, Ca II 854.2 nm, H α , and H β spectra from three different time steps during the flare, which cover the pre-heating (0 s), heating (7 s), and post-heating (15 s) phases. During the heating phase, most of the profiles experience an increase in emission, and the Mg II k, H α , and H β lines are redshifted to positive Doppler offsets. The shapes and features of the profiles arise as a consequence of the atmospheric response to the non-thermal electrons depositing their energy. A good way to determine which factors contribute to the line formation is by analysing the contribution function. Following Carlsson and Stein 1997, the contribution function can be calculated as

$$C_{I_\nu} \equiv \frac{dI_\nu(z)}{dz} = S_\nu \tau_\nu e^{-\tau_\nu} \frac{\chi_\nu}{\tau_\nu}. \quad (3.5)$$

The first term on the right-hand side gives the total source function S_ν , which is frequency dependent when PRD is assumed. The next term is the optical depth factor $\tau_\nu e^{-\tau_\nu}$. It represents the Eddington-Barbier part of the contribution

3. Simulating nanoflares

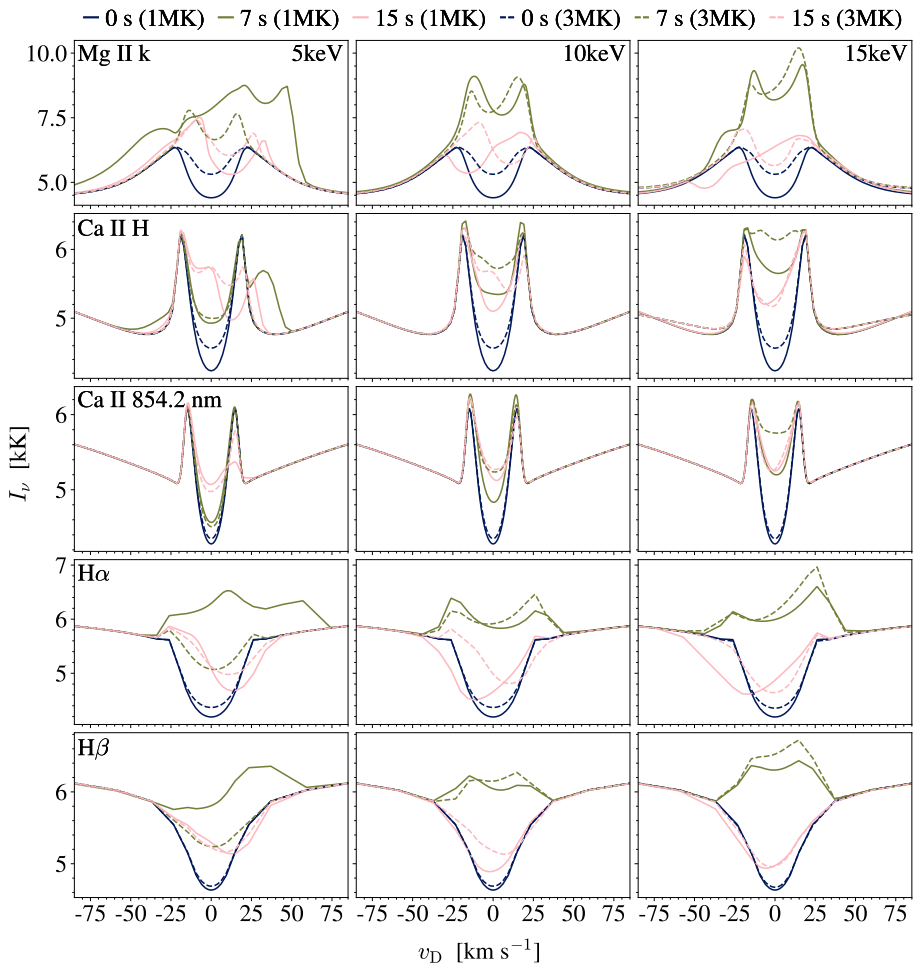


Figure 3.7: Synthetic Mg II k, Ca II H, Ca II 854.2 nm, H α , and H β chromospheric lines from the RADYN simulations in Paper I. The solid and dotted lines represent the loops with temperatures of 1 MK and 3 MK, respectively. The line profiles are shown at different stages throughout the flare, namely during the pre-heating ($t = 0$ s), heating ($t = 7$ s), and post-heating ($t = 15$ s) phases.

function, and has a maximum at $\tau_\nu = 1$. The final term χ_ν/τ_ν is the ratio of the opacity over optical depth, and is responsible for spectral line asymmetries due to its high sensitivity to velocity gradients in the atmosphere. This factor is often dominating the contribution function in the presence of strong velocity gradients as the opacity has a tendency to become large at small optical depths. The contribution to the line intensity can be further explored through the famous four-panel diagram first presented in Carlsson and Stein 1997, where the terms

of the contribution function, as well as C_{I_ν} , are presented in separate panels. An example is shown in Figure 3.8, where the formation of Si IV 139.4 nm at a location in the Bifrost simulation from Paper II is presented. The contributions to the line intensity are determined by looking at the effects occurring around the purple solid line, which is the $\tau_\nu = 1$ height (also referred to as the formation height). The interpretation of the diagram can be summarised as follows:

- The strong velocity gradient around 1.05 Mm gives a large contribution to the formation of the line (as can be seen in the C_{I_ν} panel in the bottom right), and the overall positive velocity is shifting the profile to the red (positive Doppler offset).
- The temperature increase at 1 Mm gives rise to weak emission of the line at around $+5 \text{ km s}^{-1}$, while a second temperature increase at approximately 1.45 Mm causes emission of the red peak at around $+20 \text{ km s}^{-1}$.
- The dip in temperature at around 1.75 Mm causes the relatively reduced intensity in the form of a weak dip in the profile at $+30 \text{ km s}^{-1}$.

The Si IV resonance lines were included in the work in Paper II in order to investigate potential opacity effects arising in the Bifrost simulation with accelerated electrons. The Si IV resonance lines form in the transition region, which is optically thin to most radiation, and are therefore generally assumed to form under optically thin conditions. Consequently, the emissivity can be computed without calculating the full radiative transfer. The model silicon atom from Kerr et al. 2019 was employed in the RH1.5D synthesis of the Si IV resonance lines because it includes potential opacity effects, allowing the emission to form under optically thick conditions. In an extensive parameter survey of RADYN flare simulations, Kerr et al. 2019 find that optical depth effects on the Si IV emission are significant. The resonance lines can even form under optically thick conditions for weaker flares, depending on the electron energy distribution parameters. For example, in flares where the value of E_C is large, the emission is more likely to form under optically thin conditions. Oppositely, smaller values of E_C lead to a larger fraction of the energy being deposited at higher altitudes, and in these flares optical depth effects are more likely to arise. While the model silicon atom was constructed for use on RADYN flare simulations, it was applied to the Bifrost simulation in Paper II to investigate the formation of Si IV emission in weaker flares. Even though the results show that most of the emission in the simulation is forming under optically thin conditions, Figure 3.8 shows that above 1 Mm the $\tau_\nu = 1$ curve follows the contribution function, implying that this part of the spectral line forms under optically thick conditions.

The spectral diagnostics presented in this section constitute the main method of analysis in Paper I and Paper II. As observations of nanoflares currently remain rare, analysis of synthetic spectra from numerical models such as RADYN and Bifrost grants the opportunity to provide guidance to future observations. By including spectral lines in the visible to the analysis, it is possible to expand the list of diagnostics for the presence and properties of nanoflares in the solar atmosphere.

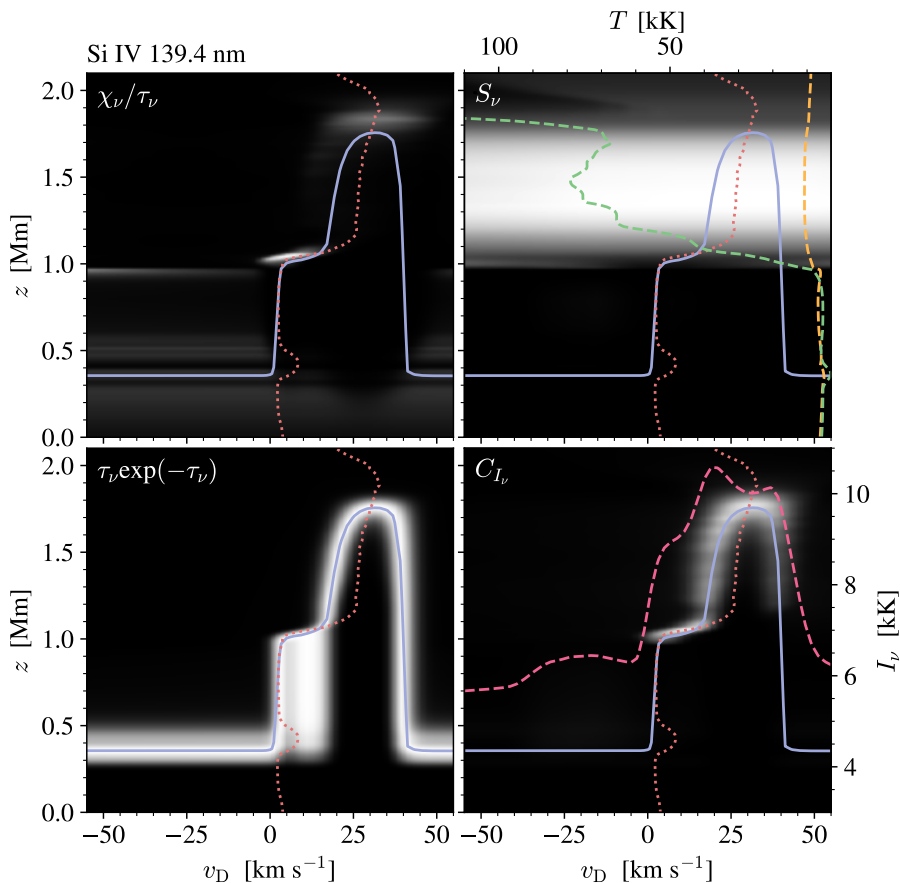


Figure 3.8: Intensity formation of Si IV 139.4 nm at a specific location in the Bifrost simulation from Paper II. Multiplication of the first three panels produces the contribution function in the bottom right panel. The quantities are given in the top left corners, and they are shown in greyscale as functions of frequency from line centre (in units of Doppler offset) and atmospheric height. The $\tau_\nu = 1$ height (purple solid), which represents the formation height of the line, and vertical velocity (red dotted) are displayed in all panels. Negative velocities correspond to upflows, while positive velocities correspond to downflows. The S_ν panel also shows the source function at $v_D = 0$ (yellow dashed) and Planck function (green dashed) in units of brightness temperature. The Si IV 139.4 nm intensity profile (pink dashed) is shown in units of brightness temperature in the C_{I_ν} panel.

Chapter 4

Summary and outlook

The results of the analysis presented in this thesis indicate that the chromospheric lines in the visible can be used as diagnostics of nanoflares. The spectral analysis generally show that the chromospheric and transition region lines are affected by variations in temperature and velocity, both in RADYN flare models (Paper I) and in the Bifrost simulation with accelerated electrons (Paper II). By starting our work in the 1D domain with RADYN flare models, we were able to study the impact of non-thermal electrons in an isolated system and get a better understanding of the potential signatures arising in the synthetic spectra as a result of nanoflare heating. We found that the models with low-energy electrons produced the most significant signatures in the spectra. This is because the electrons deposit their energy at coronal heights, causing both upward and downward motion of plasma in the loop as well as shifting of the transition region to lower heights. The combination of large velocity gradients and sudden temperature increases at the height of formation for the chromospheric spectra lead to significant Doppler shifts, line broadening, and increased emission. Signatures in the spectral profiles forming in the models with electron beams with higher-energy electrons in their distributions generally consisted of increased emission of the line. Since the electrons are able to deposit most of their energy in the lower atmosphere, the velocity gradients that arise are weaker as the chromospheric plasma is harder to accelerate. Hence the signatures in the spectral profiles were mostly affected by the increase in temperature.

We continued our work by analysing chromospheric and transition region spectra forming in Bifrost employed with the electron beam heating module. Going from 1D to 3D added more dimensions of confusion than actual physical dimensions, and it is safe to say that we struggled to find a proper method of selecting beam heating sites to analyse in detail. First, we tried to use k -means clustering to find sites of interesting spectral profiles resembling those from our RADYN analysis. This proved to be a difficult task, as the majority of profiles in the Bifrost simulation are unique, demanding a large number of clusters to properly identify the desired ones. Additionally, an extensive k -means analysis means a lot of computation time, and we finally decided to go for a more manual approach in the selection of beam heating sites. While analysis of the RADYN flare models made it relatively simple to determine the impact of the non-thermal electrons, Bifrost proved to be more challenging due the complexity of the atmospheric response in three dimensions. The evolution of temperature, vertical velocity, and electron number density revealed little about where the electrons deposit their energy as the parameters were shown along z following the vertical path of emerging radiation, and not along the magnetic field. The magnetic field in Bifrost is tangled and messy, as can be inferred

4. Summary and outlook

from Figure 3.4 showing the reconnection factor K which essentially outlines the magnetic field due to its properties. Because of the tangled mess that is the Bifrost magnetic field, it is almost impossible to determine the atmospheric response to the non-thermal electrons along z , as opposed to RADYN which models a single loop and has a known location where the electron beam is injected. We found that the spectral lines were heavily affected by shock waves passing through the atmosphere, as the subsequent oscillations in temperature caused variations in the spectra of similar magnitude, but due to the complexity of the atmospheric response the shocks could not be attributed to the non-thermal electrons. Consequently, we found that the best way of determining which factors contribute to the line formation was through analysing the contribution function. However, we were not able to make a firm conclusion about the atmospheric response to small-scale beam heating events in Bifrost and claim that specific signatures in the spectral lines were due to the accelerated electrons. Even so, the results of the analysis can still contribute to the understanding of nanoflare-sized events in the solar atmosphere.

Our work came full circle when we got the opportunity to compare the chromospheric synthetic spectra from our RADYN models to an observation of a small-scale coronal heating event (see Figure 2.2). The event was captured by both SST and IRIS, but for our contribution we analysed the chromospheric Ca II K data taken at SST. This meant that we finally got to apply k -means analysis to the observational data. We focused on clustering the spectral profiles of the flare ribbon in order to distinguish particular features such as redshifts, blueshifts, weak to no shifts, and line broadening. We used the k -means analysis to choose three locations in the flare ribbon representing regions of strong redshifts, high intensity, and blueshifts. To make things interesting, we decided to include Ca II 854.2 nm and H α observations to the comparison to our numerical results. While browsing through the synthetic spectra from the different RADYN flare models from Paper I, we found that the model with loop-top temperature of 1 MK and low-energy cutoff of 5 keV was closest in reproducing the observed spectra. In particular, the H α synthetic profile showed many similarities to the observed profile, both in shape and temporal evolution (see bottom panels of Figure 4.1). The Ca II comparisons did unfortunately not reveal many similarities, mainly because the line cores of the synthetic profiles were in absorption while the flare profiles were in emission. The only way to compare the profiles was through their Doppler shifts, and not their shapes and features. However, we found a correlation between the Doppler shift and width of the observed profiles, and based on the results from our numerical models this correlation suggests that there is a presence of non-thermal electrons with relatively low energy in the flaring loops.

The comparison of observational spectra to synthetic spectra in Paper III revealed that current numerical models generally fail to reproduce the observed chromospheric lines. It would be interesting to investigate the reason for this, especially when certain features of the flare profiles can be reproduced by the models (for example H α). Our research suggests that low-energy electrons depositing their energy at high altitudes significantly impact the chromospheric

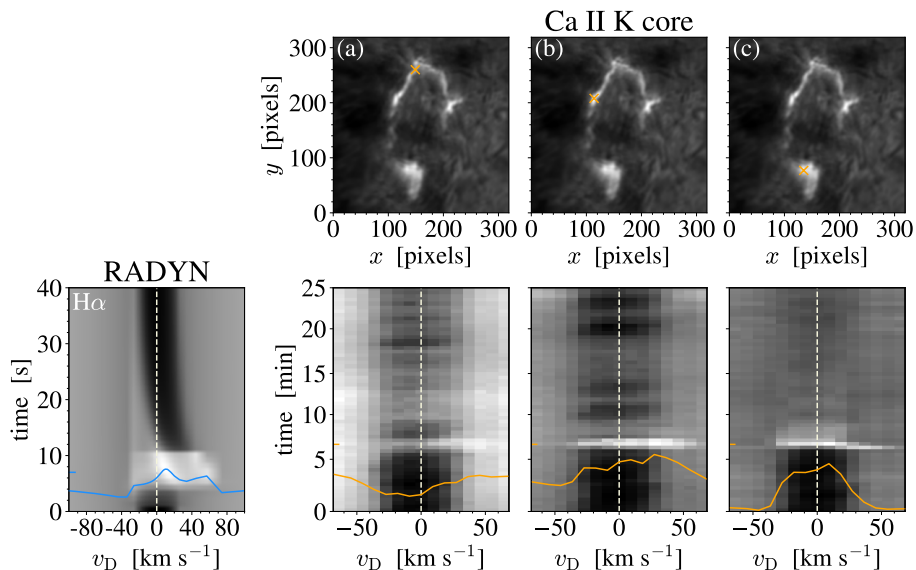


Figure 4.1: Spectral evolution of $H\alpha$ from one of the RADYN simulations in Paper I and from an SST observation of a small coronal heating event that is the subject of Paper III. The top panels show intensity maps of the SST/CHROMIS Ca II K line core at an instance in time during the flare, where the orange crosses represent three different locations at which the $H\alpha$ spectrum is taken. The bottom panels show the spectral evolution of $H\alpha$, where the line profile is indicated at a specific time during the flare (marked along the y -axis). The time step for the RADYN simulation is chosen at 7 s, while the time step for the observation is chosen at 6.8 min which is the same time as the intensity maps in the top panels are shown. We note that the duration of the simulated flare is much shorter compared to the observed flare, as can be seen from the y -axis in the bottom panels.

spectra through the atmospheric response. This was further supported by the fact that it was the low-energy electron beam RADYN model that was able to produce synthetic spectra that resembled the observed profiles the most. It would be interesting to continue to investigate the Bifrost simulation with accelerated electrons, but run for a longer period of time compared to the duration of the simulation in Paper II and with higher-energy electrons. The latter is because the low-energy cutoff values of the electron energy distributions in Bifrost are below the 5 keV cutoff in RADYN, and it would be beneficial to try to reproduce similar flaring conditions for better comparison between the models. If we were able to determine specific signatures from the non-thermal electrons in Bifrost, we could provide further guidance on observations and contribute even more to the continued understanding of nanoflare heating in the solar atmosphere.

Bibliography

- Abbett, W. P. and Hawley, S. L. (Aug. 1999). “Dynamic Models of Optical Emission in Impulsive Solar Flares”. In: *The Astrophysical Journal* vol. 521, no. 2, pp. 906–919.
- Allred, J. C., Hawley, S. L., et al. (Sept. 2005). “Radiative Hydrodynamic Models of the Optical and Ultraviolet Emission from Solar Flares”. In: *The Astrophysical Journal* vol. 630, no. 1, pp. 573–586. arXiv: [astro-ph/0507335](#) [[astro-ph](#)].
- (June 2006). “Radiative Hydrodynamic Models of Optical and Ultraviolet Emission from M Dwarf Flares”. In: *The Astrophysical Journal* vol. 644, no. 1, pp. 484–496. arXiv: [astro-ph/0603195](#) [[astro-ph](#)].
- Allred, J. C., Kowalski, A. F., and Carlsson, M. (Aug. 2015). “A Unified Computational Model for Solar and Stellar Flares”. In: *The Astrophysical Journal* vol. 809, no. 1, 104, p. 104. arXiv: [1507.04375](#) [[astro-ph.SR](#)].
- Antolin, P. et al. (Jan. 2021). “Reconnection nanojets in the solar corona”. In: *Nature Astronomy* vol. 5, pp. 54–62.
- Aschwanden, M. J. et al. (Mar. 2015). “Global Energetics of Solar Flares: II. Thermal Energies”. In: *The Astrophysical Journal* vol. 802, no. 1, 53, p. 53. arXiv: [1502.05941](#) [[astro-ph.SR](#)].
- Bakke, H., Frogner, L., and Gudiksen, B. V. (Nov. 2018). “Non-thermal electrons from solar nanoflares. In a 3D radiative MHD simulation”. In: *Astronomy & Astrophysics* vol. 620, L5, p. L5.
- Bakke, H. (2018). “Acceleration of High-Energy Electrons by Magnetic Reconnection in Coronal Nanoflares”. MA thesis. University of Oslo, Institute of Theoretical Astrophysics.
- Biskamp, D. (2005). *Magnetic Reconnection in Plasmas*.
- BjØrgen, J. P. et al. (Mar. 2018). “Three-dimensional modeling of the Ca II H and K lines in the solar atmosphere”. In: *Astronomy & Astrophysics* vol. 611, A62, A62. arXiv: [1712.01045](#) [[astro-ph.SR](#)].
- Brown, J. C. (July 1971). “The Deduction of Energy Spectra of Non-Thermal Electrons in Flares from the Observed Dynamic Spectra of Hard X-Ray Bursts”. In: *Solar Physics* vol. 18, no. 3, pp. 489–502.
- Buitrago-Casas, J. C. et al. (Sept. 2022). “The faintest solar coronal hard X-rays observed with FOXSI”. In: *Astronomy & Astrophysics* vol. 665, A103, A103. arXiv: [2205.04291](#) [[astro-ph.SR](#)].
- Carlsson, M. and Stein, R. F. (Sept. 1992). “Non-LTE Radiating Acoustic Shocks and CA II K2V Bright Points”. In: *The Astrophysical Journal Letters* vol. 397, p. L59.

- Carlsson, M. and Stein, R. F. (Feb. 1995). “Does a Nonmagnetic Solar Chromosphere Exist?” In: *The Astrophysical Journal Letters* vol. 440, p. L29. arXiv: [astro-ph/9411036](#) [[astro-ph](#)].
- (May 1997). “Formation of Solar Calcium H and K Bright Grains”. In: *The Astrophysical Journal* vol. 481, no. 1, pp. 500–514.
- Cheng, J. X., Ding, M. D., and Carlsson, M. (Mar. 2010). “Radiative Hydrodynamic Simulation of the Continuum Emission in Solar White-Light Flares”. In: *The Astrophysical Journal* vol. 711, no. 1, pp. 185–191.
- Christe, S. et al. (Mar. 2016). “FOXSI-2: Upgrades of the Focusing Optics X-ray Solar Imager for its Second Flight”. In: *Journal of Astronomical Instrumentation* vol. 5, no. 1, 1640005-625, pp. 1640005–625.
- Cirtain, J. W. et al. (Jan. 2013). “Energy release in the solar corona from spatially resolved magnetic braids”. In: *Nature* vol. 493, no. 7433, pp. 501–503.
- De Pontieu, B. et al. (July 2014). “The Interface Region Imaging Spectrograph (IRIS)”. In: *Solar Physics* vol. 289, no. 7, pp. 2733–2779. arXiv: [1401.2491](#) [[astro-ph.SR](#)].
- Dere, K. P. et al. (Oct. 1997). “CHIANTI - an atomic database for emission lines”. In: *Astronomy & Astrophysics Supplement Series* vol. 125, pp. 149–173.
- Dorfi, E. A. and Drury, L. O. (Mar. 1987). “Simple adaptive grids for 1-D initial value problems.” In: *Journal of Computational Physics* vol. 69, pp. 175–195.
- Emslie, A. G. (Aug. 1978). “The collisional interaction of a beam of charged particles with a hydrogen target of arbitrary ionization level.” In: *The Astrophysical Journal* vol. 224, pp. 241–246.
- Emslie, A. G., Dennis, B. R., et al. (Nov. 2012). “Global Energetics of Thirty-eight Large Solar Eruptive Events”. In: *The Astrophysical Journal* vol. 759, no. 1, 71, p. 71. arXiv: [1209.2654](#) [[astro-ph.SR](#)].
- Emslie, A. G., Kucharek, H., et al. (Oct. 2004). “Energy partition in two solar flare/CME events”. In: *Journal of Geophysical Research (Space Physics)* vol. 109, no. A10, A10104, A10104.
- Frogner, L. and Gudiksen, B. V. (Oct. 2022). “Implementing accelerated particle beams in a 3D simulation of the quiet Sun”. In: *arXiv e-prints*, arXiv:2210.01609, arXiv:2210.01609. arXiv: [2210.01609](#) [[astro-ph.SR](#)].
- Frogner, L., Gudiksen, B. V., and Bakke, H. (Nov. 2020). “Accelerated particle beams in a 3D simulation of the quiet Sun”. In: *Astronomy & Astrophysics* vol. 643, A27, A27. arXiv: [2005.14483](#) [[astro-ph.SR](#)].
- Glesener, L. et al. (Mar. 2020). “Accelerated Electrons Observed Down to <7 keV in a NuSTAR Solar Microflare”. In: *The Astrophysical Journal Letters* vol. 891, no. 2, L34, p. L34. arXiv: [2003.12864](#) [[astro-ph.SR](#)].
- Gudiksen, B. V. et al. (July 2011). “The stellar atmosphere simulation code Bifrost. Code description and validation”. In: *Astronomy & Astrophysics* vol. 531, A154, A154. arXiv: [1105.6306](#) [[astro-ph.SR](#)].
- Hannah, I. G., Hudson, H. S., Battaglia, M., et al. (Sept. 2011). “Microflares and the Statistics of X-ray Flares”. In: *Space Science Reviews* vol. 159, no. 1-4, pp. 263–300.
- Hannah, I. G., Hudson, H. S., Hurford, G. J., et al. (Nov. 2010). “Constraining the Hard X-ray Properties of the Quiet Sun with New RHESSI Observations”.

- In: *The Astrophysical Journal* vol. 724, no. 1, pp. 487–492. arXiv: 1009.2918 [astro-ph.SR].
- Hansteen, V. et al. (Oct. 2015). “Numerical Simulations of Coronal Heating through Footpoint Braiding”. In: *The Astrophysical Journal* vol. 811, no. 2, 106, p. 106. arXiv: 1508.07234 [astro-ph.SR].
- Harrison, F. A. et al. (June 2013). “The Nuclear Spectroscopic Telescope Array (NuSTAR) High-energy X-Ray Mission”. In: *The Astrophysical Journal* vol. 770, no. 2, 103, p. 103.
- Hudson, H. S. (June 1991). “Solar flares, microflares, nanoflares, and coronal heating”. In: *Solar Physics* vol. 133, no. 2, pp. 357–369.
- Kerr, G. S. et al. (Jan. 2019). “SI IV Resonance Line Emission during Solar Flares: Non-LTE, Nonequilibrium, Radiation Transfer Simulations”. In: *The Astrophysical Journal* vol. 871, no. 1, 23, p. 23. arXiv: 1811.11075 [astro-ph.SR].
- Klimchuk, J. A. (Mar. 2006). “On Solving the Coronal Heating Problem”. In: *Solar Physics* vol. 234, no. 1, pp. 41–77. arXiv: astro-ph/0511841 [astro-ph].
- (Apr. 2015). “Key aspects of coronal heating”. In: *Philosophical Transactions of the Royal Society of London Series A* vol. 373, no. 2042, pp. 20140256–20140256. arXiv: 1410.5660 [astro-ph.SR].
- Kobayashi, K. et al. (Nov. 2014). “The High-Resolution Coronal Imager (Hi-C)”. In: *Solar Physics* vol. 289, no. 11, pp. 4393–4412.
- Krucker, S., Christe, S., et al. (Oct. 2014). “First Images from the Focusing Optics X-Ray Solar Imager”. In: *The Astrophysical Journal Letters* vol. 793, no. 2, L32, p. L32.
- Krucker, S., Hudson, H. S., et al. (May 2010). “Measurements of the Coronal Acceleration Region of a Solar Flare”. In: *The Astrophysical Journal* vol. 714, no. 2, pp. 1108–1119.
- Leenaarts, J. et al. (Aug. 2013a). “The Formation of IRIS Diagnostics. I. A Quintessential Model Atom of Mg II and General Formation Properties of the Mg II h&k Lines”. In: *The Astrophysical Journal* vol. 772, no. 2, 89, p. 89. arXiv: 1306.0668 [astro-ph.SR].
- (Aug. 2013b). “The Formation of IRIS Diagnostics. II. The Formation of the Mg II h&k Lines in the Solar Atmosphere”. In: *The Astrophysical Journal* vol. 772, no. 2, 90, p. 90. arXiv: 1306.0671 [astro-ph.SR].
- Lemen, J. R. et al. (Jan. 2012). “The Atmospheric Imaging Assembly (AIA) on the Solar Dynamics Observatory (SDO)”. In: *Solar Physics* vol. 275, no. 1-2, pp. 17–40.
- Lin, R. P., Dennis, B. R., et al. (Nov. 2002). “The Reuven Ramaty High-Energy Solar Spectroscopic Imager (RHESSI)”. In: *Solar Physics* vol. 210, no. 1, pp. 3–32.
- Lin, R. P. and Hudson, H. S. (Apr. 1971). “10 100 keV electron acceleration and emission from solar flares”. In: *Solar Physics* vol. 17, no. 2, pp. 412–435.
- Marsh, A. J. et al. (Nov. 2017). “First NuSTAR Limits on Quiet Sun Hard X-Ray Transient Events”. In: *The Astrophysical Journal* vol. 849, no. 2, 131, p. 131. arXiv: 1711.05385 [astro-ph.SR].

- Martens, P. C. H. and Kuin, N. P. M. (Sept. 1989). “A Circuit Model for Filament Eruptions and Two-Ribbon Flares”. In: *Solar Physics* vol. 122, no. 2, pp. 263–302.
- Matsumoto, T. (Nov. 2016). “Competition between shock and turbulent heating in coronal loop system”. In: *Monthly Notices of the Royal Astronomical Society* vol. 463, no. 1, pp. 502–511. arXiv: [1606.06019](https://arxiv.org/abs/1606.06019) [astro-ph.SR].
- McIntosh, S. W. et al. (July 2011). “Alfvénic waves with sufficient energy to power the quiet solar corona and fast solar wind”. In: *Nature* vol. 475, no. 7357, pp. 477–480.
- Milkey, R. W. and Mihalas, D. (Sept. 1974). “Resonance line transfer with partial redistribution: II. The solar Mg II lines.” In: *The Astrophysical Journal* vol. 192, pp. 769–776.
- Musset, S. et al. (Sept. 2019). “Ghost-ray reduction and early results from the third FOXSI sounding rocket flight”. In: *UV, X-Ray, and Gamma-Ray Space Instrumentation for Astronomy XXI*. Ed. by Siegmund, O. H. Vol. 11118. Society of Photo-Optical Instrumentation Engineers (SPIE) Conference Series, 1111812, p. 1111812.
- Parker, E. N. (July 1988). “Nanoflares and the Solar X-Ray Corona”. In: *The Astrophysical Journal* vol. 330, p. 474.
- Pereira, T. M. D. and Uitenbroek, H. (Feb. 2015). “RH 1.5D: a massively parallel code for multi-level radiative transfer with partial frequency redistribution and Zeeman polarisation”. In: *Astronomy & Astrophysics* vol. 574, A3, A3. arXiv: [1411.1079](https://arxiv.org/abs/1411.1079) [astro-ph.SR].
- Pesnell, W. D., Thompson, B. J., and Chamberlin, P. C. (Jan. 2012). “The Solar Dynamics Observatory (SDO)”. In: *Solar Physics* vol. 275, no. 1-2, pp. 3–15.
- Polito, V. et al. (Apr. 2018). “Investigating the Response of Loop Plasma to Nanoflare Heating Using RADYN Simulations”. In: *The Astrophysical Journal* vol. 856, no. 2, 178, p. 178. arXiv: [1804.05970](https://arxiv.org/abs/1804.05970) [astro-ph.SR].
- Priest, E. (2014). *Magnetohydrodynamics of the Sun*.
- Quintero Noda, C. et al. (Oct. 2022). “The European Solar Telescope”. In: *Astronomy & Astrophysics* vol. 666, A21, A21. arXiv: [2207.10905](https://arxiv.org/abs/2207.10905) [astro-ph.SR].
- Reale, F. (July 2014). “Coronal Loops: Observations and Modeling of Confined Plasma”. In: *Living Reviews in Solar Physics* vol. 11, no. 1, 4, p. 4.
- Robinson, R. A. and Carlsson, M. (Sept. 2023). “Tracing the signatures of a quiet Sun nanoflare”. In: *The Astrophysical Journal* vol. 677, A36, A36.
- Shibata, K. et al. (Oct. 1995). “Hot-Plasma Ejections Associated with Compact-Loop Solar Flares”. In: *The Astrophysical Journal Letters* vol. 451, p. L83.
- Shine, R. A., Milkey, R. W., and Mihalas, D. (Aug. 1975). “Resonance Line Transfer with Partial Redistribution. V. The Solar CA II Lines”. In: *The Astrophysical Journal* vol. 199, pp. 724–733.
- Testa, P., De Pontieu, B., Allred, J., et al. (Oct. 2014). “Evidence of nonthermal particles in coronal loops heated impulsively by nanoflares”. In: *Science* vol. 346, no. 6207, 1255724, p. 1255724. arXiv: [1410.6130](https://arxiv.org/abs/1410.6130) [astro-ph.SR].

- Testa, P., De Pontieu, B., Martínez-Sykora, J., et al. (June 2013). “Observing Coronal Nanoflares in Active Region Moss”. In: *The Astrophysical Journal Letters* vol. 770, no. 1, L1, p. L1. arXiv: 1305.1687 [astro-ph.SR].
- Testa, P., Polito, V., and De Pontieu, B. (Feb. 2020). “IRIS Observations of Short-term Variability in Moss Associated with Transient Hot Coronal Loops”. In: *The Astrophysical Journal* vol. 889, no. 2, 124, p. 124. arXiv: 1910.08201 [astro-ph.SR].
- Testa, P., Saar, S. H., and Drake, J. J. (Apr. 2015). “Stellar activity and coronal heating: an overview of recent results”. In: *Philosophical Transactions of the Royal Society of London Series A* vol. 373, no. 2042, pp. 20140259–20140259. arXiv: 1502.07401 [astro-ph.SR].
- Uitenbroek, H. (Aug. 2001). “Multilevel Radiative Transfer with Partial Frequency Redistribution”. In: *The Astrophysical Journal* vol. 557, no. 1, pp. 389–398.
- Vardavas, I. M. and Cram, L. E. (Oct. 1974). “Partially coherent scattering models for the formation of the chromospheric Ca ii K line”. In: *Solar Physics* vol. 38, no. 2, pp. 367–376.
- Vernazza, J. E., Avrett, E. H., and Loeser, R. (Apr. 1981). “Structure of the solar chromosphere. III. Models of the EUV brightness components of the quiet sun.” In: *The Astrophysical Journal Supplement Series* vol. 45, pp. 635–725.
- Winebarger, A. R. et al. (July 2013). “Detecting Nanoflare Heating Events in Subarcsecond Inter-moss Loops Using Hi-C”. In: *The Astrophysical Journal* vol. 771, no. 1, 21, p. 21.
- Wright, P. J. et al. (Aug. 2017). “Microflare Heating of a Solar Active Region Observed with NuSTAR, Hinode/XRT, and SDO/AIA”. In: *The Astrophysical Journal* vol. 844, no. 2, 132, p. 132. arXiv: 1706.06108 [astro-ph.SR].

Papers

Paper I

Chromospheric emission from nanoflare heating in RADYN simulations

**Helle Bakke, Mats Carlsson, Luc Rouppe van der Voort, Boris
V. Gudiksen, Vanessa Polito, Paola Testa, Bart De Pontieu**

A&A 659, A186 (2022)

DOI:10.1051/0004-6361/202142842

Chromospheric emission from nanoflare heating in RADYN simulations

H. Bakke^{1,2}, M. Carlsson^{1,2}, L. Rouppe van der Voort^{1,2}, B. V. Gudiksen^{1,2}, V. Polito^{3,4},
P. Testa⁵, and B. De Pontieu^{4,1,2}

¹ Institute of Theoretical Astrophysics, University of Oslo, PO Box 1029, Blindern, 0315 Oslo, Norway
e-mail: helle.bakke@astro.uio.no

² Roseland Centre for Solar physics, University of Oslo, PO Box 1029, Blindern, 0315 Oslo, Norway

³ Bay Area Environmental Research Institute, NASA Research Park, Moffett Field, CA 94035, USA

⁴ Lockheed Martin Solar & Astrophysics Laboratory, 3251 Hanover St, Palo Alto, CA 94304, USA

⁵ Harvard-Smithsonian Center for Astrophysics, 60 Garden St, Cambridge, MA 02193, USA

Received 6 December 2021 / Accepted 26 January 2022

ABSTRACT

Context. Heating signatures from small-scale magnetic reconnection events in the solar atmosphere have proven to be difficult to detect through observations. Numerical models that reproduce flaring conditions are essential in understanding how nanoflares may act as a heating mechanism of the corona.

Aims. We study the effects of non-thermal electrons in synthetic spectra from 1D hydrodynamic RADYN simulations of nanoflare heated loops to investigate the diagnostic potential of chromospheric emission from small-scale events.

Methods. The Mg II h and k, Ca II H and K, Ca II 854.2 nm, and H α and H β chromospheric lines were synthesised from various RADYN models of coronal loops subject to electron beams of nanoflare energies. The contribution function to the line intensity was computed to better understand how the atmospheric response to the non-thermal electrons affects the formation of spectral lines and the detailed shape of their spectral profiles.

Results. The spectral line signatures arising from the electron beams highly depend on the density of the loop and the lower cutoff energy of the electrons. Low-energy (5 keV) electrons deposit their energy in the corona and transition region, producing strong plasma flows that cause both redshifts and blueshifts of the chromospheric spectra. Higher-energy (10 and 15 keV) electrons deposit their energy in the lower transition region and chromosphere, resulting in increased emission from local heating. Our results indicate that effects from small-scale events can be observed with ground-based telescopes, expanding the list of possible diagnostics for the presence and properties of nanoflares.

Key words. Sun: chromosphere – Sun: flares – methods: numerical – radiative transfer – line: profiles

1. Introduction

Nanoflares are small-scale events associated with magnetic reconnection in the solar atmosphere. The nanoflare heating mechanism is one of the prime candidates in understanding the high temperature of the corona (Parker 1988). Flare energy is believed to be transported by electrons from the thermal background, where the electrons are accelerated to non-thermal energies as the magnetic field lines reconnect. The accelerated electrons travel along the magnetic field through the transition region (TR) and chromosphere, where the energy is lost via Coulomb collisions with the ambient plasma (Brown 1971; Emslie 1978; Holman et al. 2011). This gives rise to observable signatures in spectral lines that are formed in the sites where energy is deposited. However, spectral line signatures are also affected by the response to the dissipated electron energy elsewhere in the atmosphere, such as strong plasma flows.

Signatures of non-thermal electrons are found in spectra from hard X-ray observations of active region flares. However, X-ray observations of small-scale events with energies in the range 10^{24} – 10^{25} erg remain rare because signatures from non-thermal electrons are typically below the detection threshold (although, see e.g., Wright et al. 2017; Glesener et al. 2020;

Cooper et al. 2021). Indications of energetic events are obtained in regions that are responsive to heating. In the corona, such indications are more difficult to observe because its high conductivity smears the heating signatures out. The TR, on the other hand, is highly responsive to heating because of rapid changes in density, temperature, and volume during heating events. Non-thermal electrons from coronal heating events give rise to changes in density and temperature through collisions with the dense TR and chromospheric plasma. Through advanced numerical simulations, Testa et al. (2014) have demonstrated that blueshifts in the Si IV 140.2 nm line observed with the Interface Region Imaging Spectrograph (IRIS; De Pontieu et al. 2014) in small heating events at the footpoints of transient hot loops are consistent with heating by non-thermal electrons, and they cannot be reproduced by models that assume heating only by thermal conduction. Polito et al. (2018) carried out an extensive numerical investigation to better understand and interpret TR observations by exploring a wide region of parameters. Testa et al. (2020) have further shown that observations of high variability (≤ 60 s) at the footpoints of active region (AR) high-temperature coronal loops (~ 8 – 10 MK) in combination with numerical simulations provide powerful diagnostics of coronal heating and energy transport.

Polito et al. (2018) analysed in detail the TR Si IV lines and upper chromospheric Mg II h and k lines from RADYN 1D simulations of nanoflare heated loops, and Testa et al. (2020) also investigated C II and Mg II triplet emission from the same set of simulations. In this work, we extend their analyses by probing the impact of electron beam heating on spectral lines that are formed deeper in the atmosphere and are readily accessible by ground-based telescopes: Ca II H and K, Ca II 854.2 nm, and H α and H β . We focus our efforts on the electron beam heating models with the shorter loop length (15 Mm) and initial loop-top temperatures of 1 and 3 MK, representing respectively an initially almost empty loop and a typical AR core loop. The selection of simulations is motivated by the study of nanoflare electron beams in 3D MHD Bifrost models (Bakke et al. 2018; Frogner et al. 2020), which only covers cooler and shorter loops. With RADYN we can more easily study the details of such conditions, while with Bifrost this is more difficult due to the complex configuration of the simulation. We reproduce the upper chromospheric Mg II h results of Polito et al. (2018) with the aim of making a direct comparison with the lower chromospheric observables. In the analysis we explore the impact of varying the low-energy cutoff value by investigating the atmospheric response, the Doppler shift of the chromospheric lines, and the formation of line intensity.

2. Method

2.1. The RADYN numerical code

The numerical simulations were performed using the RADYN numerical code (Carlsson & Stein 1992, 1995, 1997; Allred et al. 2015). RADYN solves the equation of charge and population conservation coupled to the non-linear equations of hydrodynamics in a 1D plane-parallel atmosphere on an adaptive grid (Dorfi & Drury 1987). The non-local thermodynamic equilibrium (non-LTE) radiation transport is solved for H, He, and Ca II, while continua from other atomic species are treated in local thermodynamic equilibrium (LTE) as background metal opacities using the Uppsala opacity package (Gustafsson 1973). Optically thin losses are calculated using the CHIANTI 7.1 atomic database (Dere et al. 1997).

The RADYN version described in Allred et al. (2015) allows to model the effect of non-thermal electrons in flaring loops. The particle distribution function is calculated by the Fokker-Planck equations, and the electron beam spectrum follows a power-law. With RADYN flare models it is possible to study the atmospheric response to energy deposited in the loop. RADYN models half of the loop only, between one footpoint and the loop apex. It is implicitly assumed that the full loop is symmetric around the apex. Further, the half-loop is modelled as a quarter circle, where the geometry is used to vary the value for the gravitational acceleration along the z -axis. The radiative transfer is computed by assuming a 1D atmosphere along the z -axis. The spectral diagnostics of interest are formed in the lowest part of the atmosphere where the loop geometry is near-vertical. This allows for comparisons with observations with a top-down line of sight.

We have investigated the heating models of coronal nanoflares carried out by Polito et al. (2018), but focused our efforts on the models with transport by non-thermal electrons. The atmospheric structure included a plage-like chromosphere following the work by Carlsson et al. (2015). The numerical investigation included several nanoflare models with different loop-top temperatures and parameters of the non-thermal electron power-law distribution.

2.2. Parameter survey

A total of six numerical simulations were analysed. The energy deposited in a single loop was set to $E = 6 \cdot 10^{24}$ erg in all models, following the work by Testa et al. (2014, 2020). The cross-sectional area of the loop was set to $A = 5 \cdot 10^{10}$ m², corresponding to a diameter of about 250 km. The half-loop lengths were set to 15 Mm with initial loop-top temperatures $T_{\text{LT}} = 1$ and 3 MK, giving two initial atmospheres that aimed to reproduce AR loops at different heating stages. With the assumption of an atmosphere in hydrostatic equilibrium, low-temperature loops have low density while hotter loops are also denser. The 1 MK loop represents an empty strand where heating has not yet occurred, and has an apex electron number density around $10^{8.7}$ cm⁻³. The 3 MK loop represents a previously heated strand with apex electron number density of approximately $10^{9.6}$ cm⁻³. In the following, we refer to the 1 MK and 3 MK loops as empty and pre-heated loops, respectively.

In RADYN flare models, the energy flux F , spectral index δ , and low-energy cutoff E_C that go into the power-law distribution are user-specified. The input value for the electron beam energy flux was calculated as

$$F = \frac{E}{At} = 1.2 \cdot 10^9 \text{ erg cm}^{-2} \text{ s}^{-1}, \quad (1)$$

where E and A are the total energy and cross-section of the loop given above. The loop was heated constantly for $t = 10$ s which is consistent with IRIS observations of TR moss showing that the lifetime of short-lived footpoint brightenings varies between 10–30 s (Testa et al. 2013, 2014, 2020).

A large spectral index ($\delta = 7$) was chosen for the energy distribution, supported by observational evidence of increasing spectral index with decreasing flare energy (Hannah et al. 2011), and compatible with values from rare hard X-ray observations of these small heating events (e.g., Glesener et al. 2020; Cooper et al. 2021). The low-energy cutoff values $E_C = 5, 10, \text{ and } 15$ keV were chosen to represent beams that are dominated by low-, intermediate-, and high-energy electrons. Figure 1 shows examples of power-law distributions for the different values of E_C , where the total energy of the beam is fixed. Each distribution starts at its respective cutoff energy (which is the energy that most of the electrons have because of the large spectral index), before exponentially declining as the energy increases. The $E_C = 5$ keV distribution shows that there are few electrons with $E > 9$ keV, and that most of the electrons have energies between 5 and 6 keV. As the cutoff energy increases, the number of electrons with $E = E_C$ decreases. However, there are generally more electrons with higher energies in these distributions.

2.3. Spectral synthesis with RH

The chromospheric lines were synthesised using the RH1.5D radiative transfer code (Uitenbroek 2001; Pereira & Uitenbroek 2015). RH1.5D solves the non-LTE radiative transport for spectral lines in partial redistribution (PRD). This is important in the synthesis of spectral lines where there is a correlation between the frequencies of the absorbed and re-emitted radiation such that the line source function varies with frequency. RADYN assumes complete redistribution, where the frequencies of the ingoing and outgoing photons are independent. While this is reasonable for the energetics in RADYN simulations, the assumption is best suited for modelling of photospheric lines. A more accurate treatment of photon scattering is required when modelling chromospheric lines, hence PRD is generally assumed

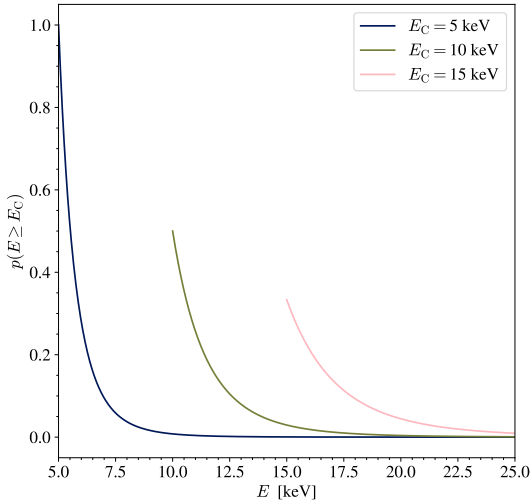


Fig. 1. Sketch of power-law distributions with different cutoff energies E_C , on a linear scaling. The figure serves as a visual aid to distinguish the difference between the electron distributions.

in the synthesis of Mg II h and k (Milkey & Mihalas 1974; Leenaarts et al. 2013a,b) and Ca II H and K (Vardavas & Cram 1974; Shine et al. 1975; Bjørgen et al. 2018).

The atmospheric evolution from the RADYN simulations was used as input to the RH code at every second. We added a microturbulence term of 7 km s^{-1} to produce a plage-like chromosphere following the work of Carlsson et al. (2015). This atmospheric structure is not proposed as a realistic model of plage, but aims to reproduce the observed average Mg II k line profile. However, we note that the atmosphere still fails to reproduce the single peaked profiles observed in plage.

In the synthesis of hydrogen and calcium, we used the 5 level-plus-continuum H I and Ca II atoms that are standard in RH1.5D, while for magnesium, we used the 10 level-plus-continuum Mg II atom from Leenaarts et al. (2013a). All lines were treated in PRD, even though Bjørgen et al. (2018) found that it is less important for Ca II 854.2 nm. The synthetic spectra were calculated for the first 40 s, allowing us to investigate the chromospheric emission during the heating and post-heating phases in detail.

Testa et al. (2020) investigated the Mg II 279.882 nm triplet in a variety of RADYN simulations, including the empty loop models presented here. The Mg II triplet lines (279.160 nm, 279.875 nm and 279.882 nm) are located in the wings of the h and k lines, and are expected to be in emission when large temperature increases are present in the lower chromosphere (Pereira et al. 2015). We included the Mg II 279.882 nm triplet in the formation height analysis, in order to compare it to the Ca II 854.2 nm line which is formed in the lower chromosphere.

2.4. Contribution function to the line intensity

The final part of the spectral diagnostics consisted of analysing the contribution function to the emergent intensity. Following Carlsson & Stein (1997), the contribution function was

calculated as

$$C_I(z) \equiv \frac{dJ_\nu(z)}{dz} = S_\nu \tau_\nu e^{-\tau_\nu} \frac{\chi_\nu}{\tau_\nu}. \quad (2)$$

The first term on the right-hand side gives the total source function S_ν , which is dependent on frequency because we assume PRD. The optical depth factor $\tau_\nu e^{-\tau_\nu}$ represents the Eddington-Barbier part of the contribution function, and peaks at $\tau_\nu = 1$. The χ_ν/τ_ν term is the ratio of the opacity over optical depth which is sensitive to velocity gradients in the atmosphere, and is responsible for the line asymmetries. The factor is dominant when the opacity is large at small optical depths, which typically occurs when the velocity gradients are strong.

The opacity χ_ν and source function S_ν were calculated by the RH1.5D code for selected wavelengths, and the optical depth τ_ν was calculated by integrating the opacity over the entire loop length. The contribution function to the line intensity was calculated in the range $z = 0\text{--}2 \text{ Mm}$, which is the part of the loop that has near-vertical geometry.

3. Results

3.1. Atmospheric response to non-thermal electrons

Figures 2 and 3 show the evolution of temperature T , vertical velocity v_z , electron number density n_e , and beam heating rate H for the loops with $T_{\text{LT}} = 1$ and 3 MK. The quantities are plotted in the range of interest in terms of formation heights for the relevant spectra. For the temperature, velocity, and density, we focus on the first 20 s of the simulations in order to investigate the heating and early relaxation phase in more detail. The beam heating rate is shown for the first 10 s, corresponding to the loop heating time. These figures essentially reproduce Figs. 2 and 3 of Polito et al. (2018), but show the evolution in the lower 3 Mm of the loops in more detail. We refer to Polito et al. (2018) for more details on the evolution of the entire 15 Mm loop-length.

3.1.1. Empty loop

The difference between heating models is largest in the loop with initial low electron number density and 1 MK loop-top temperature (see Fig. 2). During the 10 s heating phase, electrons with $E_C = 5 \text{ keV}$ deposit most of their energy in the corona and TR, leading to an increase in temperature and density of the ambient plasma of about one order of magnitude. This causes the TR to shift to lower depths, as can be seen in panel a. The large (negative) velocities in panel d result from an increase in pressure due to the rise in temperature. The upward motion of hot plasma (“chromospheric evaporation”) increases with height, and as a consequence, the loops are filled with hot plasma and the electrons start depositing energy at increasing heights (see panel j). The positive velocities are indicative of a significant downflow of plasma towards the chromosphere, caused by the condensation of hot plasma filling the flaring loop.

The heating models with $E_C = 10$ and 15 keV (middle and right columns) have more energetic electrons in their distributions. Higher-energy electrons can travel through the corona depositing only a small fraction of their energy, allowing them to penetrate deeper into the atmosphere. Panels h and i show that the deposited energy is at a maximum between $z \approx 1.5$ and 2.1 Mm within the first few seconds. The radiative losses from ionised hydrogen and helium are not able to balance the large amount of energy deposited, resulting in a temperature increase in this region (as can be seen in panels b and c). The

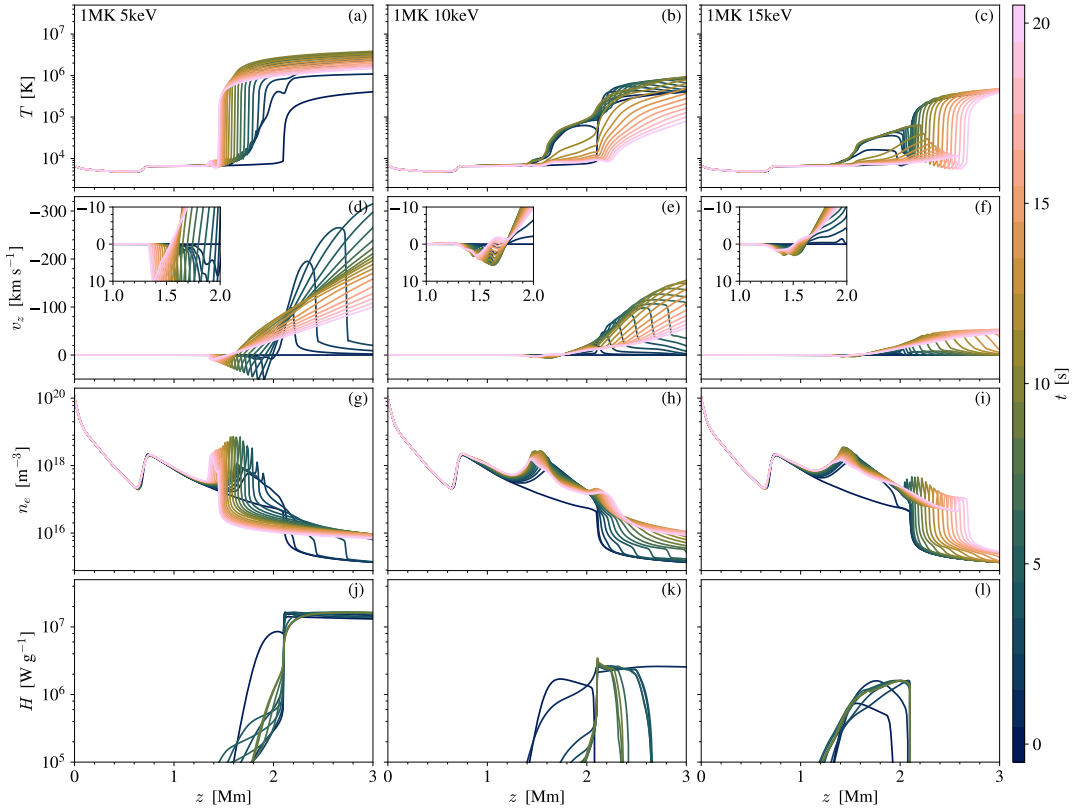


Fig. 2. Atmospheric response to the RADYN simulation for the 15 Mm half-loop with initial apex temperature of 1 MK. Each column corresponds to the heating model with $E_C = 5, 10,$ and 15 keV, and each row represents the temperature, velocity, electron number density, and beam heating rate. Negative (positive) velocities correspond to upflows (downflows). The quantities are plotted in the range $z \in [0, 3]$ Mm at 1 s intervals. Temperature, velocity, and electron number density are displayed for the first 20 s of the simulations, while the beam heating rate is given for the duration of the injected electron beam (10 s). The insets in panels *d–f* show the velocity in the region $z = 1–2$ Mm saturated to ± 10 km s $^{-1}$.

upflowing velocities in panels e and f are lower compared to the 5 keV model. This is due to the difference in sites where electron energy is deposited. While the 5 keV electrons deposit most of their energy in the corona and TR, the 10 and 15 keV electrons mostly deposit their energy in the chromosphere where the plasma is denser. Dense plasma is harder to accelerate, and the combination of this and the fact that energy radiates away more efficiently contributes to weaker upflowing velocities. Consequently, the upflows cause the TR to move towards greater heights.

The upward motion of hot plasma in the 10 and 15 keV heating models causes the density of the loops to increase over time, and similarly to the 5 keV model, the electrons start to deposit energy at increasing heights (see panels k and l). However, we note that in the 15 keV model the increase in height where energy is deposited does not change much over the 10 s heating duration compared to the other models. The 5 keV electrons are more effective at heating the corona, and the large upflowing velocity demonstrates that this heating model is more efficient at filling the flaring loop with high-temperature plasma.

3.1.2. Pre-heated loop

Figure 3 shows the atmospheric response to the heating models for the loops with initial apex temperature of 3 MK. As mentioned earlier, the hotter and denser loops represent strands that have been previously heated. Therefore, the initial atmospheres have transition regions that are located at lower depths compared to the 1 MK loop models. Panels a–c show a temperature increase in the corona for all E_C values. Due to the higher initial density of the loops, the injected electrons deposit more of their energy in the corona. In the 5 keV heating model, the energy deposited directly into the corona (as indicated by the increasing heating rate in the corona for all E_C values. Due to the higher initial density of the loops, the injected electrons deposit more of their energy in the corona. In the 5 keV heating model, the energy deposited directly into the corona (as indicated by the increasing heating rate with height in panel j, but also shown in Polito et al. 2018) causes the temperature and pressure to increase, leading to both upflows and downflows of plasma. However, not all electrons deposit their energy in the corona. Some of the electrons are able to reach the TR, where they deposit their energy at $z \approx 1.5$ Mm. The local heating of the TR in combination with the conduction front from the corona results in a pressure gradient that produces both upward motion of plasma towards the corona as well as downflowing plasma into the TR.

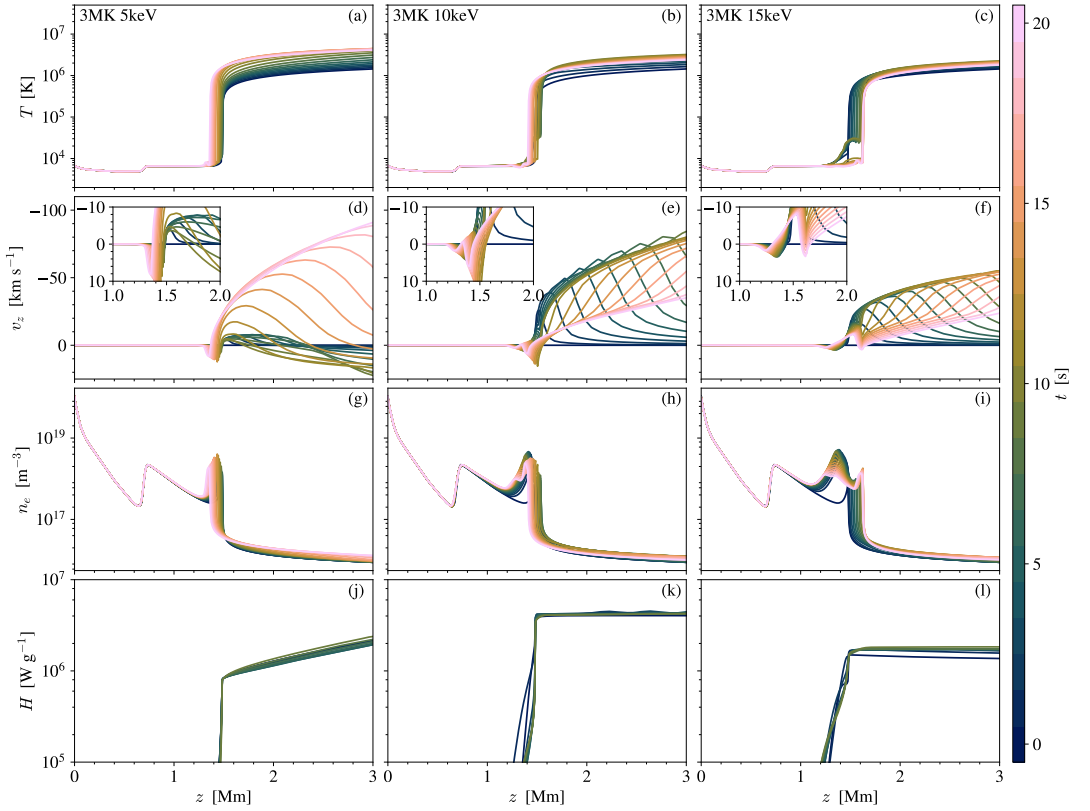


Fig. 3. Atmospheric response to the RADYN simulation for the 15Mm half-loop with initial apex temperature of 3MK. See Fig. 2 for an explanation of the different panels.

The intermediate- and high-energy electrons initially deposit their energy in the TR, resulting in upflows of hot plasma into the corona. As the loops are filled with high-temperature plasma, the electrons start to deposit energy at greater heights, as can be seen in panels k and l. Panels e and f show that as the height where energy is deposited increases, the evaporation front travels upwards along the loop. The moving TR region in panel c shows resemblance to the 10 and 15 keV runs in Fig. 2, where the properties of dense plasma in combination with direct heating results in an increased temperature. However, the atmospheric response is much slower for the 3MK loop because the plasma is harder to accelerate, hence the TR does not move much during the first 20 s.

3.2. Chromospheric emission

Figures 4 and 5 represent the time evolution of the synthetic Mg II h, Ca II K, and Ca II 854.2 nm spectra, along with their light curves, from the different heating models. The light curves are obtained by integrating the emission over the spectra in the wavelength range for each timestep. We note that the Mg II h results are similar to Mg II k, and that the Ca II K results are similar to Ca II H. Therefore, we only present our findings from the Mg II h and Ca II K lines. Polito et al. (2018) analysed the

Mg II h line in detail, and we reproduce the Mg II h results in order to make a direct comparison with the Ca II lines and study the effect from energy deposited by non-thermal electrons.

Figure 4 shows the chromospheric emission for the 1MK loop, where each column represents the different cutoff energies E_C . The three spectral lines in the $E_C = 5$ keV model are behaving similarly, but with some variation. The Mg II h and Ca II K profiles have redshifted components that are caused by the downflow of cool plasma into the chromosphere, as seen in Fig. 2d. The Mg II h line also has a blueshifted component, and is characterised by multiple peaks that are Doppler shifted up to approximately ± 50 km s⁻¹ during the heating phase. The Ca II K line shows multiple peaks in the redshifted component that are Doppler shifted to around $+40$ km s⁻¹. The Ca II 854.2 nm line shows weak emission of the red wing at the end of the heating phase. The blue peak gets broader and has a higher intensity level during the post-heating phase, as a response to the upflow of plasma into the corona and TR.

During the first 10 s of the simulations, while the electrons are still injected, the profiles in the $E_C = 10$ and 15 keV models are mostly double peaked. The spectra experience an increase in line core intensity during the heating phase. This is because the high-energy electrons are able to penetrate deeper into the atmosphere before depositing their energy, as can be seen from

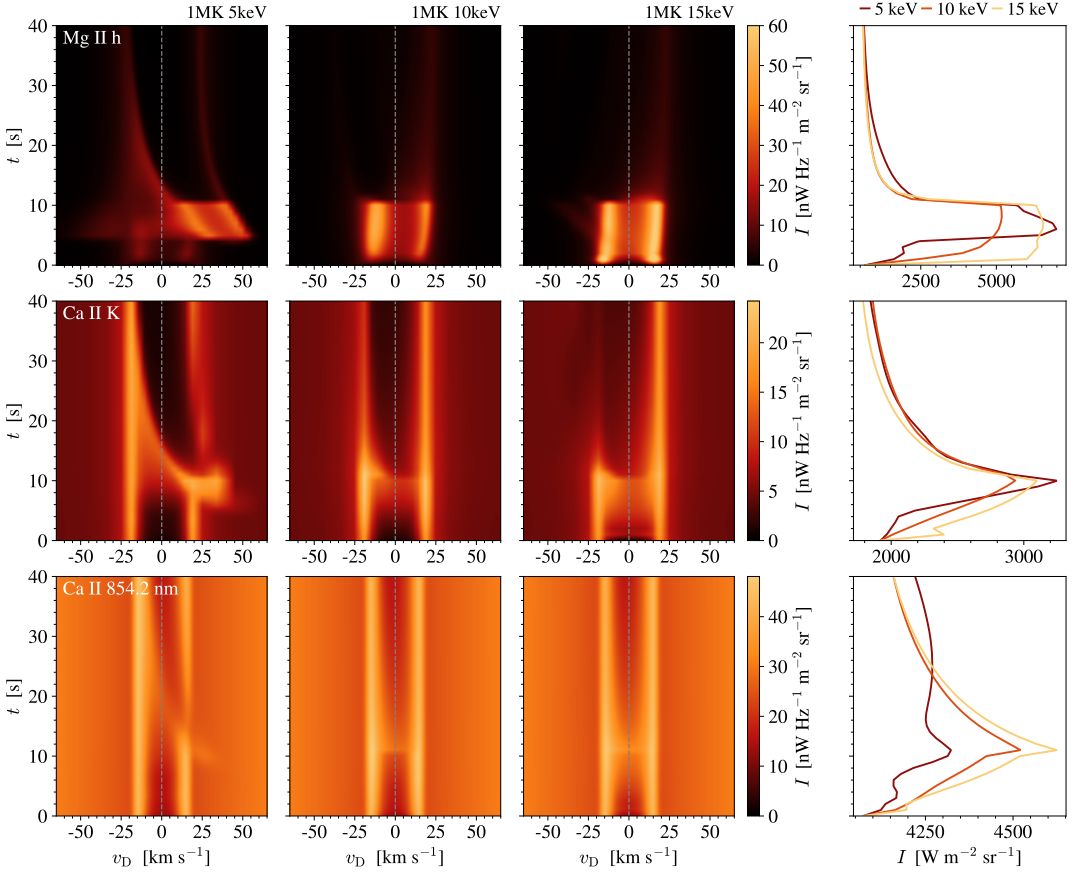


Fig. 4. Spectral evolution of Mg II h, Ca II K, and Ca II 854.2 nm spectra for the heating models with $T_{LT} = 1$ MK and $E_C = 5, 10,$ and 15 keV. The x -axes in the first three panels of each row are in units of Doppler offset, where negative (positive) velocities indicate blueshifts (redshifts). The panels of the right column show light curves from each heating model, where the x -axes are in units of integrated intensity. The first 40 s of the simulations are shown, including the 10 s electron injection phase. The Mg II h spectra are clipped at $60 \text{ nW Hz}^{-1} \text{ m}^{-2} \text{ sr}^{-1}$ to emphasise the less bright features. Line profiles for $t = 0, 7,$ and 15 s are shown in Fig. 6.

panels h and i in Fig. 2. During 5–10 s, the Mg II h line in the 15 keV model shows faint emission of the blue wing, which is Doppler shifted to approximately -30 km s^{-1} . After the heating phase, Mg II h and Ca II K are dominated by a red peak, and the profiles become almost single peaked. This is apparent from the solid pink lines in Fig. 6.

The light curves from the Mg II h spectra show a sudden increase in intensity as a response to the electron beams. The profile from the 5 keV model is generally less intense, but the integrated emission increases as a result of the broadening of the line. The light curves from the Ca II spectra have a slower increase and peak around 10 s. While most of the light curves decrease after the heating is turned off, the Ca II 854.2 nm integrated emission starts to increase around 15 s. This is due to the broadening and increased emission of the blue peak.

Figure 5 shows the spectra for the denser 3 MK loop. The 5 keV simulation shows qualitatively similar effects on the Mg II h and Ca II K lines, while the effect on the Ca II 854.2 nm

line is less significant. The Mg II h and Ca II K lines both show broadening of the blue peak at around 10 s. During the post-heating phase, the entire Mg II h line is shifted to the red before slowly reverting back. The blue component of Ca II K is characterised by double peaks, and the general behaviour of the intensity after the heating is turned off is similar to that of Ca II K in the 10 and 15 keV empty loop model. Due to the density of the loop, the electron energy is dissipated directly in the corona and TR. The chromosphere is not heated significantly, and the effects seen in Mg II h and Ca II K are due to local plasma flows.

In the 10 and 15 keV simulations, there is an increase in intensity as a function of E_C that is particularly apparent in Mg II. The peak intensity of Mg II h in the 10 keV model is comparable to that of an empty loop. However, the energy deposited from the 15 keV electrons affect the chromospheric line greatly, where the intensity of the red peak is much stronger compared to the empty loop (see Fig. 6). The Ca II 854.2 nm profiles in the $E_C \geq 10$ keV simulations are comparable to the results of the empty loop,

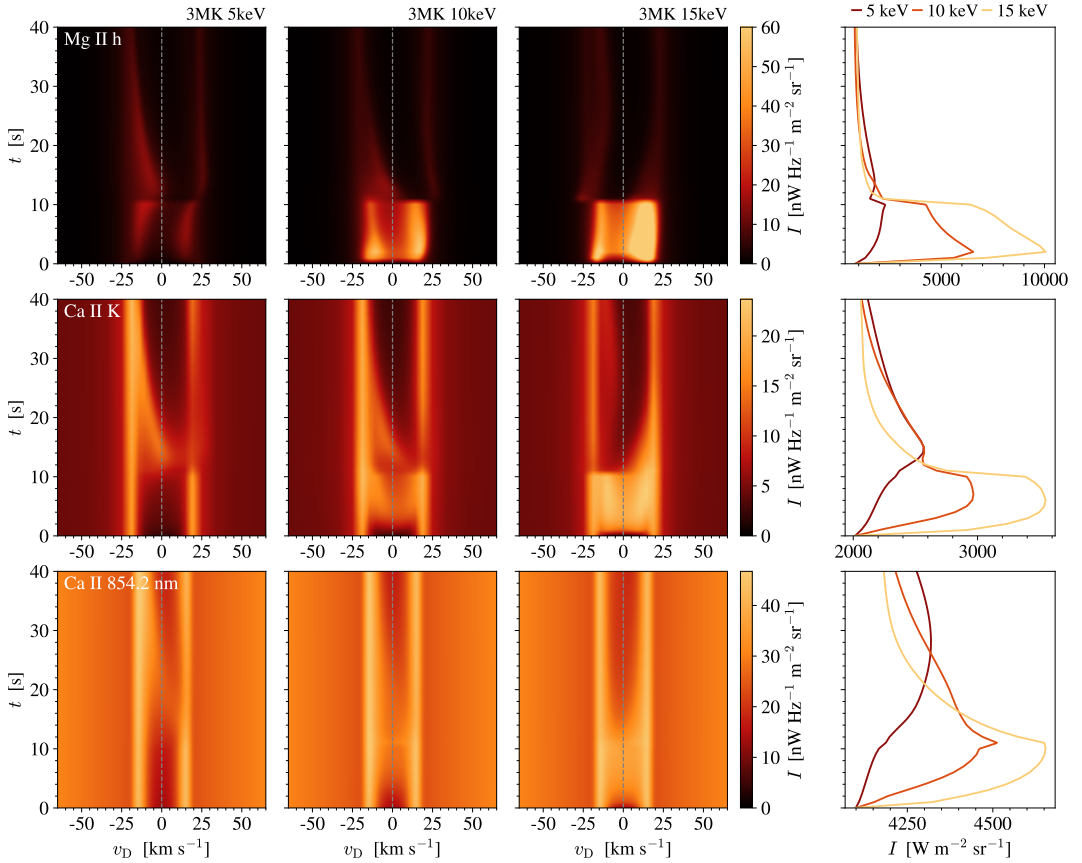


Fig. 5. Synthetic spectra for the $T_{\text{IR}} = 3$ MK heating models. See the caption of Fig. 4 for more details.

both in line features and evolution of the light curves. The Ca II K profiles are greatly affected by the intermediate- and high-energy electrons, and are characterised by multiple peaks and strong emission of the line core. The latter is reflected in the light curves, which are similar to the Mg II integrated emission from the 10 and 15 keV models in that they have a steep decline.

Figure 6 shows the Mg II and Ca II line profiles to better visualise the shapes and features that arise during the simulations. Particularly, the faint emission of the blue wing of Mg II h in the 15 keV empty loop model is easier to observe (see the solid green line in the upper right panel). In the 5 keV empty loop model and the 5 and 10 keV dense loop models, the Ca II K core is shifted to the red after the heating is turned off, and the blue component is double peaked. The Ca II 854.2 nm profiles show that the response to the non-thermal electrons is mostly changing the absorption feature, which gets brighter as time progresses. In the 5 keV models, the red emission peak of Ca II 854.2 nm is weaker at later timesteps.

Figure 7 represents the synthetic $H\alpha$ and $H\beta$ lines from all the simulations, and are given for the same timesteps as in Fig. 6. The initial profiles are almost identical across the sim-

ulation span, where both $H\alpha$ and $H\beta$ are in absorption. In the 1 MK low-energy model, both spectra are in emission during the heating phase. The $H\alpha$ line is characterised by a redshifted component with multiple peaks, while the redshifted $H\beta$ peak is severely broadened. In the post-heating phase, both lines are back in absorption, where their cores are Doppler shifted to approximately $+15 \text{ km s}^{-1}$. In the 3 MK loop, both lines are in absorption during the heating and post-heating phases, showing no significant effects as a consequence to the nanoflare event.

The intermediate- and high-energy models (both 1 and 3 MK loops) show similar effects in the $H\alpha$ and $H\beta$ lines. During the heating phase, the spectra are double peaked. In the 10 keV models, the blue peak is dominating the spectra in the empty loop, while the red peak dominates the spectra in the dense loop. In the 15 keV dense loop model, the red peak of both lines is more pronounced. The latter is also true for the $H\alpha$ line in the 1 MK loop, while $H\beta$ is almost symmetric around the line core. All heating models show that the line cores are in absorption during the post-heating phase, but some of the line cores are either redshifted or blueshifted as a response to the non-thermal electrons.

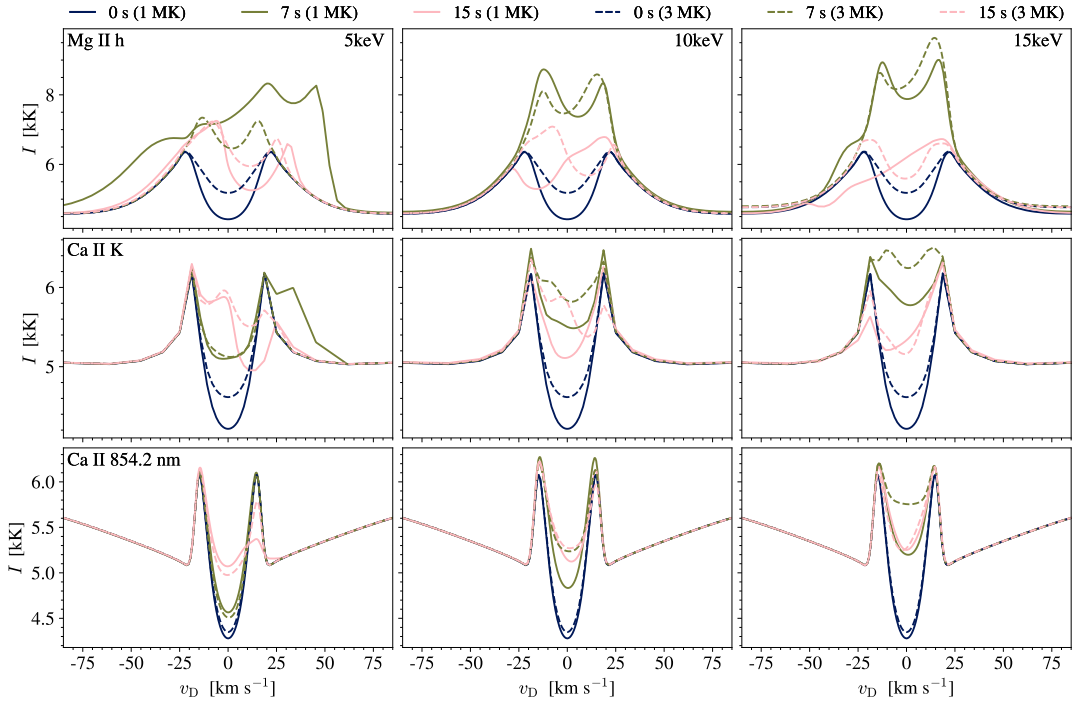


Fig. 6. Synthetic Mg II h, Ca II K, and Ca II 854.2 nm line profiles. The solid and dotted lines represent the 1 and 3 MK loops, respectively. Line profiles during the pre-heating ($t = 0$ s), heating ($t = 7$ s), and post-heating ($t = 15$ s) phases are shown.

3.3. Formation of line intensity

Figures 8 and 9 show four 2×2 diagrams of the intensity formation of Mg II h and Ca II K from two of the heating models presented in this work. Because of the extensive parameter survey, we selected two distinctively different models. We present the Mg II h and Ca II K spectra subject to low-energy (5 keV) electrons in the 1 MK loop and high-energy (15 keV) electrons in the 3 MK loop. The specifics of the simulations are given in the top left corner of each diagram. The panels in each subfigure represent the terms in Eq. (2), and are strongly inspired by the four-panel diagrams in Carlsson & Stein (1997).

Figure 8a shows the Mg II h line during the heating phase in the 5 keV empty loop model. The downward velocity gradient is reflected in the χ_v/τ_v term, exhibiting a strong variation in wavelength. As a result, the $\tau_v = 1$ height of the red peak is shifted to larger Doppler offsets. The source function is equal to the Planck function from the photosphere up to around 1.2 Mm where it decouples. Since the Planck function is given in units of brightness temperature, it also represents the temperature itself. The strong rise in temperature at 1.7 Mm gives rise to a significant increase in the source function. The peak in S_v is further responsible for the multiple peaks observed in the redshifted component of Mg II h. Investigation of the $\tau_v = 1$ height reveals that what appeared to be a double peaked blue component is emission of the blue wing. This is further supported by the increase in S_v around the blue wing. The contribution function is strongly dominated by the downward velocity gradient because of its dependence on χ_v/τ_v . Signatures of the upflows caus-

ing emission in the blue wing are therefore difficult to enhance visually. We have solved this by applying gamma correction to χ_v/τ_v and C_{I_v} , simply allowing us to highlight the darker regions.

The intensity formation of Mg II h during the post-heating phase is given in Fig. 8b. The velocity gradient from the down-flowing plasma is weaker compared to the heating phase, and has less impact on the χ_v/τ_v term. The source function is coupled to the Planck function until approximately $z = 1.4$ Mm. The sudden increase in temperature at 1.5 Mm causes the source function to peak, giving rise to two emission peaks in the intensity profile. The increase in temperature and source function gives rise to an additional peak at approximately 0 km s^{-1} , causing the minimum of the central absorption to shift to the red.

Figure 8c shows the intensity formation of Ca II K during the heating phase. The Ca II K line is symmetric between $\pm 25 \text{ km s}^{-1}$, as the $\tau_v = 1$ curve is not affected by the strong velocity gradient in this range. Here, the shape of the profile is mostly defined by the source function, which is coupled to the Planck function up to 0.9 Mm. At around $+35 \text{ km s}^{-1}$, the $\tau_v = 1$ height peaks as a response to the sudden increase in S_v , which is caused by the increase in temperature due to the strong down-flowing velocity. This gives rise to a separate redshifted component at $+35 \text{ km s}^{-1}$ in the Ca II K line. We note that PRD affects Ca II K less than Mg II h which becomes apparent in the source function panel in the top right: there is little variation in S_v along the x -axis for most of the atmosphere and S_v appears like a horizontal grey band.

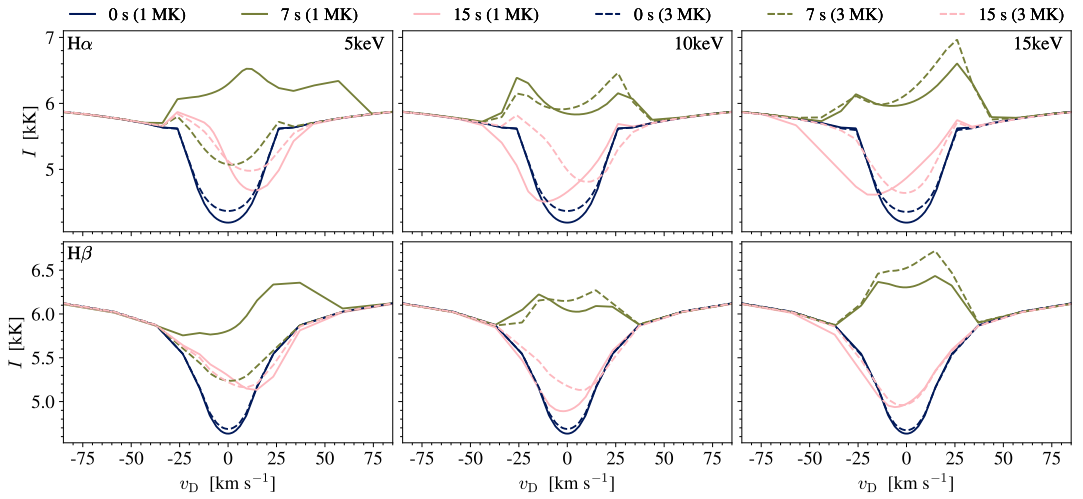


Fig. 7. Synthetic H α and H β spectra. See the caption of Fig. 6 for more details on the different panels.

Panel d in Fig. 8 gives the formation of Ca II K during the post-heating phase. Similar to Mg II h (see panel b), the less strong downflowing velocity is reflected in the χ_v/τ_v term, showing the largest increase around 0 km s^{-1} . The sudden increase in temperature at 1.5 Mm causes the source function to peak, giving rise to the peak near the centre of the line at approximately $+7 \text{ km s}^{-1}$. The intensity of the peak at -20 km s^{-1} is stronger than the peak at $+35 \text{ km s}^{-1}$ as a consequence of the formation of the peak near the line centre. We also note that the contribution function peaks at different Doppler offsets for Mg II h (0 km s^{-1}) and Ca II K ($+7 \text{ km s}^{-1}$), even though the lines form at the same height. This shows that the velocity is not the only contributing factor to the formation of spectral features, and this underlines the risk of simply interpreting the Doppler offset of spectral features as a direct measure of plasma flows in the atmosphere.

Figure 9a shows the formation of Mg II h during the heating phase in the 15 keV dense loop model. The source function is coupled to the Planck function up until 1.2 Mm, but continues to follow it closely up to around 1.4 Mm. The peak in S_ν gives a larger contribution to C_{I_ν} around the red component. As a consequence, the red peak experiences a larger intensity increase and the minimum of the central absorption is shifted to the blue.

The intensity formation of Mg II h during the post-heating phase is shown in Fig. 9b. The asymmetric $\tau_v = 1$ curve is caused by the variation in velocity between $z = 1.3\text{--}1.6 \text{ Mm}$. The source function is coupled to the Planck function up to 1.3 Mm. From this height, the source function follows a flat slope before it suddenly decreases at 1.6 Mm. The contribution function shows that the peaks of Mg II h form at different heights. The line profile is slightly shifted to the blue, with the minimum of the central absorption at approximately -5 km s^{-1} . The blueshift is caused by the general upflow pushing the TR towards greater heights (see Fig. 3c).

Figure 9c shows the intensity formation of Ca II K during the heating phase. The double peaks in the blue component are caused by the velocity gradient of the upflowing plasma. The source function peaks as a result of the temperature increase, but the upward motion of plasma dilutes the signal such that S_ν is

weaker around the $\tau_v = 1$ height of the line core. Still, the contribution to the line core is large enough to increase the intensity, making the emission peaks less pronounced.

Figure 9d shows the Ca II K line during the post-heating phase. The varying velocity of the fluid causes the asymmetric shape of the optical depth unity curve, where the $\tau_v = 1$ height increases up to 1.6 Mm at negative Doppler offsets. Similar to the Mg II h line, Ca II K is blueshifted to around -5 km s^{-1} . The source function and Planck function are coupled to approximately 0.9 Mm, but does not differ significantly until around 1.4 Mm. As the Planck function (and temperature) increases, the source function decreases. As a result, the source function makes a stronger contribution to C_{I_ν} at lower heights. This is reflected in the intensity profile, where the red peak is more intense than the blue peak.

Figure 10 shows the formation heights of the Mg II h, Mg II 279.88 nm triplet, Ca II K, Ca II 854.2 nm, H α , and H β line cores. We include the Mg II triplet to investigate how the formation height of another deep chromospheric line compares to Ca II 854.2 nm. Since the lines are formed under optically thick conditions, we define the formation height to be the maximum height of the $\tau_v = 1$ surface. During the heating phase in the 1 MK heating models (top panels), the Mg II h and Ca II cores are formed at lower heights compared to their initial $\tau_v = 1$ height, while the Mg II triplet, H α , and H β cores are formed higher in the chromosphere compared to their initial $\tau_v = 1$ height. In the 5 keV model, there is a sudden increase in the height of formation for all line cores. This sudden increase is progressively later for spectral lines with lower formation heights, which is caused by local effects from the receding TR (see Fig. 2a). As a response to the moving TR, the line cores form over a narrow region in the cooling phase due to the compression of the chromosphere. The formation heights of the line cores in the 10 and 15 keV models increase at 10 s as a result of the sudden decrease in temperature when the heating is turned off. As the temperature continues to decrease, the $\tau_v = 1$ heights approach their pre-heating values.

The bottom panels of Fig. 10 represent the 3 MK dense loop models. Since the loop is pre-heated, the TR is located

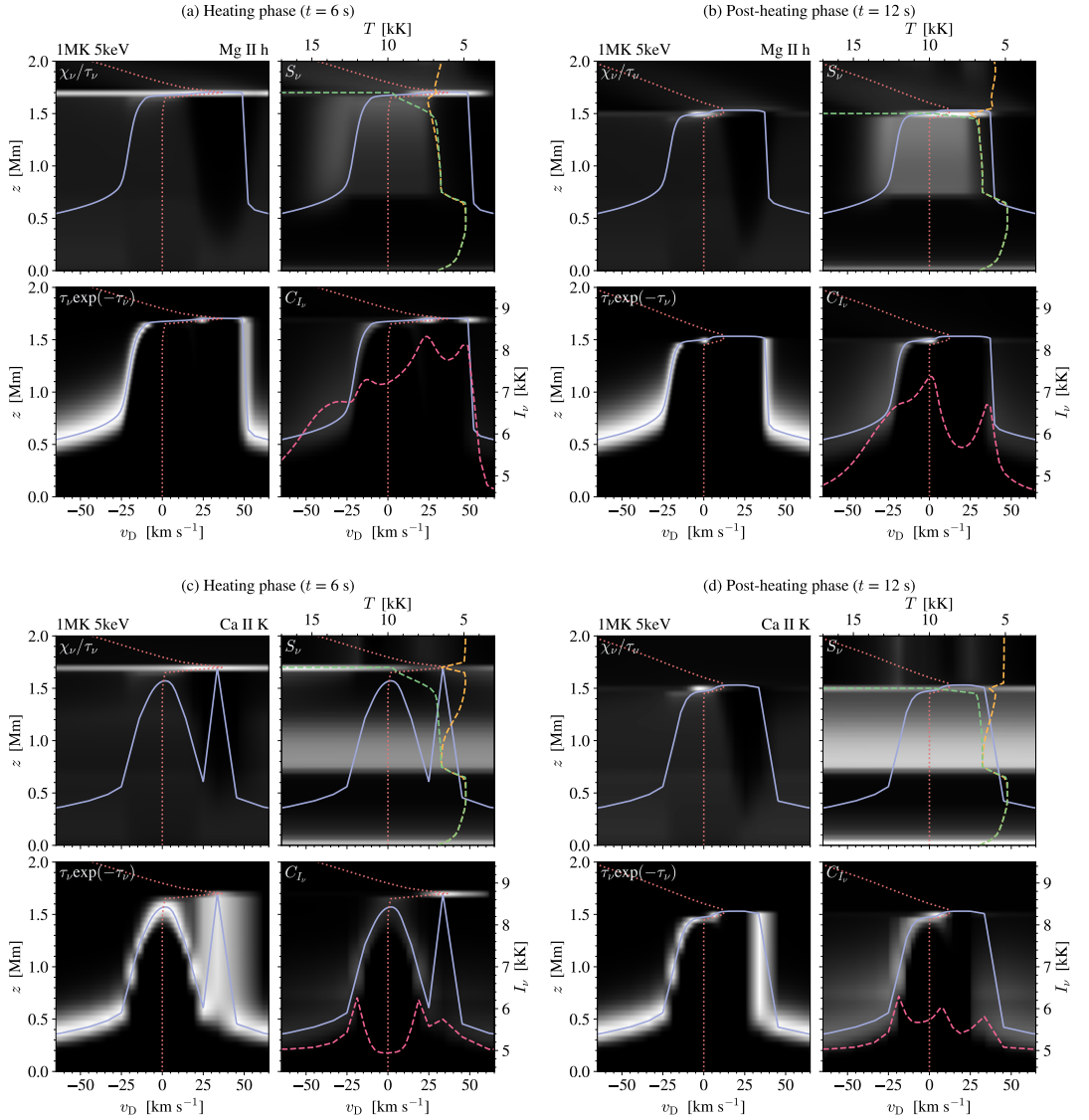


Fig. 8. Intensity formation of the Mg II h (*top*) and Ca II K (*bottom*) spectral lines from the 5 keV empty loop model. The subfigures show the heating phase (*(a)* and *(c)*) and early post-heating phase (*(b)* and *(d)*) for the two lines. The quantities given at the top left corner are shown in greyscale as functions of frequency from line centre (in units of Doppler offset) and height z . The $\tau_\nu = 1$ height (purple) and vertical velocity (red dotted) are displayed in all panels. Negative (positive) velocities correspond to upflows (downflows). In addition, the *top right panels* show the total source function at $v_D = 0$ (yellow dashed) and Planck function (green dashed) in units of brightness temperature, with high values to the left. The *bottom right panels* also contain the intensity profile (pink) as brightness temperature. Gamma correction is added to the χ_ν/τ_ν and C_ν terms to amplify the weaker signals.

at lower heights compared to the empty loop. The line cores therefore form at lower heights as well. The 5 keV electrons do not affect Mg II h, Ca II K, Ca II 854.2 nm, and H α significantly, hence these line cores form at similar heights during the heating phase. The chromosphere is affected by the intermediate- and high-energy electrons, but the response is slow since the loop is

already heated. As a result, the formation heights of the Mg II h and Ca II K cores do not drop as significantly within the first few seconds as in the empty loop. In the 10 keV model, the formation heights decrease as the TR recedes to lower depths. In the 15 keV model, the increase in $z(\tau_\nu = 1)$ after the heating is turned off is a result of the TR moving to greater heights.

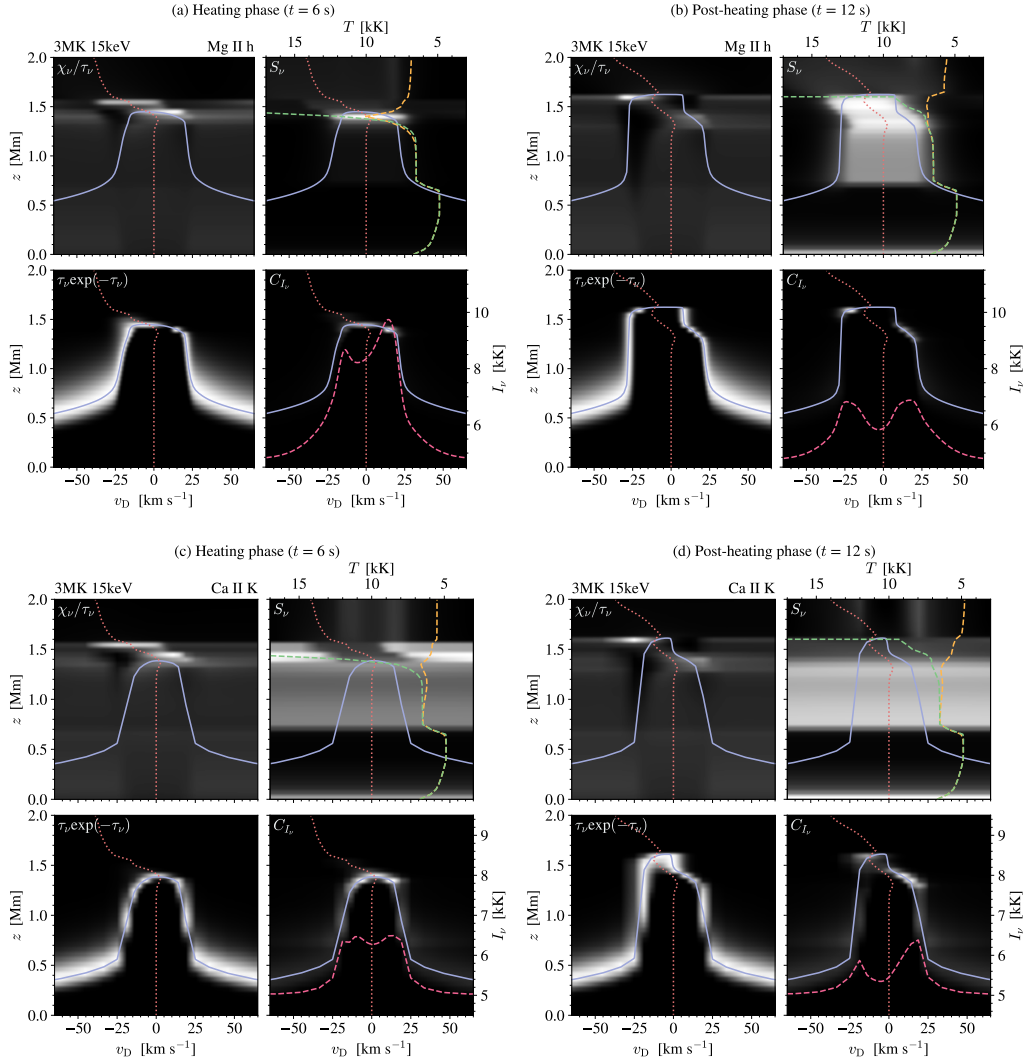


Fig. 9. Intensity formation of the Mg II h (*top*) and Ca II K (*bottom*) spectral lines from the 15 keV dense loop model. We note the different scaling of the brightness temperature in the top and bottom panels. See the caption of Fig. 8 for more details.

The increase in formation height during the heating phase for the Mg II triplet and H β cores shows that these lines are sensitive to heating. This result was also found by Testa et al. (2020) for the Mg II triplet. The 5 keV dense loop model even demonstrates that minor atmospheric responses from energy deposited by the non-thermal electrons affect their $\tau_\nu = 1$ heights. In addition, the panels show that Ca II 854.2 nm is the deepest diagnostic when electrons are being injected into the loop.

4. Discussion

By extending the spectral line diagnostics of Polito et al. (2018) and Testa et al. (2020), we find that also dominant chromo-

spheric lines in the visible are affected by coronal nanoflare events. The signatures that arise from the non-thermal electron beams highly depend on the initial physical conditions of the loop in combination with the low-energy cutoff E_C of the power-law distribution of accelerated electrons. Most importantly, the distance the electrons travel before their energy is deposited is largely dependent on the density of the loop and the energy of the electrons. In low-density loops, there are fewer collisions with the ambient plasma, and vice versa. The spectral line signatures are not only affected by the energy deposited directly in the regions where they form, but also by the response to the effects from electron beam energy dissipated elsewhere in the atmosphere, for example plasma flows.

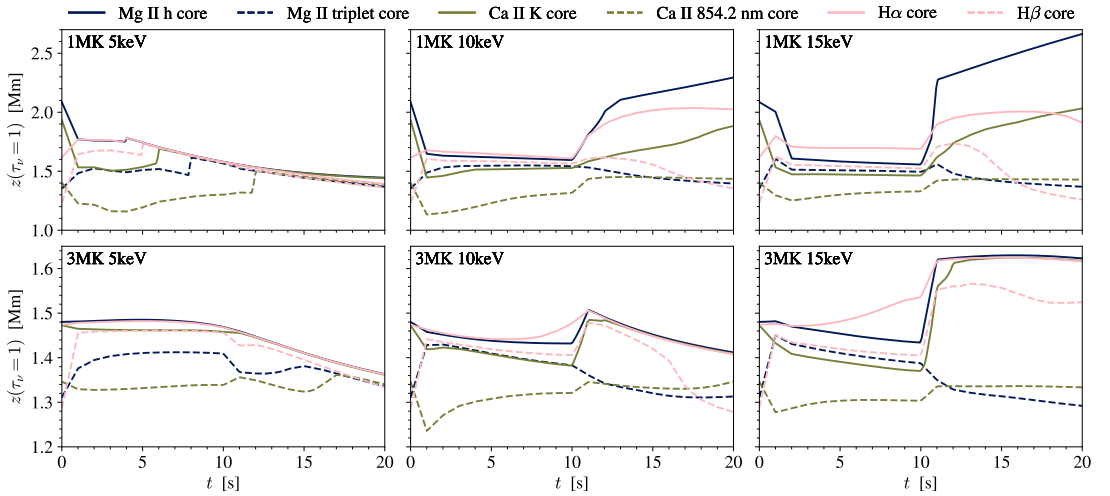


Fig. 10. Maximum formation height of the Mg II h, Mg II 279.882 nm triplet, Ca II K, Ca II 854.2 nm, H α , and H β line cores. The first 20 s of the simulations are shown, where time is given on the x-axis. Each panel represents the different heating models, as stated in the upper left corners.

The most significant effects are seen in the empty loop, where the atmospheric response to $E_C = 5$ keV electrons causes complex line profiles that are redshifted to large Doppler velocities. Through investigation of the intensity formation, we have shown that the spectral lines are highly affected by the plasma flows through the χ_v/τ_v term. The increase in coronal and TR temperatures leads to the strong downflows responsible for the redshifts, and it is a result of the electrons depositing most of their energy in those regions. The large upflows (negative velocities in Fig. 2d) are in agreement with the findings by Testa et al. (2014) and Reep et al. (2015), who showed that low-energy electrons could drive ‘explosive evaporation’. The atmospheric response to 5 keV electrons strongly depends on the sites where the energy is deposited.

The stopping depth of the electrons in the $E_C = 10$ and 15 keV energy distributions is deeper into the atmosphere, mainly in the TR and chromosphere. However, we note that the 10 keV electrons in the 3 MK loop deposit more energy in the corona and TR, similarly to the 5 keV models. A portion of the electrons is able to travel to the chromosphere, where the increase in chromospheric emission during the heating phase is significantly larger than in the 5 keV models. The height where the energy is deposited strongly depends on the density of the loop, which becomes apparent when comparing the 10 keV empty and dense loop models. The increased density causes significantly more electrons from the distribution to collide with the ambient plasma at great heights. The atmospheric response to the 10 keV electrons in the dense loop therefore resembles that of the 5 keV models, while the response to intermediate-energy electrons in the empty loop is more similar to the high-energy models.

A range of energies is represented in the electron energy distributions (see Fig. 1), where the input parameters are free and chosen based on observations. The advantage of 1D flare modelling with RADYN is the ability to study specific energetic events in an isolated system. The atmospheric response to the electron beams provides information on features that we can look for in more advanced simulations, such as those pro-

duced with the radiative magnetohydrodynamic (MHD) Bifrost code (Gudiksen et al. 2011). We previously introduced a Bifrost model including accelerated particles by magnetic reconnection, where the reconnection sites were found by identifying locations where the magnetic topology is not conserved (Bakke et al. 2018). Frogner et al. (2020) further developed the modelling of the accelerated particles, and found that the magnetic topology is a significant factor when determining both the amount of accelerated electrons and their energy. In this type of Bifrost models, the magnetic reconnection, and hence particle acceleration, occurs over extended regions. An advantage with such models is the more realistic 3D modelling. However, with the complex configuration of Bifrost models, it is more difficult to control the parameter space of the simulations. RADYN follows the traditional approach of modelling flares (with the injection of electrons at the top of the loop), hence we can more easily isolate the details of the event. RADYN is also relatively quick to run, which is beneficial when surveying an extensive parameter space to investigate the effects of small-scale events on a variety of spectral lines.

The signatures in the chromospheric spectra give an indication of what to look for in observations. Complex line profiles as the ones shown in Fig. 4 using the 5 keV empty loop model have not been reported in the literature so far, but might suggest heating by non-thermal electrons if observed. The inclusion of the Ca II and H I lines to the diagnostics gives potential for observing small-scale events with ground-based telescopes, such as the Swedish 1-m Solar Telescope (SST; Scharmer et al. 2003) and the Daniel K. Inouye Solar Telescope (DKIST; Rimmele et al. 2020). With the CHROMIS instrument installed at the SST, it is possible to sample the Ca II H and K and H β lines with high spectral resolution. Ground-based telescopes generally allow for higher spatial resolution as compared to millimetre observations and (extreme-)UV diagnostics observed from space. This could provide tighter constraints on the spatial dimensions of the strand widths and temporal variability. We also note that Mg II h and Ca II K appear to be more sensitive to events at the top of the chromosphere than Ca II 854.2 nm, and coordinated

observations with SST and IRIS, for instance, would be beneficial to provide more constraints on nanoflares. A comparison of observations to our numerical results, as well as Bifrost electron beam simulations, will be explored in future work. Testa et al. (2020) found that Mg II profiles from RADYN nanoflare models showed similarities to what was observed at the footpoints of AR coronal loops with IRIS. They also found that the Mg II triplet is an important diagnostic for non-thermal electrons due to its sensitivity to heating in the lower atmosphere. We will therefore include the Mg II triplet in future spectral line analysis.

In this paper, we have extended the spectral line diagnostics of Polito et al. (2018) and Testa et al. (2020) to include additional chromospheric lines. We have established that non-thermal electrons from small-scale events are able to affect line features through strong plasma flows as a response to the electrons depositing their energy in the corona and TR, but also through energy deposited directly in the chromosphere. We show that the strong chromospheric lines in the visible can also be used as diagnostics of nanoflare-size events.

Acknowledgements. This research was supported by the Research Council of Norway, project number 250810, 325491, through its Centres of Excellence scheme, project number 262622, and through grants of computing time from the Programme for Supercomputing. P.T. was supported by contract 8100002705 from Lockheed-Martin to SAO, NASA contract NNM07AB07C to the Smithsonian Astrophysical Observatory, and NASA grant 80NSSC20K1272. V.P. and B.D.P. were supported by NASA contract NNG09FA40C (IRIS).

References

- Allred, J., Kowalski, A., & Carlsson, M. 2015, *AAS/AGU Triennial Earth-Sun Summit*, 1, 302.07
- Bakke, H., Frogner, L., & Gudiksen, B. V. 2018, *A&A*, 620, L5
- Björger, J. P., Sukhorukov, A. V., Leenaarts, J., et al. 2018, *A&A*, 611, A62
- Brown, J. C. 1971, *Sol. Phys.*, 18, 489
- Carlsson, M., & Stein, R. F. 1992, *ApJ*, 397, L59
- Carlsson, M., & Stein, R. F. 1995, *ApJ*, 440, L29
- Carlsson, M., & Stein, R. F. 1997, *ApJ*, 481, 500
- Carlsson, M., Leenaarts, J., & De Pontieu, B. 2015, *ApJ*, 809, L30
- Cooper, K., Hannah, I. G., Grefenstette, B. W., et al. 2021, *MNRAS*, 507, 3936
- De Pontieu, B., Title, A. M., Lemen, J. R., et al. 2014, *Sol. Phys.*, 289, 2733
- Dere, K. P., Landi, E., Mason, H. E., Monsignori Fossi, B. C., & Young, P. R. 1997, *A&AS*, 125, 149
- Dorfi, E. A., & Drury, L. O. 1987, *J. Comput. Phys.*, 69, 175
- Emslie, A. G. 1978, *ApJ*, 224, 241
- Frogner, L., Gudiksen, B. V., & Bakke, H. 2020, *A&A*, 643, A27
- Glesener, L., Krucker, S., Duncan, J., et al. 2020, *ApJ*, 891, L34
- Gudiksen, B. V., Carlsson, M., Hansteen, V. H., et al. 2011, *A&A*, 531, A154
- Gustafsson, B. 1973, *Uppsala Astron. Obs. Ann.*, 5
- Hannah, I. G., Hudson, H. S., Battaglia, M., et al. 2011, *Space Sci. Rev.*, 159, 263
- Holman, G. D., Aschwanden, M. J., Aurass, H., et al. 2011, *Space Sci. Rev.*, 159, 107
- Leenaarts, J., Pereira, T. M. D., Carlsson, M., Uitenbroek, H., & De Pontieu, B. 2013a, *ApJ*, 772, 89
- Leenaarts, J., Pereira, T. M. D., Carlsson, M., Uitenbroek, H., & De Pontieu, B. 2013b, *ApJ*, 772, 90
- Milkey, R. W., & Mihalas, D. 1974, *ApJ*, 192, 769
- Parker, E. N. 1988, *ApJ*, 330, 474
- Pereira, T. M. D., & Uitenbroek, H. 2015, *A&A*, 574, A3
- Pereira, T. M. D., Carlsson, M., De Pontieu, B., & Hansteen, V. 2015, *ApJ*, 806, 14
- Polito, V., Testa, P., Allred, J., et al. 2018, *ApJ*, 856, 178
- Reep, J. W., Bradshaw, S. J., & Alexander, D. 2015, *ApJ*, 808, 177
- Rimmele, T. R., Warner, M., Keil, S. L., et al. 2020, *Sol. Phys.*, 295, 172
- Scharmer, G. B., Bjelksjö, K., Korhonen, T. K., Lindberg, B., & Petterson, B. 2003, in *Innovative Telescopes and Instrumentation for Solar Astrophysics*, eds. S. L. Keil, & S. V. Avakyan, *SPIE Conf. Ser.*, 4853, 341
- Shine, R. A., Milkey, R. W., & Mihalas, D. 1975, *ApJ*, 199, 724
- Testa, P., De Pontieu, B., Martínez-Sykora, J., et al. 2013, *ApJ*, 770, L1
- Testa, P., De Pontieu, B., Allred, J., et al. 2014, *Science*, 346, 1255724
- Testa, P., Polito, V., & De Pontieu, B. 2020, *ApJ*, 889, 124
- Uitenbroek, H. 2001, *ApJ*, 557, 389
- Vardavas, I. M., & Cram, L. E. 1974, *Sol. Phys.*, 38, 367
- Wright, P. J., Hannah, I. G., Grefenstette, B. W., et al. 2017, *ApJ*, 844, 132

Paper II

Accelerated particle beams in a 3D simulation of the quiet Sun. Lower atmospheric spectral diagnostics

Helle Bakke, Lars Frogner, Luc Rouppe van der Voort, Boris V. Gudiksen, Mats Carlsson






A&A 675, A103 (2023)

DOI:10.1051/0004-6361/202346765



Accelerated particle beams in a 3D simulation of the quiet Sun

Lower atmospheric spectral diagnostics

H. Bakke^{1,2} , L. Frogner^{1,2} , L. Rouppe van der Voort^{1,2} , B. V. Gudiksen^{1,2} , and M. Carlsson^{1,2} 

¹ Institute of Theoretical Astrophysics, University of Oslo, PO Box 1029 Blindern, 0315 Oslo, Norway
e-mail: helle.bakke@astro.uio.no

² Rosseland Centre for Solar physics, University of Oslo, PO Box 1029 Blindern, 0315 Oslo, Norway

Received 28 April 2023 / Accepted 2 June 2023

ABSTRACT

Context. Nanoflare heating through small-scale magnetic reconnection events is one of the prime candidates to explain heating of the solar corona. However, direct signatures of nanoflares are difficult to determine, and unambiguous observational evidence is still lacking. Numerical models that include accelerated electrons and can reproduce flaring conditions are essential in understanding how low-energetic events act as a heating mechanism of the corona, and how such events are able to produce signatures in the spectral lines that can be detected through observations.

Aims. We investigate the effects of accelerated electrons in synthetic spectra from a 3D radiative magnetohydrodynamics simulation to better understand small-scale heating events and their impact on the solar atmosphere.

Methods. We synthesised the chromospheric Ca II and Mg II lines and the transition region Si IV resonance lines from a quiet Sun numerical simulation that includes accelerated electrons. We calculated the contribution function to the intensity to better understand how the lines are formed, and what factors are contributing to the detailed shape of the spectral profiles.

Results. The synthetic spectra are highly affected by variations in temperature and vertical velocity. Beam heating exceeds conductive heating at the heights where the spectral lines form, indicating that the electrons should contribute to the heating of the lower atmosphere and hence affect the line profiles. However, we find that it is difficult to determine specific signatures from the non-thermal electrons due to the complexity of the atmospheric response to the heating in combination with the relatively low energy output ($\sim 10^{21}$ erg s⁻¹). Even so, our results contribute to understanding small-scale heating events in the solar atmosphere, and give further guidance to future observations.

Key words. Sun: chromosphere – Sun: transition region – Sun: flares – magnetic reconnection – radiative transfer

1. Introduction

Nanoflares are heating events associated with small-scale magnetic reconnection in the solar atmosphere. They release energy in the range 10^{24} – 10^{25} erg, and they are believed to occur frequently throughout the atmosphere. The nanoflare heating mechanism is one of the prime candidates in understanding why the corona is heated to millions of Kelvin (Parker 1988). It is generally accepted that flare energy is transported by electrons accelerated to non-thermal energies as magnetic field lines reconnect. The accelerated electrons transfer energy to the ambient plasma through Coulomb collisions as they travel along the magnetic field (Brown 1971; Emslie 1978; Holman et al. 2011), leaving observable signatures in the spectral lines that form in the sites where the energy is deposited. Signatures of non-thermal electrons are found in observed hard X-ray spectra from active region flares. However, X-ray observations of small-scale events with nanoflare energies are rare because the signatures are typically below the detection threshold (although, see e.g., Wright et al. 2017; Glesener et al. 2020; Cooper et al. 2021). As a result, the presence and properties of nanoflares in the solar atmosphere remain poorly known.

Heating signatures from energetic events in the corona are difficult to observe directly, as the high conductivity of coronal plasma has a tendency to smear the signatures out. It is therefore beneficial to look for signatures of heating release in the

atmospheric layers that are responsive to heating, such as the transition region (TR) and chromosphere. Non-thermal electrons accelerated by magnetic reconnection in the corona collide with the dense TR and chromospheric plasma, giving rise to changes in temperature and density. However, looking for specific signatures is problematic as nanoflares are difficult to observe. Through numerical simulations, Testa et al. (2014) have found that non-thermal electrons are necessary to reproduce blueshifts in the Si IV 140.3 nm line observed with the Interface Region Imaging Spectrograph (IRIS; De Pontieu et al. 2014) in small heating events at the footpoints of transient hot loops. By exploring a wide range of parameters, Polito et al. (2018) have carried out an extensive numerical investigation to better understand and interpret TR observations, and Bakke et al. (2022) have extended the analysis to include spectral lines that form deeper in the atmosphere and are readily accessible by ground-based telescopes. In the latter, the analysis of chromospheric spectra in 1D simulations of nanoflares showed that the lines forming deeper in the chromosphere experience similar effects as the lines forming higher up. Testa et al. (2020) have further demonstrated that observations of high variability (≤ 60 s) at the footpoints of hot coronal loops (~ 8 – 10 MK) in active region (AR) cores provide powerful diagnostics of the properties of coronal heating and energy transport when combined with numerical simulations.

In this work, we investigate the effect of accelerated electrons in a 3D radiative magnetohydrodynamics (MHD) simulation by

analysing synthetic chromospheric Ca II 854.2 nm, Ca II H and K, and Mg II h and k spectral lines as well as the TR Si IV resonance lines. The simulation is based on the 3D MHD Bifrost model introduced in Bakke et al. (2018), which has been further developed in Frogner et al. (2020) and Frogner & Gudiksen (2022) to include a more accurate method for calculating the electron beam heating. We explore the impact of non-thermal electrons by comparing the spectral line analysis from different regions that are both subject and not subject to beam heating. In the analysis we investigate the Doppler shifts of the spectra and the formation of line intensity.

2. Method

2.1. Bifrost simulation

The numerical simulation was performed using the Bifrost code (Gudiksen et al. 2011), which solves the resistive MHD partial differential equations in 3D, with radiative transfer and field-aligned thermal conduction accounted for in the energy equation. In the photosphere and lower chromosphere, Bifrost solves the optically thick radiative transfer equation with scattering (Hayek et al. 2010). In the upper chromosphere and TR, it approximates non-LTE radiative losses based on parameterised results from 1D radiative hydrodynamic simulations (Carlsson & Leenaarts 2012). Finally, it calculates optically thin radiative losses in the corona.

Bifrost was developed with a high degree of modularity, allowing users to extend the code with additional physics. In Bakke et al. (2018), we presented a method for treating energy transport by accelerated electrons in Bifrost simulations, which we expanded upon and discussed in depth in Frogner et al. (2020) and Frogner & Gudiksen (2022). The first step of the method is to detect locations where the magnetic field reconnects using a criterion for reconnection in MHD theory (Biskamp 2005). The second step is to estimate the energy distributions of the non-thermal electrons expected to be accelerated at each reconnection site. We assume that the distribution is a power-law, with a lower cut-off energy E_c corresponding to the intersection of the power-law with the local thermal distribution. The lower cut-off energy is not fixed, but is roughly proportional to temperature (for example, 10^6 K corresponds to a lower cut-off energy of the order of 1 keV). We determine the total non-thermal energy flux assuming that a fixed fraction p of the released magnetic energy, which otherwise would be converted entirely into resistive heating, goes into accelerating electrons. The value of $p = 0.2$ was chosen based on flare observations suggesting that typical values of p range from 10% (Emslie et al. 2004, 2012) up to 50% (Lin & Hudson 1971). Finally, we leave the power-law index δ as a free global parameter. This parameter largely affects the resulting distribution of deposited electron beam energy. We used a value of $\delta = 6$, which has a faster rate of deposited energy compared to smaller values. We note that a larger δ leads to a smaller penetration depth of the beam (Allred et al. 2015). The value of δ is supported by observational evidence showing an increase in power-law index with decreasing flare energy (Hannah et al. 2011). A higher value of δ is also motivated by the 1D flare simulations analysed in Bakke et al. (2022), where $\delta = 7$ was used for the non-thermal electron energy distribution. The final step is to trace the trajectory of each non-thermal electron beam along the magnetic field while computing the heating of the local plasma due to Coulomb collisions along the way. For this, we use an analytical expression accounting for the systematic velocity change of

beam particles due to collisions with ambient hydrogen atoms and free electrons (Emslie 1978; Hawley & Fisher 1994). During the simulation, we continually computed the transfer of energy by the beams in this way and included it as a term in the MHD energy equation.

The particular atmospheric simulation considered in this paper encompasses a horizontal area of 24×24 Mm and a vertical span from 2.5 Mm below the photosphere to 14.3 Mm above it, in the corona. The simulation has a resolution of $768 \times 768 \times 768$ grid cells, with a uniform grid cell extent of 31 km in the horizontal directions and uneven vertical grid cell extents that vary with height in the atmosphere. Due to the need to resolve sudden local variations near the transition region, the grid cells are about 12 km tall between the photosphere and the height of 4 Mm. From this region, the vertical grid cell extent increases evenly to 21 km at the bottom of the simulation box and to 80 km at the top. In the simulation, heating at the bottom boundary in combination with radiative cooling in the photosphere produces convective motions. The chromosphere and corona are heated by magnetic reconnection and acoustic shocks resulting from these motions. At this point, the Bifrost simulation qualifies as rather quiet, and electron beams from this level of reconnection can be regarded as weak. In order to perturb the system with more magnetic energy and produce more energetic reconnection events, we introduced a large scale magnetic flux emergence. To emulate flux emergence, a sheet with magnetic field strength of 2000 G oriented in the y -direction was injected at the bottom boundary. As it rose up through the convection zone and coalesced in the convective downflow regions, the injected field organised into a largely bipolar loop system pushing up on the ambient x -directed magnetic field that was originally present in the corona. Reconnection between the ambient and injected field then resulted in minor energy release and particle acceleration events throughout the corona. This setup made the simulation more active, but still relatively quiet as compared to solar active regions with high flaring activity. We note that the original setup of this Bifrost simulation was developed and used by Hansteen et al. (2019), with the aim of studying the generation of Ellerman bombs and UV bursts through flux emergence.

For this paper, we consider a series of 36 snapshots with 1 s intervals, where the simulation time step is 10^{-3} s. This simulation starts 8220 s after the magnetic flux sheet has been injected at the bottom boundary. The vertical component of the magnetic field in the photosphere at this time can be seen in Fig. 1, where $t' = 0$ s is the first time step where the electrons are injected. The total power of accelerated electrons in a single simulation snapshot is roughly 10^{24} erg s^{-1} , and individual beams along the magnetic field produce approximately 3×10^{21} erg s^{-1} of non-thermal power (Frogner et al. 2020). A typical small-scale beam heating event is estimated to release 10^{20} – 10^{24} erg of non-thermal energy in the lower atmosphere assuming that the event lasts around 100 s. With 36 s of simulation time, we can assume that the energy released by heating events is on the lower end of this range, and hence a few orders of magnitudes less than the typical nanoflare energy (which is about 10^{24} – 10^{25} erg). But even though the events are weak, they are highly abundant, and a significant number of small beam heating events are likely to occur in the chromosphere at any given time. We note that it is difficult to provide a meaningful number of events as they have a tendency to lose their identity in the simulation due to the relatively low energy released. However, see Kanella & Gudiksen (2017) for a method of identifying coronal heating events in a Bifrost simulation by detecting 3D volumes of high Joule heating to find locations with current sheets.

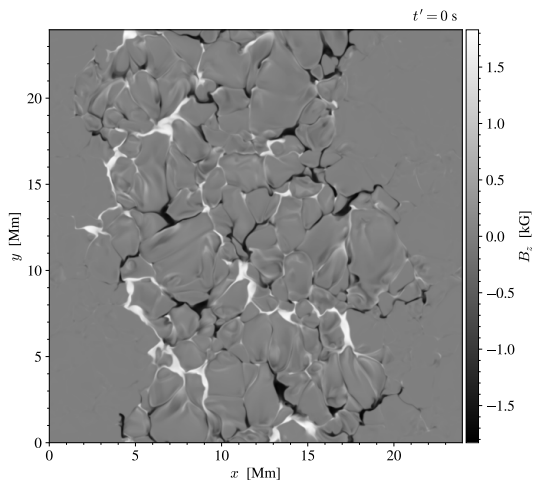


Fig. 1. Vertical magnetic field B_z in the photosphere at $t' = 0$ s (8220 s after the magnetic flux sheet has been injected).

2.2. Spectral synthesis with RH

The spectral lines were synthesised using the RH1.5D radiative transfer code (Uitenbroek 2001; Pereira & Uitenbroek 2015), which calculates spectra from 1D, 2D or 3D numerical simulations on a column-by-column basis. RH1.5D solves the non-LTE radiative transport for spectral lines in partial redistribution (PRD), which is important in the synthesis of chromospheric lines where a more accurate treatment of photon scattering is required. While PRD is not strictly necessary in the synthesis of all our chosen spectra, RH1.5D can still be employed as a general non-LTE code. In general, PRD is assumed in the synthesis of Mg II h and k (Milkey & Mihalas 1974; Leenaarts et al. 2013a,b) and Ca II H and K (Vardavas & Cram 1974; Shine et al. 1975; Bjørgen et al. 2018), but is less important for Ca II 854.2 nm and the Si IV resonance lines.

Each atmosphere from the Bifrost snapshots was used as input to the RH code. We did not include a micro-turbulence term to the spectral synthesis as we wanted to focus on the effect from velocities in the Bifrost simulation. The z -axis of the input atmospheres includes the heights from the surface to the corona, excluding the convection zone as it is not relevant for the line synthesis. We selected all columns in x - and y -direction when synthesising the spectra from the main snapshot at $t' = 28$ s analysed in this study, covering a domain of $768 \times 768 \times 670$ pixels. The synthetic spectra for the entire time series were calculated using a coarser grid ($384 \times 384 \times 670$ pixels) for the model atmospheres in order to reduce the computation time. The coarser grid does not affect the spectral analysis as the level of change from one grid cell to its neighbouring ones is almost negligible. A similar coarser sampling of a Bifrost simulation domain was performed in Leenaarts et al. (2013b). We used the default 5 level-plus-continuum H I and Ca II atoms, the 10 level-plus-continuum Mg II atom from Leenaarts et al. (2013a), and the 30 level-plus-continuum Si IV atom from Kerr et al. (2019). The latter was used to allow the Si IV resonance lines to form under optically thick conditions, as the model silicon atom includes potential opacity effects. It is common to assume that the Si IV emission is formed under optically thin conditions, and hence compute

the emissivity without calculating the full radiative transfer. Through 1D flare modelling, Kerr et al. (2019) found that optical depth effects are considerable in the produced Si IV emission, and that the lines can form under optically thick conditions even for weaker flares with electron energy flux down to $F \approx 5 \times 10^9$ erg cm $^{-2}$ s $^{-1}$. We note that the model atom was constructed for use on simulated flares in RADYN (Carlsson & Stein 1992, 1995, 1997; Allred et al. 2015), a 1D radiative transfer code that allows for flare investigation in an isolated system. The model atom employs a photospheric value $A_{\text{Si}} = 7.51$ for the silicon abundance (Asplund et al. 2009), even though other work (e.g., Olluri et al. 2015; Martínez-Sykora et al. 2016) have argued in favour of using coronal abundances for silicon and other low first ionisation potential (low-FIP) elements. Using coronal abundances is based on the findings that low-FIP elements tend to be overabundant in the TR and corona (Laming 2004). However, Warren et al. (2016) have shown that low-FIP elements have a composition that is close to that of the photosphere during impulsive heating events. In Bifrost, it is possible that the model silicon atom is more accurate in regions that are subject to electron acceleration, but also at the sites where the electron energy is deposited. However, we keep in mind that the silicon abundance might not be accurate in areas that are not subject to heating.

The synthetic spectra were calculated for 36 s, corresponding to 36 Bifrost snapshots with a 1 s time interval. IRIS observations of TR moss show that the lifetime of short-lived brightenings resulting from coronal nanoflare heating at the footpoints of hot transient coronal loops varies between 10–30 s (Testa et al. 2013, 2014, 2020). With the Bifrost time series, we should be able to study the effects of non-thermal electrons on a similar timescale. However, we note that with the current energy distribution for the non-thermal electrons, it is difficult to obtain a strong signal in the synthetic spectra.

2.3. Optically thin calculation of Si IV emission

While the RH spectral line synthesis allows for the Si IV resonance lines to form under both optically thick and thin conditions, we also include a more straightforward approach to calculate the Si IV emission under optically thin conditions in order to compare potential differences and put further constraints on the interpretation of observations. The approach we used is similar to that of Olluri et al. (2015), where we calculated emissivities for the relevant Si IV energy transitions using atomic data from the CHIANTI database (Dere et al. 1997; Del Zanna et al. 2021). We did this for a range of temperatures and electron densities representative of the conditions in the corona and upper TR of the simulated atmosphere to create a lookup table enabling us to efficiently obtain the emissivity at every location in the simulation domain. We note that emissivities for temperatures lower than 10 000 K are set to zero in CHIANTI. In this approach, we used the coronal abundance $A_{\text{Si}} = 8.10$ (Feldman 1992). To determine the intensities formed in the optically thin regime as it emerges from the atmosphere, we integrated the emissivities in each vertical column of the atmosphere. We also computed the Doppler shift and width of the synthetic spectral line by evaluating the first and second moment of the locally emitted line profile with respect to Doppler shift from the line centre, and integrated this over height. We assume that the locally emitted radiation has a Gaussian spectral profile with thermal broadening and a Doppler shift depending on the local plasma velocity. The optically thin calculation is also significantly cheaper in computational terms than the RH spectral synthesis.

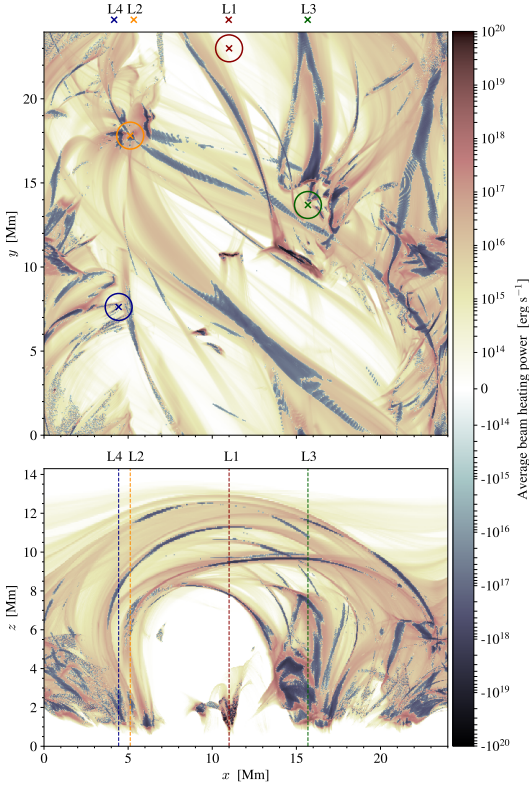


Fig. 2. Integrated average beam heating power along the z -axis (upper panel) and y -axis (lower panel) of the Bifrost simulation snapshot at $t' = 28$ s. The blue regions represent where a fraction p of the reconnection energy is being injected into the accelerated electrons, while the orange regions show where the non-thermal electrons deposit their energy and heat the plasma. The coloured circles in the upper panel are the areas of interest, while the crosses (upper panel) and dashed lines (lower panel) mark the specific locations analysed in detail (L1, L2, L3, and L4).

2.4. Contribution function to the line intensity

The spectral diagnostics consisted of analysing the contribution function to the emergent intensity. The contribution function can be used to explore which parts of the atmosphere contributes to the line formation. Following [Carlsson & Stein \(1997\)](#), the contribution function was calculated as

$$C_{I_\nu}(z) \equiv \frac{dI_\nu(z)}{dz} = S_\nu \tau_\nu e^{-\tau_\nu} \frac{\chi_\nu}{\tau_\nu}. \quad (1)$$

The first term on the right-hand side gives the total source function S_ν . Here, S_ν is dependent on frequency because we assume PRD. The next term is the optical depth factor $\tau_\nu e^{-\tau_\nu}$, which represent the Eddington-Barbier part of the contribution function. The optical depth factor has a maximum at $\tau_\nu = 1$. The final term, χ_ν/τ_ν , is the ratio of the opacity over optical depth. The term is responsible for line asymmetries due to its sensitivity to velocity gradients in the atmosphere. In the presence of strong velocity gradients, the opacity is typically large at small optical depths, and χ_ν/τ_ν is the dominant factor in the contribution function.

2.5. Locations of interest

The locations of interest were selected based on the electron acceleration regions. Figure 2 shows the net electron beam heating power integrated vertically (upper panel) and horizontally (lower panel) over the simulation domain. The electrons are mostly accelerated along the magnetic field, where negative average beam heating power (blue regions) indicates where part of the energy is transported away from the reconnection site. As shown in the upper panel, we have chosen three areas (orange, green, and blue circles) at magnetic field footpoints that are associated with field lines where electrons are accelerated, and a reference area (red circle) without beam impact. The crosses (upper panel) and dashed lines (lower panel) represent the specific locations L1, L2, L3, and L4 that we subsequently analyse in detail.

The specific locations were found using CRISPEX ([Vissers 2012](#)), which is a widget based tool developed to browse and analyse large observational data sets. However, CRISPEX can also be used to analyse synthetic spectra from simulations by creating a data cube that is readable by the tool. We formatted the synthetic Mg II k, Ca II K, and Si IV 140.3 nm lines from Bifrost at $t' = 28$ s as a multidimensional data cube that is readable by CRISPEX, and chose locations based on the intensity and complexity of the profiles by browsing through the spectra within the different areas. We further note that the prominent low altitude current sheet at $(x, y) = (10, 11)$ was found to produce an Ellerman bomb and UV burst in the detailed analysis by [Hansteen et al. \(2019\)](#).

3. Results

3.1. Evolution of the Bifrost atmosphere

Figure 3 shows the time evolution of temperature T , vertical velocity v_z , and electron number density n_e in the Bifrost simulation at 1 s intervals. The rows represent the different quantities, while the columns represent the specific locations shown in Fig. 2. The temperature in the four different panels does not experience significant increases or decreases over time. However, the atmospheric structure varies from location to location. This is better seen in Fig. 4, showing the temperature at a vertical cut in the xz -plane taken at the location of the y -coordinate of L1, L2, L3, and L4, at a single instance in time ($t' = 28$ s).

L1 is located within the flux emergence region of the simulation (see Fig. 4a). The magnetic bubble does not have a significant temperature rise until the canopy is reached around $z = 6.8$ Mm, which can be seen as the TR in Fig. 3a. L1 is also located in a region without beam impact, as can be seen in Fig. 3m where $Q_b = 0$ over the entire duration of the simulation. L2, L3, and L4 are located at magnetic field footpoints, where the TR and temperature rise to coronal values are located at lower altitude. Panel b in Fig. 3 shows that the TR is gradually pushed upwards over time. This is happening in the height where electrons are both accelerated and depositing their energy (see panel n). However, both the velocity and electron number density are relatively unchanged over the duration of the simulation, making it difficult to conclude that the moving TR is caused by the electrons only. If the latter was the case, we would expect the electrons that deposit their energy at 1 Mm to accelerate the dense plasma, causing upflowing (negative) velocities that move the TR to greater heights. Panel n shows that the electrons contribute to the thermodynamics of the TR and chromosphere, but the level of heating available in the simulation combined with the complex dynamics of the Bifrost atmosphere causes the effect from the deposited electron beam energy to blend and smear out.

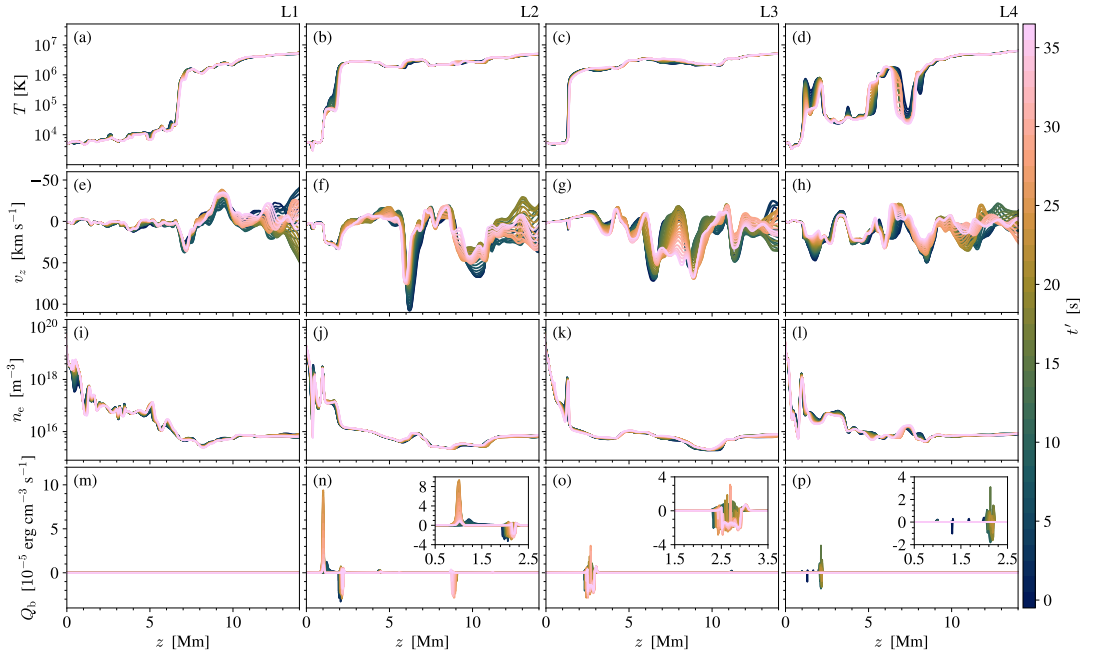


Fig. 3. Evolution of temperature T , vertical velocity v_z , electron number density n_e , and beam heating rate Q_b in the Bifrost simulation. The quantities are plotted in the range $z \in [0, 14]$ Mm at 1 s intervals for the duration of the time series. Each column represents the specific locations (L1, L2, L3, and L4) from the chosen areas. Negative (positive) velocities correspond to upflows (downflows). The insets in panels n–p show the electron beam heating in a sub-region, where the y -axes are limited to better show the details of the variations in Q_b .

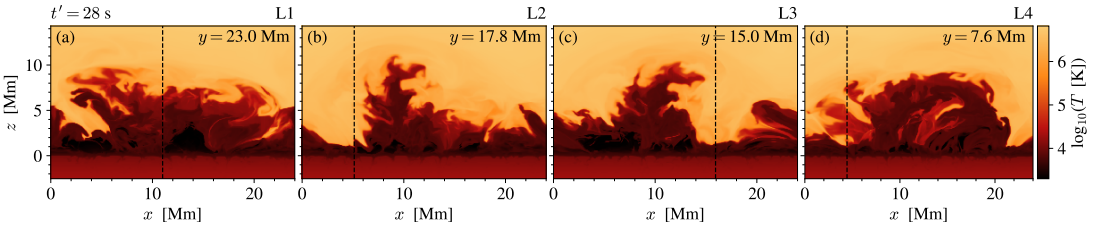


Fig. 4. Vertical cut in the xz -plane of the temperature structure at $t' = 28$ s. The vertical cut is taken at the location of the y -coordinate of L1, L2, L3, and L4. The dashed lines are drawn at the x -coordinate of the different locations.

This makes it difficult to recognise an unambiguous footprint left by the electrons.

The temperature at L3 (panel c) does not change significantly over the duration of the simulation. The TR is located around 1.5 Mm, and panels g and k show that at this height there is a weak plasma upflow and an increase in electron number density. We note that the change over time is so small that the line of the last time step covers small variations. There are generally more visible changes over time in the corona compared to the lower atmosphere. The beam heating rate in panel o shows that the electrons are both accelerated and depositing their energy between 2.3–3.1 Mm, which is in the corona. This is because the cut-off energy E_C at coronal heights is low (around 1 keV), and the electrons lose most of their energy through interactions with the coronal plasma. This leads us to suspect that particular features in the synthetic spectra are not caused by the electrons, as signature are potentially only visible in coronal spectral

lines and we focus here on spectral lines formed deeper in the atmosphere.

The temperature structure at L4 (see panel d in Figs. 3 and 4) is much more complex compared to the other locations. The cool plasma from the magnetic bubble intersects the column at several different heights, making the atmospheric structure difficult to analyse. Panel p shows that the beam heating rate is almost balanced out by the energy transferred to the electrons at the reconnection site. This means that the electrons that get accelerated at approximately 2 Mm deposit their energy right away, and do not contribute to any noticeable heating.

It is important to note that Fig. 3 shows the evolution of the atmosphere along the z -axis as seen from directly above, and not along the magnetic field lines. It is beneficial to choose pixel locations that are situated at magnetic field footpoints, as it is possible to detect spectral line signatures from electrons accelerated along the magnetic field connected to the particular

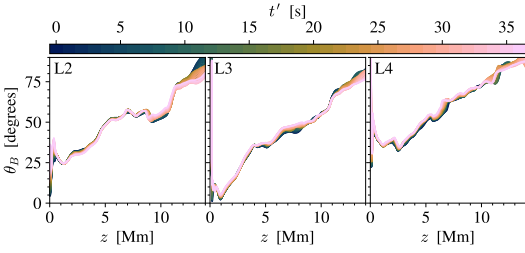


Fig. 5. Angle between the magnetic field and the vertical direction as a function of z for the entire Bifrost time series at the L2, L3, and L4 locations.

footpoint. However, because of the low cross-field transport of energy, we do not expect to see a direct effect of heating by accelerated electrons to travel along z because the effect is isolated to the specific field line where the heating is taking place. This is most likely not along z , as the field lines can at best only be regarded as straight at the very bottom of the atmosphere. This is better illustrated in Fig. 5, which shows the angle between the field and the vertical direction, calculated as

$$\theta_B \equiv \tan^{-1} \left(\frac{\sqrt{B_x^2 + B_y^2}}{|B_z|} \right) = \tan^{-1} \left(\frac{|B_h|}{|B_z|} \right), \quad (2)$$

at the magnetic footpoint locations (L2, L3, and L4) over the duration of the simulation. The figure shows that the angle increases with z , reaching 90° in the corona where the field lines are mostly horizontal. We note that at L3 and L4, the angle is 90° at $z = 0$ Mm because the magnetic field is highly complex in the convection zone, and the surface is not always located at exactly 0 Mm. This means that the magnetic field might not be aligned with z at 0 Mm, hence we see that the angle between z and the magnetic field is large rather than small. We also note that even though the angle is smaller at low heights (for instance around 1 Mm at L3), we are not able to see direct effects of non-thermal electrons potentially depositing their energy at these heights unless θ_B is zero. The heating signatures from the electron beams seen in Figs. 3n–p do not originate from vertical field lines that are aligned with z , but rather from reconnection events along the magnetic field connected to the footpoints.

3.2. Emission from synthetic spectra

Figure 6 represents the time evolution of the synthetic Ca II 854.2 nm, Ca II H, Mg II k, and Si IV 140.3 nm lines at the four selected locations, where we have added individual line profiles at $t' = 0$ s in each panel (orange line) to indicate what the spectra looks like. We note that our findings from the Ca II K, Mg II h, and Si IV 139.4 nm lines are similar to Ca II H, Mg II k, and Si IV 140.3 nm, respectively, hence these results are not shown. At L1, the minimum intensity of Ca II 854.2 nm at $t' = 28$ s is redshifted to a value between 1 and 2 km s^{-1} . The line seems to narrow towards the end of the simulation, but the general shape of the profile persists. At $t' = 28$ s, the minimum intensity of Ca II H and Mg II k and the single peak of Si IV 140.3 nm are redshifted to approximately $+5 \text{ km s}^{-1}$. The Ca II H line profile has increased emission in the blue wing and peak that becomes weaker over time, and there are small variations in the intensity of the line core and the red

peak. Over time, the minimum intensity of Mg II k and the single peak of Si IV 140.3 nm shifts periodically between approximately 0 km s^{-1} and $+5 \text{ km s}^{-1}$.

At the L2 location, the synthetic spectra are redshifted to varying degree. The minimum intensity of Ca II and Mg II are redshifted to a value between 1 and 2 km s^{-1} , while the Si IV line exhibits a much stronger redshift of the line. The latter is also significantly broadened, most likely due to the downflows at TR heights. Si IV forms higher in the atmosphere compared to the other spectra, and it is therefore more likely to be affected by the strong downflow seen between 1–2 Mm in Fig. 3f. In the beginning of the simulation, there is strong emission in the absorption feature so that the profile almost looks single peaked. As time progresses, the spectral profile becomes broader and the line is redshifted up to approximately $+30 \text{ km s}^{-1}$. From around 14 s, the red and blue peaks become more pronounced due to increased emission in these components. The Ca II lines show increased emission in the red wing that is due to the weak downflowing velocity around 0.4 Mm (see Fig. 3f). Over time, the red wings of the profiles become less broad. This feature is not seen in Mg II k, suggesting that the line forms slightly above this height.

The evolution of the spectra at L3 shows that the different spectra are experiencing oscillations. This behaviour is not detectable in the Ca II 854.2 nm panel, but further investigation show that this line, along with the other spectral lines, are subject to shock waves passing through the atmosphere. Around the formation height of Ca II 854.2 nm, we see temperature oscillations varying between 6500 and 6700 K, but the intensity amplitude is too small to see because of the large range between core minimum and wing maximum. Around the formation height of Ca II H, Mg II k, and Si IV 140.3 nm, the temperature oscillations vary between 7200 and 7800 K, 8500 and 11 000 K, and 8000 and 14 000 K, respectively. These values are low for Si IV, but we note that the temperatures are taken at the $\tau = 1$ height and that the contribution function covers a wider range. The temperature oscillations at the formation height of Si IV 140.3 nm exhibit the largest variation, hence the line is showing the strongest modulation in intensity. As the difference in minimum and maximum temperature decreases, the oscillating pattern in the intensity panels becomes weaker.

At L4, the Ca II spectral profiles have line cores at approximately 0 km s^{-1} at the beginning of the simulation that are redshifted to a value between 1 and 2 km s^{-1} over time. Both profiles are double peaked with a slightly more intense blue peak, but the Ca II 854.2 nm profile becomes single peaked and less intense as time progresses. The Ca II H profile keeps its double peaked shape, but the red peak becomes less intense from around 20 s. The Mg II k profile is similar to that of L2, with a blue peak that is more intense than the red peak and an absorption feature that is redshifted to a value between 1 and 2 km s^{-1} . At $t' = 12$ s, there is a sudden increase in intensity of the entire line profile that is also faintly seen in the Mg II k panel at the L2 location. This is due to a sudden increase in temperature at the formation height of the spectral line. The Si IV 140.3 nm line profile is severely broadened over the entire duration of the simulation. The initial profile (orange line) has a red and blue peak and a central reversal of the line core at approximately $+6 \text{ km s}^{-1}$ that has a higher intensity than the peaks. Similar to the L3 location, the Si IV line is subject to shock waves, where the temperature oscillations around its formation height vary between 26 000 and 29 000 K. At around 26 s, the temperature stabilises and the shape of the profile is similar to the initial profile ($t' = 0$ s).

Figure 6 shows that the strongest emission of the different spectra is found at L2. This location is promising in terms of

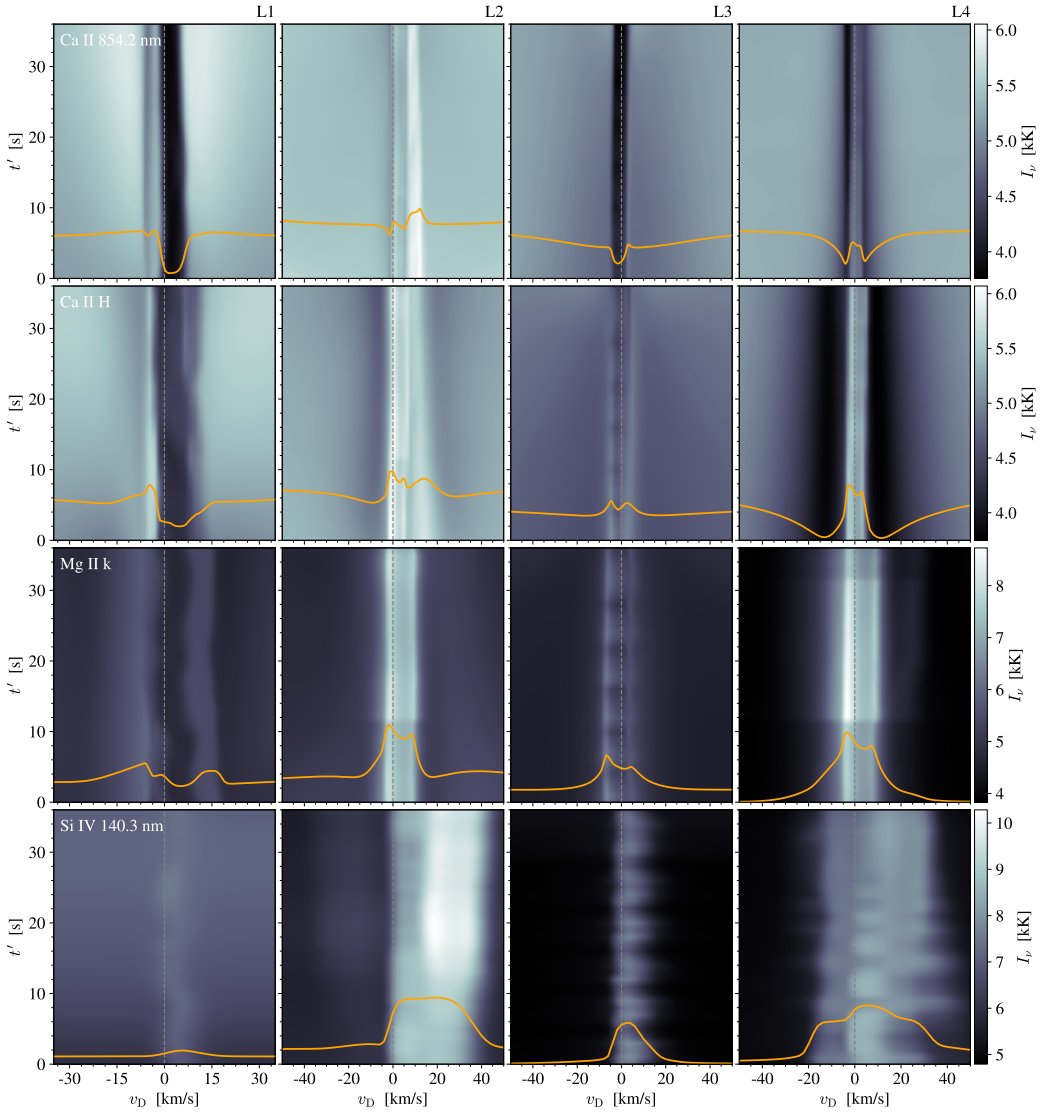


Fig. 6. Spectral evolution of Ca II 854.2 nm, Ca II H, Mg II k, and Si IV 140.3 nm at the locations of interest. The x -axes are in units of Doppler offset, where negative (positive) velocities indicate blueshifts (redshifts). The intensity is shown in units of brightness temperature. The orange line profiles are taken at $t' = 0$ s, where the highest (lowest) intensity of the profiles in each row corresponds to the maximum (minimum) intensity of the respective colourbars. We note that the intensity of Si IV 140.3 nm at the L1 location has a maximum of $I_v = 7$ kK in order to visually enhance the features of the relatively weak emission. The orange line profiles give a better indication of the difference in intensity across the Si IV row.

electron beam heating, as it is located at the footpoint that is connected to the longest coronal loops. The upper panel in Fig. 2 shows a large number of electron acceleration sites that are connected to the particular magnetic field footpoint. Even though the atmospheric response to the electrons has proven difficult to single out, the TR and chromospheric spectra might still be affected by the electrons depositing their energy along the loops. Figure 3n shows that the electrons along the line of sight deposit

most of their energy at TR and chromospheric heights, hence it is possible that the increased intensity seen in the L2 column of Fig. 6 is caused by local heating events.

3.3. Line formation

Figure 7 shows the Ca II 854.2 nm, Ca II H, and Mg II k line cores (top row) and $\tau = 1$ heights (bottom row) for the entire

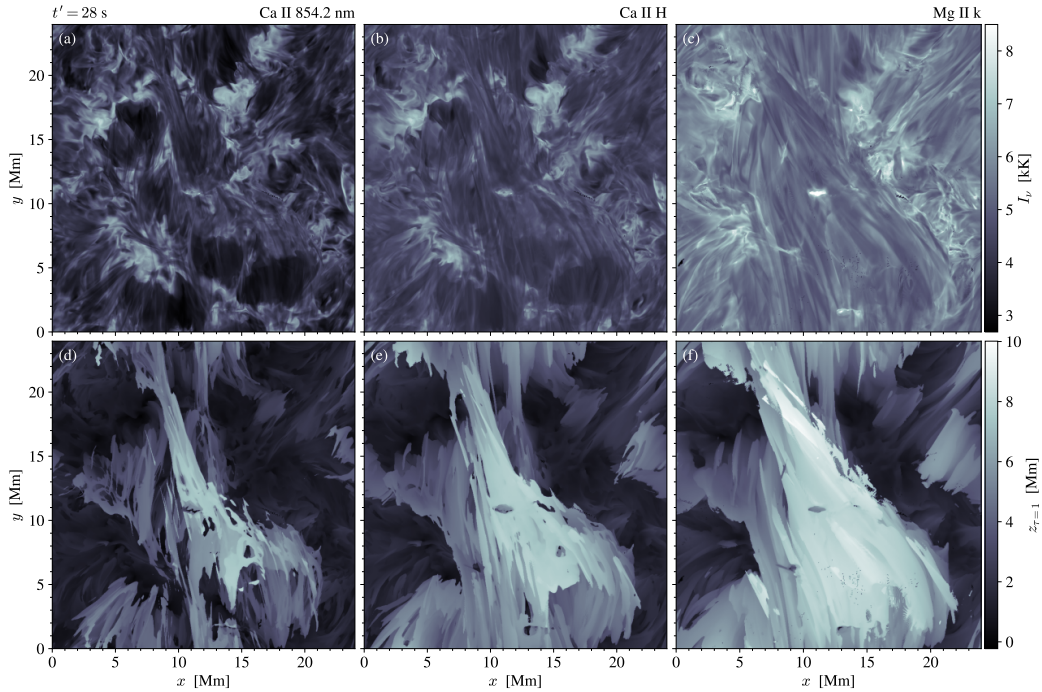


Fig. 7. Ca II 854.2 nm, Ca II H, and Mg II k nominal line core intensity (upper panels) and $\tau = 1$ heights (lower panels) at $t' = 28$ s. The colourbar of the intensity is clipped at 8.5 kK to emphasise the less bright features of the Ca II line cores.

simulation domain at a single snapshot in time ($t' = 28$ s). For simplicity, the line core is defined at $v_D = 0$ (see the dashed line in Fig. 6), even though the concept of a single line core vanishes when analysing complex atmospheres with multi-layered structures. We have chosen one of the later Bifrost snapshots so that the electrons will have affected the atmosphere for a longer duration (the electrons are present from $t' = 0$ s). Panels a–c show emission of the line cores at the magnetic field footpoints. The prominent current sheet at $(x, y) = (10, 11)$ has enhanced intensity in the line cores, see Hansteen et al. (2019) for a detailed analysis of the associated Ellerman bomb and UV burst emission. The emission from the spectral lines consists of long strands outlining the loops above the flux emergence region. This region is seen in panels d–f as the structure with the highest $z_{\tau=1}$ values. The structure is not as clearly outlined in panel d as in the other panels. This is because Ca II 854.2 nm forms deeper in the atmosphere, hence there is less emission of the line core above the flux emergence region. This is also seen in panel a, where there are fewer long emission strands outlining the magnetic bubble compared to the other upper panels. The Ca II H and Mg II k line cores form higher in the chromosphere, hence larger portions of the flux emergence region are outlined in the lower panels.

Figure 8 shows the integrated Si IV 140.3 nm intensity calculated using two different line synthesis approaches, as well as the ratio of the Si IV 139.4 nm to Si IV 140.3 nm line. In the left panel, the emission is calculated employing an optically thin approach using CHIANTI. The middle panel shows the intensity as output from the RH1.5D code allowing the Si IV resonance lines to form under both optically thin and thick conditions. The

intensity in both panels is normalised between 0 and 1 as we aim to do a qualitative comparison between the two intensity maps. A detailed quantitative comparison is difficult given differences between the two approaches in for example silicon abundance and temperature coverage. Hence Fig. 8 aims to visualise the impact of using a model atom that includes potential opacity effects. At first glance, the integrated intensity maps look similar. The general structure of the simulation is outlined by the intensity in both panels, with long strands spanning the flux emergence region. However, the structures are smoother in the left panel where the emission forms under optically thin conditions. The middle panel has features that appear to be below the loops that outline the flux emergence region. These features are either weak or not seen in the left panel, suggesting that it is necessary to include potential opacity effects when calculating Si IV synthetic spectra.

This is further supported by the right panel, which shows the ratio of the Si IV 139.4 nm to Si IV 140.3 nm line. In the optically thin limit the ratio should be equal to two, which is the ratio of their oscillator strengths. While the figure shows that most of the Si IV lines form under optically thin conditions, there are also darker areas where the ratio is below two. Similar results were discovered in Skan et al. (2023), where the wavelength integrated Si IV ratio was found to be between 1.6 and 1.8 at four different locations in a loop-like structure in a MURaM simulation. Our results show that a few of the darker areas where the ratio is below two stretches along the strands above the flux emergence region, which is consistent with their findings. Our results underline the risk of assuming that all Si IV emission forms under optically thin conditions in the solar atmosphere,

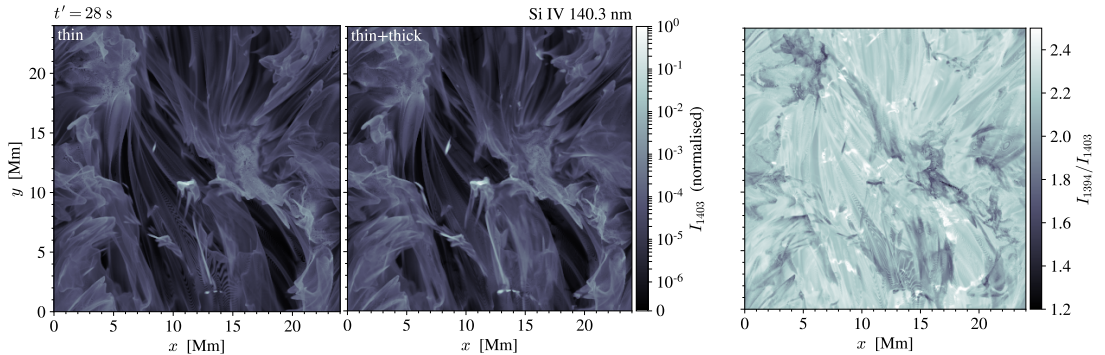


Fig. 8. Integrated Si IV 140.3 nm intensity calculated using CHIANTI (left, marked as optically thin) and RH1.5D (middle, marked as optically thin+thick), and ratio of the Si IV resonance lines (right). The three panels show their respective quantities at $t' = 28$ s. The integrated intensity maps are normalised between 0 and 1. The I_{1394}/I_{1403} ratio is calculated using the intensity output from the RH code.

and motivates our choice of using a more advanced approach when calculating the Si IV synthetic spectra.

3.4. Contribution function to the intensity

Figures 9–11 show four 2×2 diagrams of the intensity formation of Ca II 854.2 nm, Ca II H, Mg II k, and Si IV 140.3 nm at the L2, L3, and L4 locations at $t' = 28$ s. The panels in each subfigure represent the individual terms in Eq. 1 as well as the total contribution function to the line intensity.

Panels a and b in Fig. 9 show the intensity formation of Ca II 854.2 nm and Ca II H, respectively. There are two distinct downward velocity gradients that are reflected in the χ_v/τ_v term around 0.5 Mm and 1.05 Mm. The velocity gradient at 1.05 Mm seems to be located just above the maximum formation height of both spectral lines, and does not affect the contribution to the line intensity. The velocity gradient at 0.5 Mm (see also Fig. 3b) causes small emission features in the red wing, which can be seen in the emergent intensity profile that is shown in the lower right panels. The source function is coupled to the Planck function from the photosphere up to 0.3 Mm, where a narrow cold region is seen as a dip in the Planck function and as a darker band in S_v . Above the cold region, the source function is more closely following the Planck function again. For Ca II 854.2 nm, the functions decouple around 0.6 Mm, while for Ca II H this does not happen until 0.8 Mm. There is a strong increase in the Planck function, and hence also temperature, around 1 Mm. This gives rise to an increase in the source function around the maximum height of formation for the two lines. In panel a, the increase in source function is responsible for the central reversal of the Ca II 854.2 nm line core ($v_D = 0$), while the absorption feature at -1 km s^{-1} is caused by the decline in source function just above the narrow cold band. In panel b, the increase in source function gives rise to two emission peaks in the Ca II H intensity profile. The line core is formed at the maximum height of the optical depth unity curve ($z = 1$ Mm), where the central reversal is caused by the source function declining from the peak at around 0.95 Mm.

Figure 9c shows the intensity formation of Mg II k. The velocity gradients at 0.5 Mm and 1.05 Mm are reflected in the χ_v/τ_v term. The gradient at 0.5 Mm occurs below the formation height of the spectral profile, while the gradient at 1.05 Mm does not affect the total contribution function significantly because the

other terms are too small. In turn, the contribution function is dominated by the peak in source function, which is caused by the sudden increase in temperature seen as the Planck function. The central emission is caused by the increasing source function, while there is a shallow central absorption caused by a declining source function in line centre.

Figure 9d shows the formation of the Si IV 140.3 nm line. The downward velocity gradient at 1.05 Mm is clearly seen in the χ_v/τ_v term. The $\tau = 1$ height reaches high altitude, up to 1.7 Mm, at about $+35$ km s^{-1} Doppler offset. We note that all the spectral profiles presented in Fig. 9 are shifted to the red to varying degree. The strongest redshift is seen in Si IV, which has an average redshift of $+6$ km s^{-1} in the entire box. This is due to the overall positive velocity at the formation height shifting the profile to the red. In panel d, the strong velocity gradient also causes a broadening of the asymmetric profile. The contribution function panel in the lower right shows that the part of the profile formed above approximately 1 Mm is formed under optically thick conditions, as this is where the $\tau = 1$ curve follows the peak of the contribution function. Below 1 Mm on the other hand, the $\tau = 1$ curve departs from the contribution function, which means that the formation for this part of the line is under optically thin conditions.

Figure 10 represents the intensity formation of the four different spectral lines at the L3 location. Panel a shows that Ca II 854.2 nm is less affected by PRD than the other lines, as the source function, which appears like a horizontal band, shows little variation along the x -axis. The maximum height of the optical depth unity curve is slightly below the height of both the downward velocity gradient and the sudden temperature increase, hence these features do not contribute to the intensity and are not reflected in the emergent intensity profile. The intensity of the line is therefore just a map of the source function at optical depth unity. The source function decreases with height up to where the line core forms, causing the overall absorption profile without emission features.

Panels b and c in Fig. 10 show the formation of Ca II H and Mg II k, respectively. The maximum height of the Ca II H optical depth unity curve is just below that of Mg II k. The Ca II H profile has two peaks as a result of the peak in source function. There is an increase in the source function just after it decouples from the Planck function at approximately 0.7 Mm that gives rise to a small intensity increase in the red peak. The

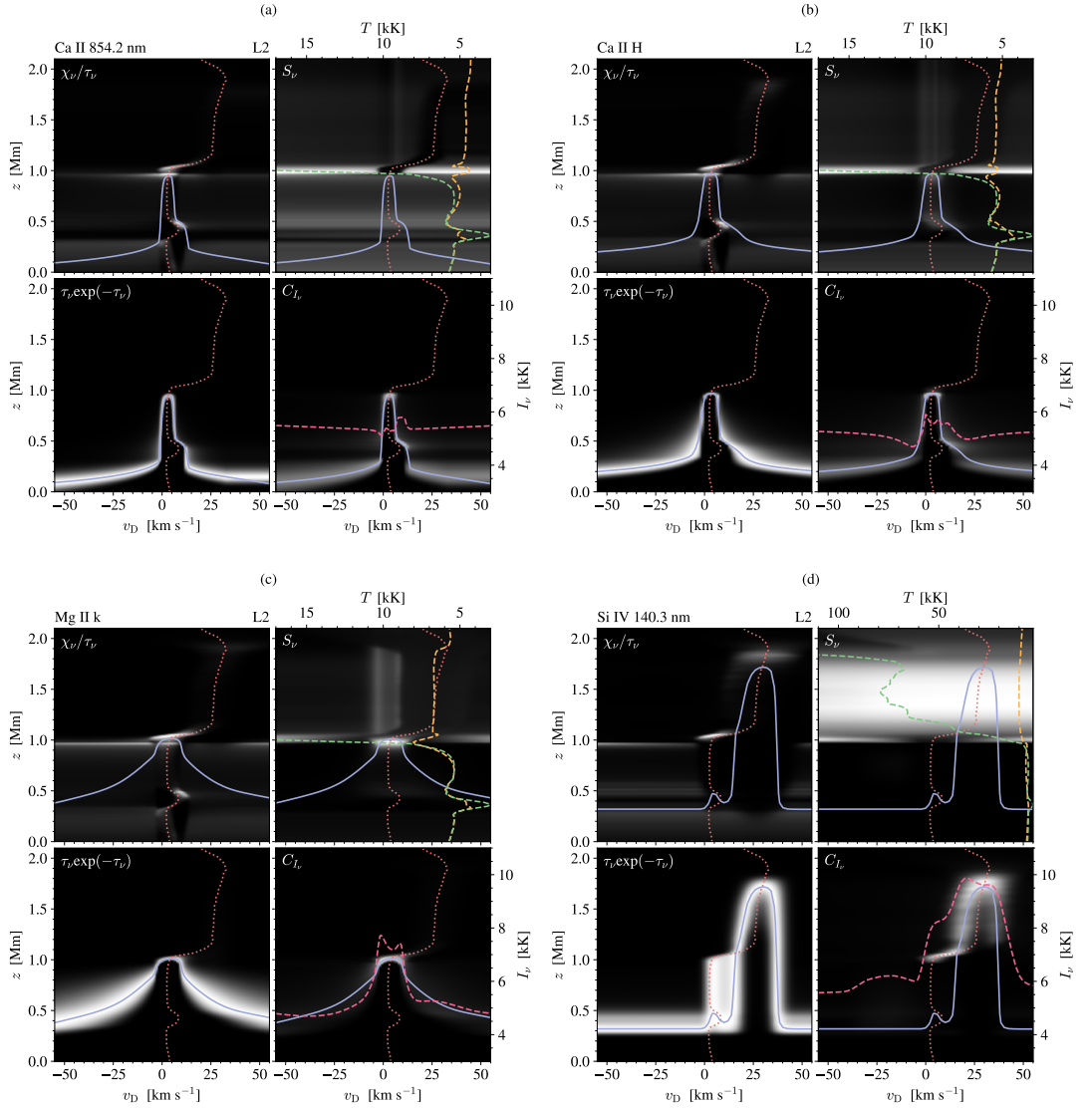


Fig. 9. Intensity formation of the Ca II 854.2 nm (a), Ca II H (b), Mg II k (c), and Si IV 140.3 nm (d) spectral lines at the L2 location at $t' = 28$ s. Each subfigure consists of four panels, where the quantities given in the top left corners are shown in greyscale as functions of frequency from the line centre (in units of Doppler offset) and atmospheric height. The $\tau_\nu = 1$ height (purple solid) and vertical velocity (red dotted) are displayed in all panels. Negative (positive) velocities correspond to upflows (downflows). The top right panels display the source function at $v_D = 0$ (yellow dashed) and Planck function (green dashed) in units of brightness temperature specified along the top (we note that the temperature range in (d) is larger because Si IV is sensitive to much higher temperatures). Multiplication of the first three panels produces the contribution function in the bottom right panel. This panel also contains the intensity profile (pink dashed) in units of brightness temperature. Gamma correction is added to the C_{I_ν} term to amplify the weaker values.

velocity gradient also makes a small contribution to the emission of the red peak, which has a slightly higher intensity than the blue peak. The rest of the line profile forms similarly as Ca II 854.2 nm, where the intensity maps the source function. The red and blue peaks of the Mg II k profile are caused by

the velocity gradient and temperature increase around 1.35 Mm, while the absorption feature is caused by the decline in the source function at the maximum height of the optical depth unity curve. The source function decouples from the Planck function at a higher height (around 1.25 Mm) compared to Ca II H, giving

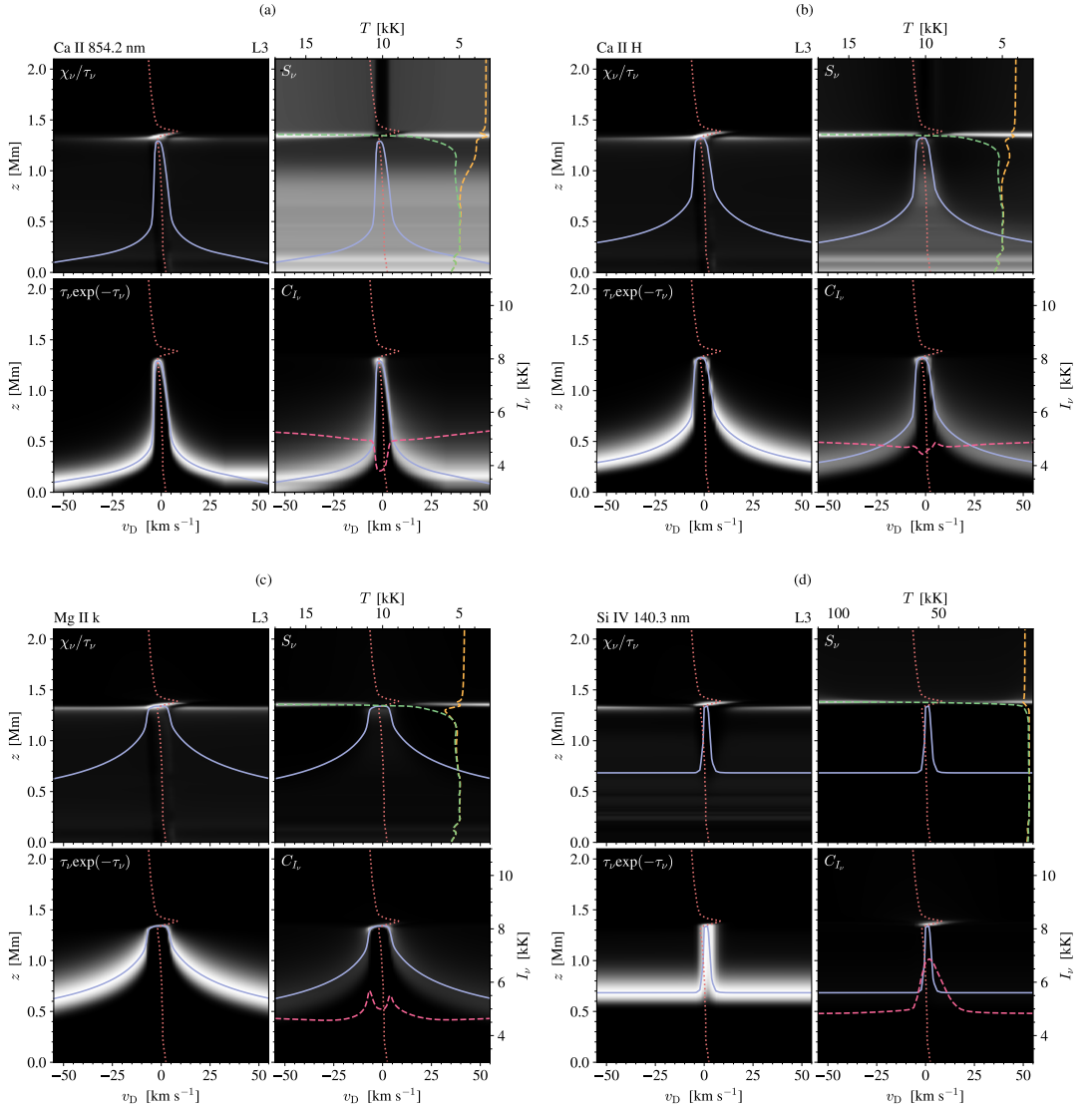


Fig. 10. Intensity formation of the Ca II 854.2 nm (a), Ca II H (b), Mg II k (c), and Si IV 140.3 nm (d) spectral lines at the L3 location at $t' = 28$ s. See the caption of Fig. 9 for more details.

a larger rise in source function that leads to more pronounced peaks.

Figure 10d shows the intensity formation of Si IV 140.3 nm. The contribution function is dominated by the χ_ν/τ_ν term, which is caused by the weak downflowing velocity around $z = 1.35$ Mm. The velocity causes the single peaked profile to shift to the red. We know from Fig. 6 that the lines forming at the L3 location are subject to shock waves passing through the atmosphere, where the oscillations in temperature contributes to increases and decreases in intensity. The 2×2 diagrams only show a single instance in time, and at $t' = 28$ s the maximum for-

mation height of the Si IV line is just below the height of the temperature increase. Hence we can assume that the line is formed between the shock waves.

Figure 11 shows the formation of the different spectral profiles at the L4 location. Panels a represent the intensity formation of Ca II 854.2 nm. The line forms below the height of both the velocity gradient at 1.1 Mm and the temperature increase at 1 Mm. There is a decrease in the source function after it decouples from the Planck function. When the temperature starts to increase around 0.7 Mm, the source function increases too. This, together with the increase in χ_ν/τ_ν at

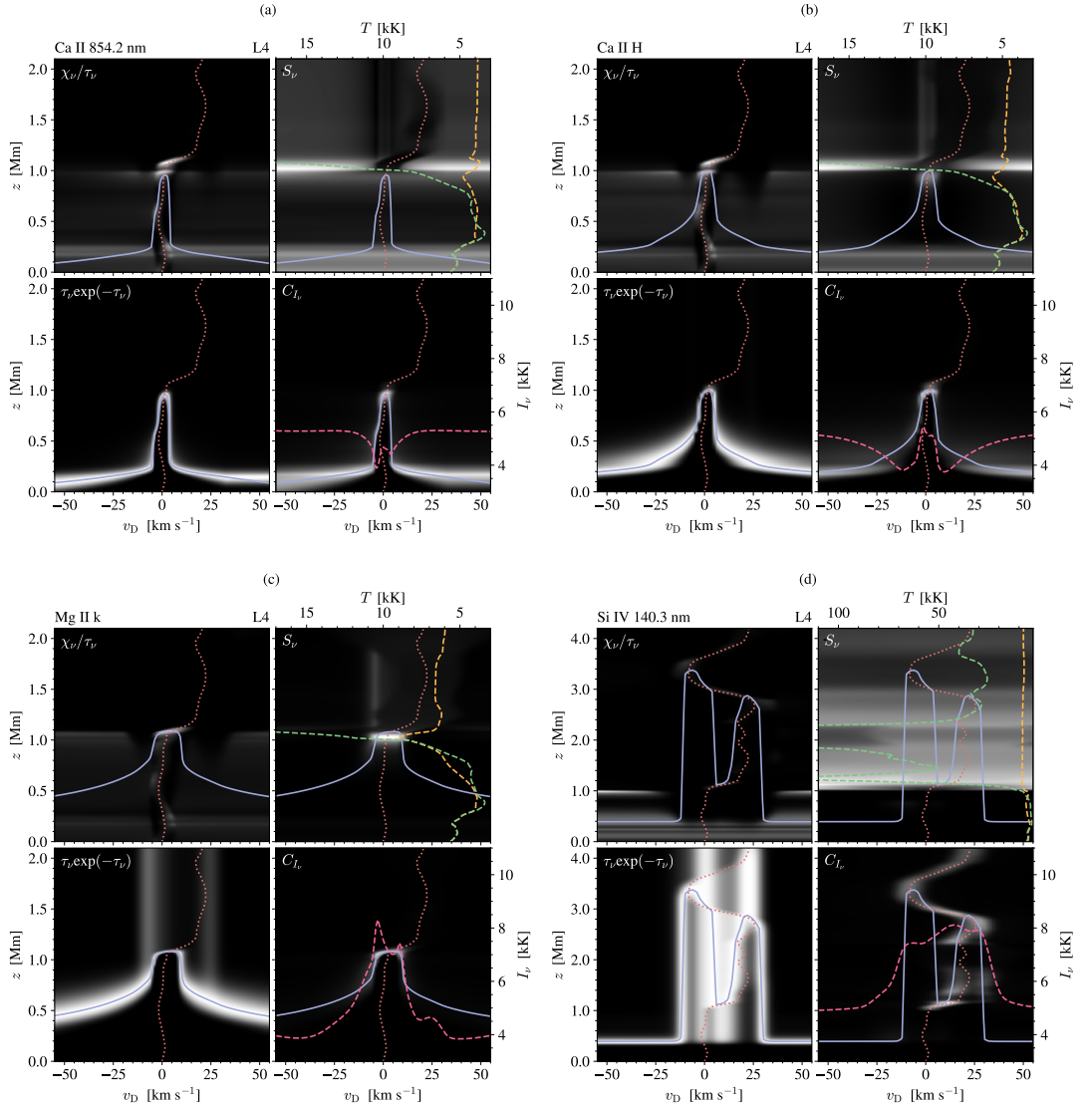


Fig. 11. Intensity formation of the Ca II 854.2 nm (a), Ca II H (b), Mg II k (c), and Si IV 140.3 nm (d) spectral lines at the L4 location at $t' = 28$ s. We note that the maximum height in (d) is larger than the other panels. See the caption of Fig. 9 for more details.

the maximum $\tau = 1$ height, causes an emission feature in the line core.

Panels b and c in Fig. 11 show the intensity formation of Ca II H and Mg II k, respectively. Both lines are double peaked, with a blue peak that has higher intensity than the red peak. The two peaks in the Ca II H profile are caused by the increase in source function around 0.95 Mm. The blue peak is more intense because the χ_ν/τ_ν term gives a stronger contribution on the blue side. The decline in source function at the highest height of the $\tau = 1$ curve causes the absorption feature at approximately $+2$ km s^{-1} . We note that there is a strong velocity gradient around

1.1 Mm that does not contribute to the formation of the Ca II H line intensity. However, the Mg II k line forms at this height, and the strong downward velocity gradient causes the line core to shift to the red. The blue peak is more intense than the red peak because it gets a larger contribution from the $\tau_\nu \exp(-\tau_\nu)$ term, but both peaks get a significant contribution from the increase in temperature and source function at 1.05 Mm. The absorption feature is caused by the decline in source function at 1.1 Mm. The increased emission of the red wing (around $+25$ km s^{-1}) and blue wing (around -10 km s^{-1}) is most likely caused by the bright columns seen in the $\tau_\nu \exp(-\tau_\nu)$ panel,

even though the contribution is too small to be visible in the C_I panel.

Figure 11d shows the formation of the Si IV 140.3 nm line. The complex structure of the atmosphere at L4 (see Fig. 3d) results in the line features forming at very different heights (we note that the height in Fig. 11d ranges from 0 to 4 Mm, whereas the height in the other panels ranges from 0 to 2 Mm). We can distinguish both a blue and a red component in the line profile. These are formed at $z = 3$ and $z = 3.2$ Mm, where the $\tau = 1$ heights have peaks at -10 and $+25$ km s $^{-1}$. These velocity components contribute to the broadening of the spectral profile. The line core forms around 1.05 Mm, where there is a downward velocity component that causes it to shift to the red. The emission of the line core is caused by the sudden increase in temperature and source function.

4. Discussion

The analysis presented in this work shows that the chromospheric and TR spectra are highly affected by strong velocity gradients and sudden variations in temperature. It is difficult to determine if these variations are due to the non-thermal electrons depositing their energy along the magnetic field, especially since the simulation is multi-dimensional and potential effects that occur are not aligned with the particular vertical columns used for calculating the emergent spectra. Even though we cannot make a firm conclusion about the effect the non-thermal electrons have on the synthetic spectra, our results contribute to the continued pursuit of understanding small-scale reconnection events and their impact on the solar atmosphere.

To determine signatures in the synthetic spectra that may arise from the non-thermal electrons, we studied the evolution of the atmosphere and the response to the accelerated electrons. Frogner et al. (2020) have shown that the energy transport by accelerated electrons and thermal conduction differs greatly with depth in the lower atmosphere. Heating by thermal conduction dominates at TR heights, but decreases towards the chromosphere due to the temperature drop. The non-thermal electrons are not directly affected by the sudden decrease in temperature at TR heights, and beam heating generally exceeds conductive heating in the chromosphere. This means that synthetic spectra forming at TR heights, such as the Si IV resonance lines, are likely to be affected by both electron beam heating and thermal conduction, while the synthetic chromospheric spectra should be mostly affected by the non-thermal electrons. However, Fig. 3 shows that there is no clear indication that the electron beams are affecting the evolution of the atmosphere. This is most likely due to the low value of E_C for the non-thermal electrons in the corona, but also because the energy transport is very low. Small values of E_C (around 1–2 keV) implies that the effect of non-thermal electrons on the TR and chromosphere are similar to that of thermal conduction (Testa et al. 2014, 2020; Polito et al. 2018). Additionally, signatures from non-thermal electrons in chromospheric spectra greatly diminishes when the electrons deposit their energy in the corona. In an attempt to add maximum power to the electron beams, we performed an experiment where all the energy from the reconnection events was transferred to the electrons ($p = 1$). In this experiment, the atmospheric structure was almost identical to the original simulation where $p = 0.2$, and the impact on the spectral diagnostics was insignificant. The only notable difference was in the beam heating, which was increased by a factor of 5. This tells us that the beam heating events in this simulation are too weak to significantly affect the low atmosphere, even when the electron

beams carry the maximum amount of energy that is possible in this simulation.

The low level of change in our simulation might be due to the relatively short time that the electrons are present. Robinson et al. (2022) have demonstrated that it takes approximately 800 s (from the magnetic field is ordered) for the field in a Bifrost simulation of the quiet Sun to generate enough magnetic energy to produce heating events of typical nanoflare energies (10^{24} erg). Guerreiro et al. (2017) have shown that most reconnection events in a Bifrost simulation similar to ours have lifetimes of roughly 40 s, with a weighted average of around 50–60 s. During that lifetime, the energy released by the small-scale events typically ranges from 10^{20} – 10^{24} erg, which is the same as what Frogner et al. (2020) have predicted for longer lasting electron beam heating events. Our 36 s of simulation time is of the order of the shortest events presented in similar simulations, as the high computational cost has so far limited the running time. A longer simulation, including more full time-scale heating events would most likely produce more locations in the chromosphere where the effect of the electron beams would leave their imprint. At this point there is no plan to shoulder the computational cost required without also changing the solar environment to a more active region. To say with certainty that a strong signal would show up in this simulation by running it for longer time cannot therefore be guaranteed.

The travel distance from the site of reconnection to the site of the deposited electron energy is affected by the power-law index δ . A low power-law index allows the electrons to penetrate deeper into the atmosphere, while larger values lead to energy being deposited higher in the atmosphere. This is because the rate of deposited energy increases more rapidly for larger values of δ , meaning that the amount of energy deposited in the lower atmosphere is less than for smaller values of δ . Consequently, the spectra forming higher in the atmosphere, such as the Si IV resonance lines, are more likely to be affected by the non-thermal electrons compared to spectra forming at lower heights. Generally, we expect to see a large difference in the intensity and shape of the spectral lines when the time offset between the non-thermal electrons and the thermal conduction front is the greatest. In reality, this happens if a reconnection event occur high in the atmosphere, meaning that a relatively large amount of energy is transferred to the electrons and the electrons travel a great distance. This comes from the fact that travel distance increases linearly with height, while the available energy decreases exponentially with height. In this analysis, we have chosen columns that are situated at the magnetic field footpoints of the simulation. Even though L2, L3, and L4 are connected to field lines showing large changes in average electron beam heating power, we do not know if energetic events in the corona have an effect on the lower atmosphere. The most significant beam heating is seen at L2 (Fig. 3n), where energy from the non-thermal electrons is deposited at TR and chromospheric heights. What is unique about L2 is that the electrons responsible for the peak in beam heating around 1 Mm are not accelerated from local reconnection in the lower atmosphere, as we do not see negative values of Q_b of the same magnitude at approximately the same height. At L3 and L4, the electrons deposit their energy almost immediately after they are accelerated. At L2, there are two acceleration sites (at $z = 2$ and 9 Mm) where energy is transferred to the electrons. However, since the angle between the magnetic field and the vertical direction at these heights differs from the angle at 1 Mm, these events are not related. It is therefore possible that the electrons depositing their energy at this height might be accelerated from reconnection events in the corona.

L2 is the most promising location in terms of signatures from non-thermal electrons. The electron energy deposited at 1 Mm is consistent with the upflows of hot plasma into the TR and corona, and further takes place around the formation height of the Ca II and Mg II lines. However, it is difficult to know if the strong velocity gradient is caused by the electrons depositing their energy at this height, especially since we see velocity gradients that are consistent with the sudden temperature increase from the chromosphere to the TR at all four locations. Additionally, the velocity gradients at L3 and L4 do not seem to be directly affected by the deposited electron energy, which gives reason to believe that this is not the case at L2 either. This is further supported by comparing the spectral lines, where the shape and features of the Mg II k line at L2 and L4 are both caused by steep velocity gradients and sudden increases in temperature. If the electrons have a significant impact on the temperature and velocity at L2, we expect to see a larger difference between the spectral profiles at the two locations. However, we cannot be certain that the electrons do not affect the atmosphere, and hence also the spectra, even though there are no significant effects from the energy deposited directly in the TR and chromosphere. We know that the electrons are continuously accelerated throughout the simulation, and they might be affecting the result more passively compared to larger energy releases. The Ca II H, Mg II k, and Si IV 104.3 nm lines show similarities to those produced by some of the RADYN models in Polito et al. (2018), Testa et al. (2020), and Bakke et al. (2022), in particular the low-temperature (1 MK) loop models. The similarities include increased emission of the Ca II H and Mg II k blue peaks, slight redshift of the Mg II k line core, emission of the blue wing of Mg II k, and single peaked Si IV 104.3 nm profiles that are strongly redshifted. The fact that we see spectral features that are similar to the signatures caused by non-thermal electrons in RADYN models suggests that the accelerated electrons in the Bifrost simulation have an impact on the atmosphere. However, even though we have an idea of the mechanisms behind small-scale heating events and the transport of non-thermal electrons, it is difficult to make a conclusion from our simulation without observational proof.

The results of the spectral line analysis can give an indication of what to look for in observations. The non-thermal electrons present in the Bifrost simulation might have an impact on the atmosphere, even though spectral line features that arise as a consequence to the beam heating have proven difficult to identify. We find that the changes to the synthetic spectra over time are relatively small. If the features of the spectral profiles are caused by the non-thermal electrons, and these features are more or less sustained over the simulation duration, it should mean that small-scale events can be detected by instruments with slower cadence than the 1 s time step in this simulation as the signal remains relatively unchanged. The spectral line diagnostics in this work include the Ca II lines, which gives potential for observing small-scale events with ground-based telescopes, such as the Swedish 1-m Solar Telescope (SST; Schärmer et al. 2003), the *Daniel K. Inoué* Solar Telescope (DKIST; Rimmele et al. 2020), and the planned European Solar Telescope (EST; Quintero Noda et al. 2022). It is beneficial to include lines in the visible, as ground-based telescopes allow for higher spatial resolution compared to millimetre observations and extreme-UV diagnostics observed from space. Coordinated observations with for instance SST and IRIS would be advantageous to provide more constraints on small-scale heating events, even below the nanoflare limit.

In this paper, we have investigated the effect of non-thermal electrons in a 3D Bifrost simulation by performing a detailed

analysis of synthetic chromospheric and TR spectral lines. We have demonstrated that there is a clear difference between the spectra forming in regions subject to electron beams and not. We show that the spectral lines are highly affected by variations in vertical velocity and temperature, but the complexity of the atmospheric response in the Bifrost simulation makes it challenging to determine specific signatures that arise uniquely from the non-thermal electrons. Based on the simulations presented here, we cannot conclude that a clear and consistent signature will arise when higher beam energies are included. Additionally, the time span of the simulation is shorter than the typical lifetimes of small-scale heating events. A simulation with a longer time span and with higher energy beam heating events would be interesting to investigate when available. Still, the spectral line analysis performed in this work can contribute to the understanding of small-scale heating events in the solar atmosphere.

Acknowledgements. We thank Paola Testa for the useful comments that helped improve the paper. This research was supported by the Research Council of Norway, project numbers 250810 and 325491, and through its Centres of Excellence scheme, project number 262622. Computational resources have been provided by Sigma2 – the National Infrastructure for High-Performance Computing and Data Storage in Norway.

References

- Allred, J., Kowalski, A., & Carlsson, M. 2015, *AAS/AGU Triennial Earth-Sun Summit*, 1, 302.07
- Asplund, M., Grevesse, N., Sauval, A. J., & Scott, P. 2009, *ARA&A*, 47, 481
- Bakke, H., Frogner, L., & Gudiksen, B. V. 2018, *A&A*, 620, L5
- Bakke, H., Carlsson, M., Rouppé van der Voort, L., et al. 2022, *A&A*, 659, A186
- Biskamp, D. 2005, *Magnetic Reconnection in Plasmas* (Cambridge: Cambridge University Press)
- Björger, J. P., Sukhorukov, A. V., Leenaarts, J., et al. 2018, *A&A*, 611, A62
- Brown, J. C. 1971, *Sol. Phys.*, 18, 489
- Carlsson, M., & Leenaarts, J. 2012, *A&A*, 539, A39
- Carlsson, M., & Stein, R. F. 1992, *ApJ*, 397, L59
- Carlsson, M., & Stein, R. F. 1995, *ApJ*, 440, L29
- Carlsson, M., & Stein, R. F. 1997, *ApJ*, 481, 500
- Cooper, K., Hannah, I. G., Grefenstette, B. W., et al. 2021, *MNRAS*, 507, 3936
- Del Zanna, G., Dere, K. P., Young, P. R., & Landi, E. 2021, *ApJ*, 909, 38
- De Pontieu, B., Title, A. M., Lemen, J. R., et al. 2014, *Sol. Phys.*, 289, 2733
- Dere, K. P., Landi, E., Mason, H. E., Monsignor Fossi, B. C., & Young, P. R. 1997, *A&AS*, 125, 149
- Emslie, A. G. 1978, *ApJ*, 224, 241
- Emslie, A. G., Kucharek, H., Dennis, B. R., et al. 2004, *J. Geophys. Res. Space Phys.*, 109, A10104
- Emslie, A. G., Dennis, B. R., Shih, A. Y., et al. 2012, *ApJ*, 759, 71
- Feldman, U. 1992, *Phys. Scr.*, 46, 202
- Frogner, L., & Gudiksen, B. V. 2022, arXiv e-prints [arXiv:2210.01609]
- Frogner, L., Gudiksen, B. V., & Bakke, H. 2020, *A&A*, 643, A27
- Glesener, L., Krucker, S., Duncan, J., et al. 2020, *ApJ*, 891, L34
- Gudiksen, B. V., Carlsson, M., Hansteen, V. H., et al. 2011, *A&A*, 531, A154
- Guerreiro, N., Haberleiter, M., Hansteen, V., & Schmutz, W. 2017, *A&A*, 603, A103
- Hannah, I. G., Hudson, H. S., Battaglia, M., et al. 2011, *Space Sci. Rev.*, 159, 263
- Hansteen, V., Ortiz, A., Archontis, V., et al. 2019, *A&A*, 626, A33
- Hawley, S. L., & Fisher, G. H. 1994, *ApJ*, 426, 387
- Hayek, W., Asplund, M., Carlsson, M., et al. 2010, *A&A*, 517, A49
- Holman, G. D., Aschwanden, M. J., Aurass, H., et al. 2011, *Space Sci. Rev.*, 159, 107
- Kanella, C., & Gudiksen, B. V. 2017, *A&A*, 603, A83
- Kerr, G. S., Carlsson, M., Allred, J. C., Young, P. R., & Daw, A. N. 2019, *ApJ*, 871, 23
- Laming, J. M. 2004, *ApJ*, 614, 1063
- Leenaarts, J., Pereira, T. M. D., Carlsson, M., Uitenbroek, H., & De Pontieu, B. 2013a, *ApJ*, 772, 89
- Leenaarts, J., Pereira, T. M. D., Carlsson, M., Uitenbroek, H., & De Pontieu, B. 2013b, *ApJ*, 772, 90
- Lin, R. P., & Hudson, H. S. 1971, *Sol. Phys.*, 17, 412
- Martínez-Sykora, J., De Pontieu, B., Hansteen, V. H., & Gudiksen, B. 2016, *ApJ*, 817, 46

- Milkey, R. W., & Mihalas, D. 1974, *ApJ*, 192, 769
- Olluri, K., Gudiksen, B. V., Hansteen, V. H., & De Pontieu, B. 2015, *ApJ*, 802, 5
- Parker, E. N. 1988, *ApJ*, 330, 474
- Pereira, T. M. D., & Uitenbroek, H. 2015, *A&A*, 574, A3
- Polito, V., Testa, P., Allred, J., et al. 2018, *ApJ*, 856, 178
- Quintero Noda, C., Schlichenmaier, R., Bellot Rubio, L. R., et al. 2022, *A&A*, 666, A21
- Rimmele, T. R., Warner, M., Keil, S. L., et al. 2020, *Sol. Phys.*, 295, 172
- Robinson, R. A., Carlsson, M., & Aulanier, G. 2022, *A&A*, 668, A177
- Scharmer, G. B., Bjelksjo, K., Korhonen, T. K., Lindberg, B., & Petterson, B. 2003, *SPIE Conf. Ser.*, 4853, 341
- Shine, R. A., Milkey, R. W., & Mihalas, D. 1975, *ApJ*, 199, 724
- Skan, M., Danilovic, S., Leenaarts, J., Calvo, F., & Rempel, M. 2023, *A&A*, 672, A47
- Testa, P., De Pontieu, B., Martínez-Sykora, J., et al. 2013, *ApJ*, 770, L1
- Testa, P., De Pontieu, B., Allred, J., et al. 2014, *Science*, 346, 1255724
- Testa, P., Polito, V., & De Pontieu, B. 2020, *ApJ*, 889, 124
- Uitenbroek, H. 2001, *ApJ*, 557, 389
- Vardavas, I. M., & Cram, L. E. 1974, *Sol. Phys.*, 38, 367
- Visser, G. 2012, & Rouppe van der Voort, L., *ApJ*, 750, 22
- Warren, H. P., Brooks, D. H., Doschek, G. A., & Feldman, U. 2016, *ApJ*, 824, 56
- Wright, P. J., Hannah, I. G., Grefenstette, B. W., et al. 2017, *ApJ*, 844, 132

Paper III

High Resolution Observations of the Low Atmospheric Response to Small Coronal Heating Events in Active Regions

**Paola Testa, Helle Bakke, Luc Rouppe van der Voort, Bart De
Pontieu**

Forthcoming article in *The Astrophysical Journal*



High Resolution Observations of the Low Atmospheric Response to Small Coronal Heating Events in an Active Region Core

PAOLA TESTA,¹ HELLE BAKKE,^{2,3} LUC ROUPPE VAN DER VOORT,^{2,3} AND BART DE PONTIEU^{4,2,3}

¹*Harvard-Smithsonian Center for Astrophysics, 60 Garden St, Cambridge, MA 02193, USA*

²*Roseland Centre for Solar Physics, University of Oslo, P.O. Box 1029 Blindern, N-0315 Oslo, Norway*

³*Institute of Theoretical Astrophysics, University of Oslo, P.O. Box 1029 Blindern, N-0315 Oslo, Norway*

⁴*Lockheed Martin Solar & Astrophysics Laboratory, 3251 Hanover St, Palo Alto, CA 94304, USA*

(Received)

Submitted to ApJ

ABSTRACT

High resolution spectral observations of the lower solar atmosphere (chromosphere and transition region) during coronal heating events, in combination with predictions from models of impulsively heated loops, provide powerful diagnostics of the properties of the heating in active region cores. Here we analyze the first coordinated observations of such events with the *Interface Region Imaging Spectrograph* (*IRIS*) and the *CHROMospheric Imaging Spectrometer* (*CHROMIS*), at the Swedish 1-m Solar Telescope (*SST*), which provided extremely high spatial resolution and revealed chromospheric brightenings with spatial dimensions down to ~ 150 km. We use machine learning methods (*k*-means clustering) and find significant coherence in the spatial and temporal properties of the chromospheric spectra, suggesting, in turn, coherence in the spatial and temporal distribution of the coronal heating. The comparison of *IRIS* and *CHROMIS* spectra with simulations suggest that both non-thermal electrons with low energy (low-energy cutoff ~ 5 keV) and direct heating in the corona transported by thermal conduction contribute to the heating of the low atmosphere. This is consistent with growing evidence that non-thermal electrons are not uncommon in small heating events (nano- to micro-flares), and that their properties can be constrained by chromospheric and transition region spectral observations.

Keywords: Solar physics — Active Sun — Solar atmosphere — Solar chromosphere — Solar transition region — Solar ultraviolet emission – Solar extreme ultraviolet emission — Solar coronal heating

1. INTRODUCTION

The understanding of the physical processes converting magnetic energy into thermal energy and powering the solar outer atmosphere represents one of the main open issues in solar physics (e.g., Klimchuk 2006; Reale 2014; Testa & Reale 2022). The heating is generally predicted to be impulsive (e.g., Klimchuk 2015), and on small spatial scales (below the current resolution capabilities). Direct observational diagnostics of coronal heating are therefore often difficult to obtain.

Tracers of coronal heating can sometimes be more evident in observations of the lower solar atmosphere – transition region (TR) and chromosphere – which efficiently radiates energy excesses, rather than in the highly conductive corona, where the signatures of heating release are easily washed out. Furthermore, while the coronal emission in a pixel is due to contributions from a generally complex three dimensional system of loops, the TR is relatively unencumbered by contamination of other material along the line of sight. It is therefore easier to detect and study single heating events in the TR, and derive constraints on the coronal event properties. For these reasons, the moss (the bright TR of high pressure loops; e.g., Peres et al. 1994; Fletcher & De Pontieu 1999; Berger et al. 1999) is well suited to

Corresponding author: Paola Testa
ptesta@cfa.harvard.edu

investigate the properties of coronal heating in the core of ARs (e.g., Martens et al. 2000; Antiochos et al. 2003; Testa et al. 2013, 2014, 2020).

The temporal variability of the moss has been studied in imaging and spectral observations, and its relatively constant emission has often been attributed to steady heating of AR cores (e.g., Antiochos et al. 2003; Brooks et al. 2009; Tripathi et al. 2010). However, high spatial ($\sim 0.3''$) and temporal resolution EUV imaging data with the High-resolution Coronal Imager (Hi-C; Kobayashi et al. 2014) sounding rocket, have provided evidence of TR brightenings on short timescales (down to ~ 15 s) at the footpoints of transient hot loops (Testa et al. 2013). Follow-up TR spectral observations at high spatial, temporal, and spectral resolution with the Interface Region Imaging Spectrograph (*IRIS*, De Pontieu et al. 2014), together with 1D hydrodynamic RADYN models of nanoflare heated loops – including non-local thermodynamic equilibrium (non-LTE), and heating by beams of non-thermal electrons (NTE) as well as in-situ thermal heating –, provided powerful diagnostics of the properties of coronal heating and mechanisms of energy transport (Testa et al. 2014, 2020; Cho et al. 2023). Polito et al. (2018) and Testa et al. (2020) discussed the *IRIS* diagnostics of the coronal heating properties from spectral observations of moss brightenings. Bakke et al. (2022) recently extended those investigations to ground-based observations, deriving additional diagnostics of the heating properties from lower chromospheric emission.

In this paper we analyzed coordinated chromospheric AR observations, with the Swedish 1-m Solar Telescope (*SST*; Scharmer et al. 2003a,b), and with *IRIS*, as well as coronal observations with *SDO*/AIA, for a small heating event in an AR. The very high resolution chromospheric observations spectra from *SST* provide new constraints to the models of small heating events. A k -means analysis of these *SST* spectra allows us to detect coherence in the spatial and temporal distribution of the chromospheric emission, and, in turn, to speculate on the coherence of the spatial and temporal distribution of the heating properties. *IRIS* spectral observations provide insights into the chromospheric and TR properties. In Section 2 we describe the selected data, and their analysis and comparison with expectations from numerical simulations is presented in Section 3. In Section 4 we summarize and discuss our findings, and draw our conclusions.

2. OBSERVATIONS AND DATA ANALYSIS

The detection of small (nano- to microflare) coronal heating events in coordinated *IRIS* and *SST* observa-

tions of active regions is one of the goals of the multi-year campaign we have conducted since the *IRIS* launch in 2013 (Roupe van der Voort et al. 2020). In fact, *SST* and *IRIS* provide very useful complementary high-resolution observations of the photosphere and chromosphere that can greatly enhance the scientific impact of either separate instrument.

Here we focus on one of the first such events observed during the *SST* and *IRIS* coordinated campaign. In particular, we selected the observations of AR 12585 carried out on 2016-09-04 (Figure 1 and Figure 2 show images of this event observed by *SST*, *IRIS*, and *SDO*). This dataset is part of the database of publicly available *SST* and *IRIS* coaligned datasets described in Roupe van der Voort et al. (2020), and some analysis of it has been presented by Roupe van der Voort et al. (2017).

The *SST* telescope includes dual Fabry-Pérot filtergraph systems capable of fast wavelength sampling of spectral lines: the CRISP Imaging SpectroPolarimeter (CRISP; Scharmer et al. 2008), and the CHROMospheric Imaging Spectrometer (CHROMIS; Scharmer 2017), with field of view of approximately $1' \times 1'$. CRISP has a plate scale of $0''.058$ per pixel and the *SST* diffraction limit is $0''.14$ at the wavelength of the H α line (calculated as λ/D with $\lambda = 6563\text{\AA}$ and $D = 0.97$ m the diameter of the *SST* aperture). The CHROMIS instrument (installed in 2016) has a plate scale of $0''.038$ per pixel and the diffraction limit is $0''.08$ at the wavelength of the Ca II K line ($\sim 3933.7\text{\AA}$). The data we analyze here were acquired during the first CHROMIS campaign (Roupe van der Voort et al. 2017; Vissers et al. 2019). Here we mainly focus on the analysis of the chromospheric Ca II K data. The Ca II K line was sampled at 21 wavelength positions, between ± 100 km s $^{-1}$ Doppler offset from line center. The line was sampled with 6 km s $^{-1}$ steps (or 78 m \AA) between ± 54 km s $^{-1}$ and somewhat coarser in the rest of the wavelength range. In addition, a continuum position was sampled at 4000 \AA . The CRISP instrument was running a program sampling the H α line at 15 line positions between ± 68 km s $^{-1}$, and Ca II 8542 \AA at 21 line positions between ± 61 km s $^{-1}$. The data was processed following the CRISPRED reduction pipeline (de la Cruz Rodríguez et al. 2015) and an early version of the CHROMISRED pipeline (now both are incorporated into SSTRED, Löfdahl et al. 2021). Seeing-induced deformations were corrected for using Multi-Object Multi-Frame Blind Deconvolution (MOMFBD; van Noort et al. 2005) image restoration. The CHROMIS timeseries has a cadence of ~ 22 s, the CRISP timeseries has a cadence of 20 s. The wavelength calibration of the *SST*/CHROMIS observations has been performed by using an average profile over a quiet area

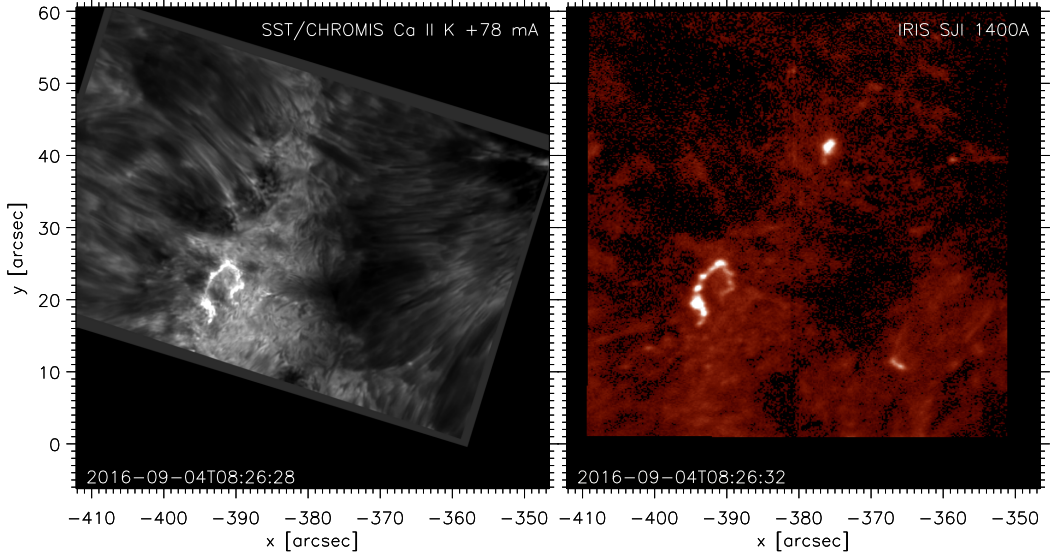


Figure 1. Chromospheric and TR observations in AR 12585 with *SST/CHROMIS* and *IRIS* on 2016-09-04 around 08:26UT. *Left:* *SST/CHROMIS* image at the center wavelength of Ca II (at 3934Å); *Right:* *IRIS* slit-jaw image (SJI) in the 1400Å band. The bright S-shaped region corresponds to brightenings at the footpoints of hot loops undergoing short-lived heating, as illustrated in the context coronal images presented in Figure 2.

just prior to the observations, and deriving the wavelength within the Ca II line where the intensity is at a minimum value. This reference wavelength is given the value (3933.6841Å) of the wavelength of the Ca II K line minimum in the FTS atlas (Neckel 1999).

We note that particularly the CHROMIS observations have exceptionally high spatial resolution (~ 100 km), which can constrain significantly better the spatial distribution of the heating events.

IRIS observes chromospheric and TR emission in UV at high spatial and temporal resolution with both high-resolution spectroscopy and slit-jaw imaging (SJI). The *IRIS* observations we analyze here are medium dense 16-step rasters (OBSID 3625503135), with exposure time of 0.5 s, and raster steps of $0''.35$, covering a field-of-view of about $5'' \times 60''$ (in about 21 s). Slit-jaw images were recorded in the SJI 1400 Å (dominated by Si IV lines), 1330 Å (dominated by C II lines), and 2796 Å (Mg II k core) channels at a temporal cadence of about 10 s. We use *IRIS* calibrated level 2 data, which have been processed for dark current, flat field, and geometrical corrections (De Pontieu et al. 2014). The *SST* and *IRIS* observations were aligned through cross-correlation of image pairs in the Ca II K wing and SJI 2796Å (see Rouppe van der Voort et al. 2020, for more details). The alignment between Ca II K and SJI 2796Å appears

to be accurate down to the *IRIS* SJI pixel size ($0''.166$). The short exposure time of the *IRIS* program (0.5 s) resulted in a high noise level in the SJI images, in particular in SJI 1400Å and SJI 1330Å. The fiducial marks that are added to the *IRIS* spectrograph slit are difficult to identify in individual SJI images and even impossible to identify in SJI 1400Å. This makes the alignment between the SJI channels challenging as the fiducial marks are the basis for accurate cross alignment. To improve on the SJI alignment as part of the standard *IRIS* level 2 data processing, we summed over many SJI exposures to reduce the noise level and improve the visibility of the fiducial marks. It is clear that this procedure improved the alignment but it cannot be excluded that there remains a residual misalignment on the order of one or two pixels between SJI 2796Å and SJI 1400Å.

We also use coordinated imaging observations of coronal emission, taken with the Atmospheric Imaging Assembly (AIA; Lemen et al. 2012) onboard the Solar Dynamics Observatory (*SDO*; Pesnell et al. 2012). The AIA datasets are characterized by $0''.6$ pixels, and 12 s cadence, and observe the TR and corona across a broad temperature range (Boerner et al. 2012, 2014). We used the AIA datacubes coordinated with and coaligned to the *IRIS* datasets, which are distributed from the *IRIS*

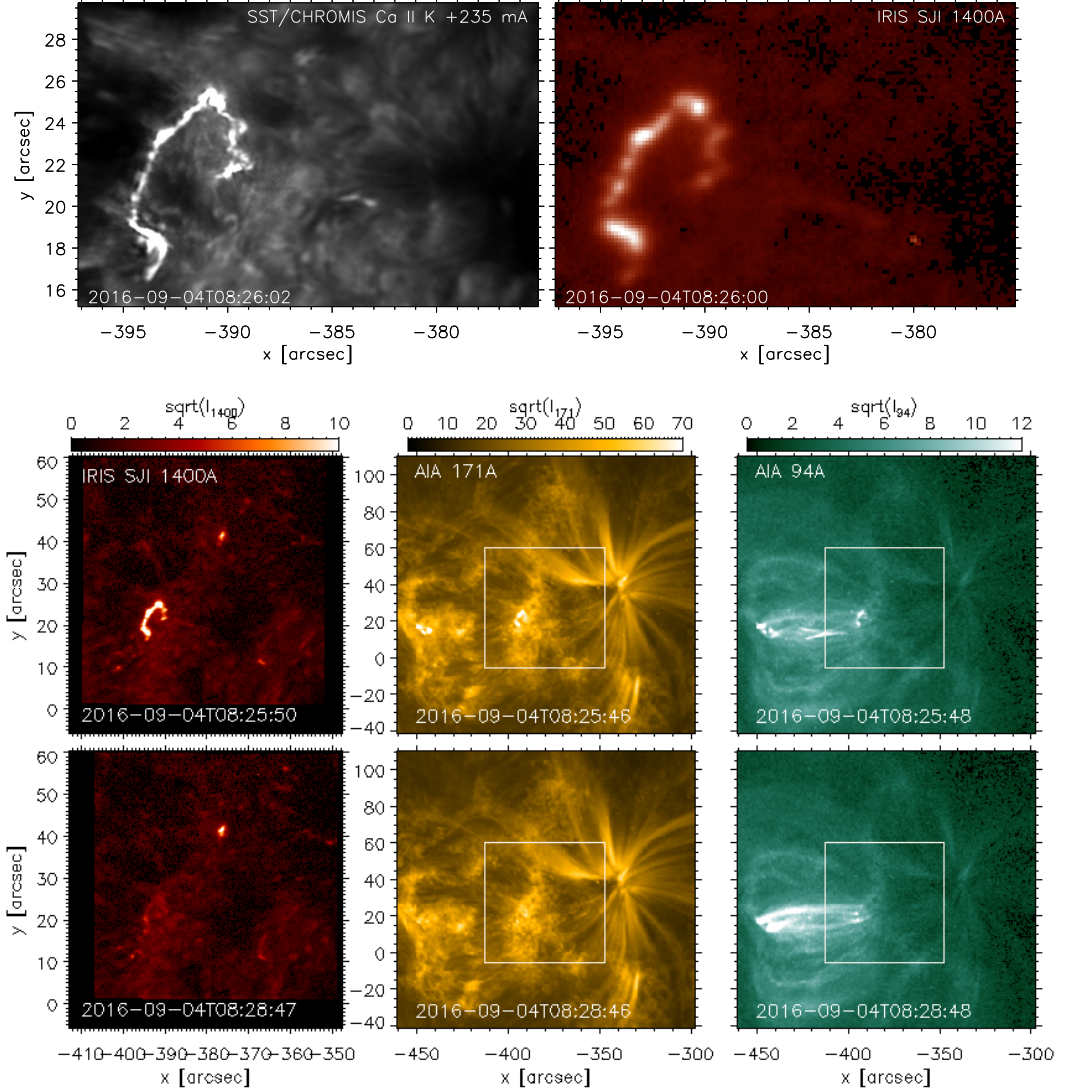


Figure 2. *SST*, *IRIS*, and *SDO* coordinated observations of AR 12585. In the top panels we plot zoomed in versions of the images of Figure 1 showing emission in the Ca II K core (*left*) and *IRIS* 1400Å SJI (*right*). The bottom panels show the TR and coronal emission, for two times – one at the peak of the loop footpoint chromospheric emission (*top*), and one 3 min later (*bottom*) when the overlying hot coronal loops are bright. In particular we show, from left to right: the TR emission in the *IRIS* SJI 1400Å passband; the upper TR emission in the AIA 171Å narrowband, dominated by ~ 1 MK emission from Fe IX; the coronal emission in the AIA 94Å narrowband (which has a cooler, ~ 1 MK, component, and a hot $\gtrsim 4$ MK component). For the AIA emission we show a larger f.o.v. than the corresponding *IRIS* observations. We mark with white boxes the f.o.v. of the *IRIS* SJI.

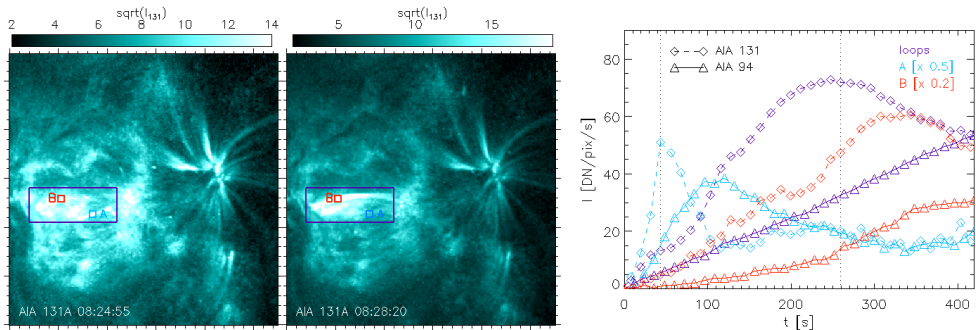


Figure 3. Evolution of the hot coronal emission in the AR core during the heating event. The left two panels show the coronal emission in the *SDO/AIA* 131Å passband (the 131Å emission in the transient core loops is dominated by hot Fe XXI emission), and for the same f.o.v. of the other AIA passbands shown in Figure 2, at two times (close to the beginning of the heating event and a few minutes later). Three locations are marked in these images to identify interesting coronal features: a short hot loop brightening early in the event (*A*), a location in a longer loop at the footpoints of which the chromospheric and TR brightenings are observed as shown in Figures 1 and 2 (*B*), and a larger region (purple rectangle) including most of the dynamic hot loops anchored in the ribbon shown in the previous two figures. The right panel shows lightcurves for $t = 0$ corresponds to 2016-09-04T08:24:00) in the hot AIA passbands at 131Å (diamonds), and 94Å (triangles), for the three regions marked in the left panels. For the *A* and *B* locations the intensities are averaged over 5×5 pixel regions (i.e., $\sim 3'' \times 3''$). All lightcurves are subtracted of their minimum value in the considered temporal window

. The vertical dotted lines mark the times of the two images shown in the left panels.

search data page¹. These AIA time series appear to be affected by unusual and significant (i.e., several AIA pixels) instabilities in the spatial pointing. We therefore refined the coalignment, by using a cross-correlation routine (`tr_get_disp`). We use AIA coronal data to investigate the spatial and temporal properties of the coronal emission.

3. RESULTS

AR 12585 appeared at the East limb around August 30 2016, and it was characterized by sustained coronal activity around GOES (Geostationary Operational Environmental Satellites²) B level. An inspection of the timeseries of the hot emission in the *SDO/AIA* channels (especially the 94Å and the 131Å channels, which include emission from Fe XVIII and Fe XXI lines respectively) shows hot ($\gtrsim 5$ MK) dynamic loops in the AR core, although the X-ray emission in the GOES X-ray passbands did not exceed C level for most of the disk passage (from September 1st onward).

The observations we analyze here captured one of these heating events associated with hot coronal emission. In Figure 2 we show the chromospheric, TR, and coronal emission in the AR at two times of this event:

early on, when the energy is most likely impulsively released and the chromospheric and TR emission at the loops' footpoints is bright, and a few minutes later, when the coronal plasma in the overlying loops is sufficiently hot and dense to emit brightly in the AIA 94Å passband.

In the initial impulsive phase of the heating, the chromosphere and TR present rapid and intense brightenings at the footpoints of the heated loops, similar to flare ribbons, as observed by *SST* and *IRIS* and shown in Figure 1 and Figure 2 where almost simultaneous images of the chromospheric and TR emission are presented.

3.1. Coronal Properties and Evolution

The heating event appears to involve many coronal structures, including the longer (~ 40 Mm in length) coronal structures overlying the bright ribbons we focus on, as well as shorter (~ 20 Mm in length) loops overlying a ribbon brightening about a minute earlier (see center row of Figure 2, and Figure 3). In Figure 3 we show lightcurves for the hot emission observed by AIA in the 94Å and 131Å channels. The lightcurves are obtained by subtracting the background value in the same spatial location just before the event, to highlight the evolution of the hot emission. The observed hot emission shows the typical behavior observed in other microflares (see e.g., Testa & Reale 2020), with a rapid increase in the Fe XXI emission (131Å) in the early phases of the event followed by a cooling phase in which the 131Å

¹ <https://iris.lmsal.com/search/>

² <https://www.swpc.noaa.gov/products/goes-x-ray-flux>,
<https://www.ngdc.noaa.gov/stp/satellite/goes/index.html>

emission decreases while the cooler Fe XVIII 94Å emission increases. An approximate temperature diagnostic from the 131Å/94Å ratio (see e.g., Testa & Reale 2020) suggests peak coronal temperatures around 8–10 MK, analogous to what typically found in similar transient events in AR cores (e.g., Reale et al. 2019a; Testa et al. 2020; Testa & Reale 2020).

3.2. Morphology of the Ribbon

The comparison of the two *SST* and *IRIS* emission maps shown in Figures 1 and 2 clearly illustrates the differences in morphology in different atmospheric layers, as well as (particularly in Figure 2) the extremely high spatial resolution attained in this *SST* dataset by the CHROMIS instrument. Figure 4 shows measurements of the cross-section widths of the ribbon brightenings. There are small spatial offsets of about 0''.2 between corresponding brightenings in Ca II K and SJI 1400Å. Given differences in formation heights and the geometry of the observed coronal loops, spatial offsets could be expected and they might provide valuable information on the 3D morphology of the loop system. We can expect a small offset between the different diagnostics due to differences in formation height, but we are cautious about drawing firm conclusions since we cannot exclude that the offset might be due to a large extent to errors in the alignment between the different passbands. Furthermore, the ribbons evolve very fast and the *SST* and *IRIS* diagnostics are not recorded strictly simultaneously so some of the apparent offsets could be attributed to temporal evolution.

We measured the cross-section widths as full-width-half-maxima for which the half maxima were determined from the difference between the peak intensity and the highest intensity of the two neighboring minima. For these six representative examples, the widths in Ca II K vary between 0''.22 and 0''.36. The widths in SJI 1400Å are more than two times larger and vary between 0''.51 and 0''.84. We note that the narrowest width of 0''.51 corresponds to three *IRIS* pixels. In feature D, the cross-section profile of the Ca II K image has two narrow peaks while the corresponding feature in SJI 1400Å is much wider and fuzzier and does not show sub-structure. The profiles A–F are shown for red wing Ca II K at +235 mÅ (+18 km s⁻¹) which is the Doppler offset of the peak for most of the redshifted ribbon profiles. The widths of cross-section profiles from Ca II K images summed over the full observed spectral widths are only slightly wider. We note how, closer to the two ends of the ribbon (i.e., S of $y \sim 45$, or W of $x \sim -390$, such as e.g., location C at the N-W end), the relative intensity of the CHROMIS Ca II emission with respect to the *IRIS* SJI

1400Å emission is much larger than for most other locations, whereas in other locations such as e.g., E, the TR emission is significantly enhanced with respect to the lower chromospheric emission. As we will discuss more later (see Section 4), these ratios provide clues to the heating properties and transport mechanisms (e.g., harder non-thermal electrons will likely cause stronger enhancements in the deeper atmosphere, i.e., lower chromosphere, than in the TR).

3.3. *k*-means Analysis of *SST* Chromospheric Spectra

To investigate the spatial and temporal evolution of the spectral properties of the chromospheric brightenings we applied *k*-means clustering analysis (e.g., Panos et al. 2018; Bose et al. 2019) to the *SST*/CHROMIS Ca II K spectral data. The *k*-means clustering algorithm finds spectral profiles representative of the observed spectra, and it groups the observed spectra according to their spectral properties. The grouping of the large number of observed spectra in a limited number of clusters, each characterized by a representative spectral profile (RSP), allows us to model more easily the variety of observed profiles, and, in turn, to efficiently derive the spatial distribution and temporal evolution of the coronal heating properties. We used the *k*-means clustering algorithm (Everitt 1972), which partitions data into *k* pre-defined clusters that each have a cluster center which is the average of the data points within that cluster. The clusters are then improved through an iterative process where data points are assigned to a cluster such that the Euclidean distance between the points and the cluster center is minimal. For every iteration, new cluster centers are calculated from the clusters in the previous iteration until the cluster centers do not change and convergence is reached. A limitation to this method is that the resulting clusters depend significantly on the initial selection of cluster centers. An option is to select the cluster centers at random, but then the initial cluster centers can be close to each other and more iterations are needed in order to reach convergence. We used the *k*-means++ initialization method (Arthur & Vassilvitskii 2007), which, before defining new cluster centers, draws the cluster centers randomly from the dataset such that they are as far away as possible from the previous centers.

In order to determine the optimal number of clusters, we used the elbow technique (see e.g., Panos et al. 2018 for a discussion), and we found that 60 clusters are sufficient to characterize the selected subset of *SST*/CHROMIS spectral observations. The 60 representative spectral profiles (RSP) we obtained from this *k*-means analysis are plotted in Figure 5. In Figure 6 we show the spatial distribution of the RSPs in the re-

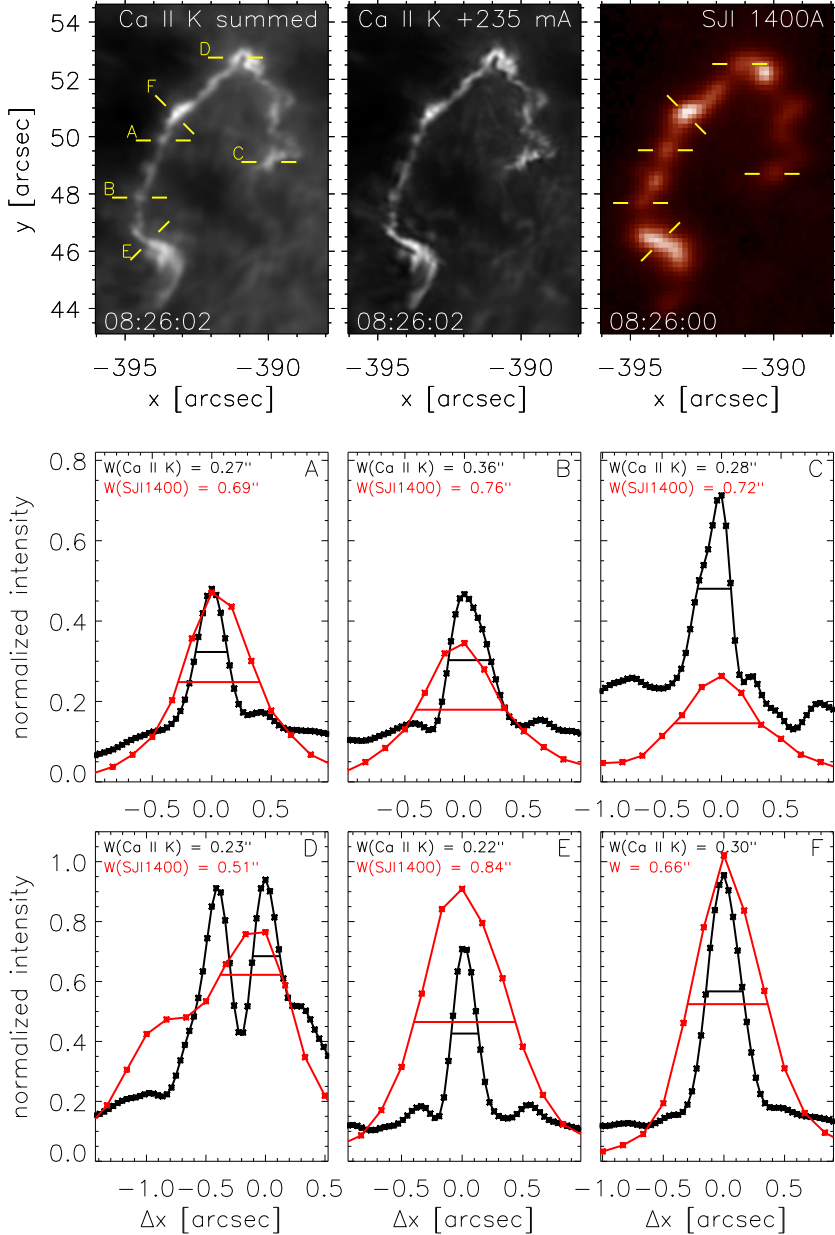


Figure 4. Cross-section widths of brightenings in the flare ribbon from CHROMIS and *IRIS* observations. The top left panel shows an image integrated over the full observed width of the Ca II K line ($\pm 100 \text{ km s}^{-1}$), the top middle panel shows a Ca II K red wing image at around the peak of most redshifted flare profiles. The top right panel shows the corresponding *IRIS* SJI 1400Å image. All images are scaled linearly between their respective minima and maxima. The yellow lines mark the endpoints of the the paths A–F along which intensity profiles were extracted and are shown in the bottom panels. In the bottom panels, the black line is the intensity profile measured in Ca II K +0.235Å, the red line in SJI 1400Å. The full-width-half-maxima are marked with horizontal lines and their values are given in each panel.

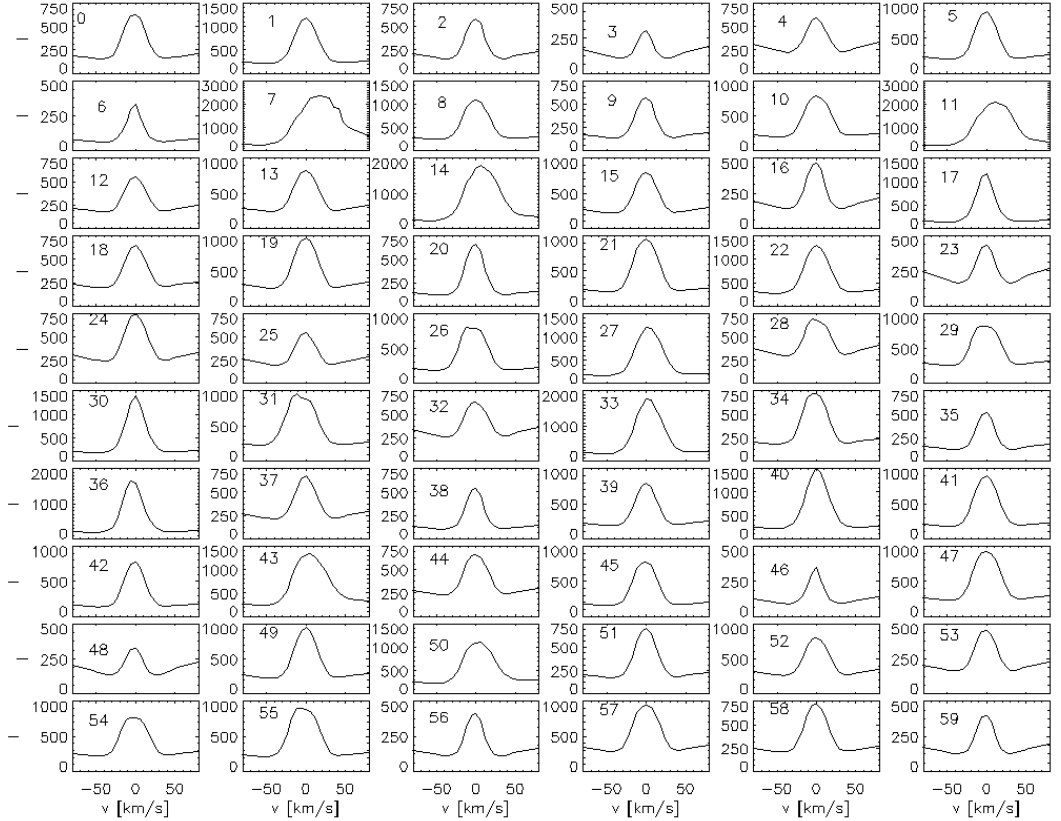


Figure 5. Representative Spectral Profiles (RSP) obtained from k -means analysis, using 60 clusters (see text for a discussion), of the timeseries of *SST*/CHROMIS Ca II K spectra.

gion of the ribbon, and the corresponding RSPs, which show that the Ca II K line observed in the ribbon varies from blueshifted, and generally narrower, profiles to redshifted, and typically broader, profiles. While the observed blueshifts are generally mild ($\lesssim 10 \text{ km s}^{-1}$), some redshifts reach large values (up to $\sim 25 \text{ km s}^{-1}$). The largest blueshifts are mostly observed in the southern portion of the ribbon. The spatial distribution of the RSPs shows a spatial coherence of the observed spectral profiles, with spatial clusters of several sizes from a few pixels ($\gtrsim 0''.1$) to ~ 50 pixels ($\sim 2''$), in one spatial dimension.

We investigated how the spatial distribution of the Ca II K spectral profiles is evolving during the event, as shown in Figure 7, where we plot the maps of RSP distribution for six consecutive timesteps of the CHROMIS observations covering most of the ribbon

evolution. These plots show that the spatial coherence of the spectral profiles is observed for all timesteps, and they reveal several additional interesting features. The highest Doppler shifts are not present in the initial Ca II K profiles (time step 17), but they appear in the second timestep when higher intensities are observed in the ribbon. In fact, the highest Ca II K intensity regions are generally characterized by large and broad redshifted profiles (RSP 7 and 14, red and orange respectively). Blueshifted profiles are observed only in lower intensity regions of the ribbon, and only in the southern portion of the ribbon. In this southern region of the ribbon (around coordinates [160, 170] in time step 18; see Figure 6) there is a patch of broad blueshifted profiles (RSP 31 of Figures 5 and 6), where the spectra rapidly shift to broad redshifted profiles in the next time step (19) when the Ca II K intensities in that region

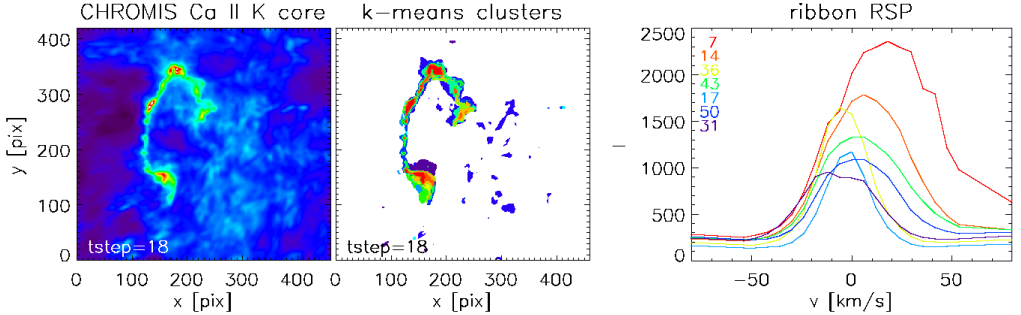


Figure 6. Example of machine learning analysis of *SST*/CHROMIS chromospheric spectral observations of variability at the footpoints of hot loops. We show results of *k*-means clustering analysis applied to a subset of the *SST*/CHROMIS Ca II K spectral data. We selected the f.o.v. shown here and 14 timesteps covering the heating event shown in Figure 1, and a few timesteps prior to it. The *k*-means clustering algorithm finds spectral profiles representative of the observed spectra, and it groups the observed spectra according to their spectral properties (in this example we find 60 clusters are sufficient to group the observed spectra). Here we show, for one time step during the brightenings (the intensity in the Ca II K line core is shown in the left panel), the spatial distribution (middle panel) of the few clusters occurring in the footpoint regions, and the corresponding representative spectral profiles (RSP; right panel); the *k*-means analysis is run on the whole time series and it produces a single set of RSPs). The RSPs present a variety of properties including broad blueshifted (cluster 31; purple) and redshifted profiles (e.g., clusters 7, 14, 43, 50).

increase significantly. We note that for similar events observed with *IRIS* (e.g., Testa et al. 2014, 2020; Cho et al. 2023) the observed chromospheric and TR spectral profiles significantly change on short timescales of seconds. In light of this, the relatively modest cadence of these CHROMIS data might not provide us with a comprehensive view of the spectral evolution at the loops footpoints. The temporal evolution of the Ca II K spectra in the spatial locations where the highest intensities are observed appear to generally follow a progression from broad profiles with largest redshifts at the peak intensity to progressively less redshifted profiles (i.e., red to orange/yellow/green, in terms of the RSPs shown in Figure 5). Fig. 7 shows that, as the event progresses, the ribbon, especially the southern portion, advances mostly in the north direction. As new locations in the lower atmosphere get brighter they tend to be characterized initially by blueshifted and narrow Ca II K profiles, and then evolve to brighter, broader and more redshifted profiles. This observed evolution of the spectral profiles could be due to the change in the plasma conditions in a magnetic strand, where increasing density and temperature as a consequence of the heating cause a different response to the heating properties, and/or could point to different heating properties during the events, with harder non-thermal electron distributions in newly reconnected lines evolving in time to softer distributions.

In the above *k*-means clustering analysis applied to the *SST* field of view which includes both ribbon and

non-ribbon emission, only a few clusters describe the ribbon spectra (see Figure 6). Therefore, in order to refine our analysis of the specific spectral features of the flare profiles, we run a *k*-means analysis on a subset mostly comprised of spectral profiles from the flare ribbon. We used a reduced data set that covers 550 pixels in *x* and 500 pixels in *y* centered on the flare ribbon, including the 82 time steps. To find the profiles covering the flare, we sampled all profiles with maximum intensity above 1565 in arbitrary intensity units (see contours in Figure 10). This value was found by exploring different thresholds and see how adjusting it affected the clustering of flare profiles. We also included profiles from outside the ribbon, creating a total sample of 94823 profiles, where 62% are flare profiles and 38% are profiles sampled in the surroundings but outside the flare. We set the number of clusters to 36 in order to capture more details of the profiles, as well as to make sure that specific features end up in less populated clusters. The *k*-means algorithm was applied to the training data set, and the output was used to predict the closest RSPs for each profile in this reduced data set.

Figure 8 shows an overview of the 36 clusters. We applied a Gaussian fit to the RSPs in order to calculate their Doppler shifts and used these values to order the clusters according to their Doppler shift. The number of redshifted RSPs is significantly higher than the blueshifted RSPs. In addition, the Doppler shifts to the red generally have higher values. Because of this, we

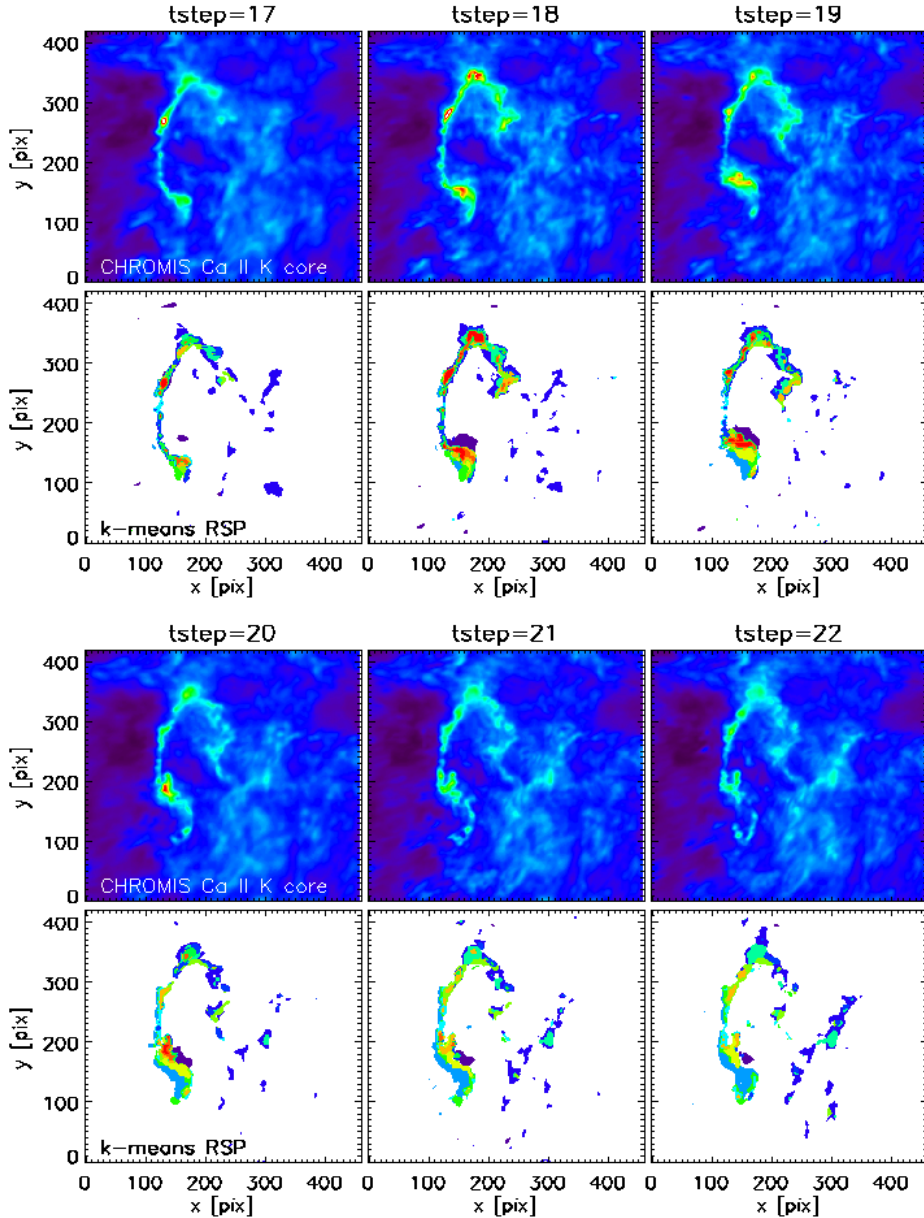


Figure 7. Results of the k -means clustering analysis allow to investigate the spatial and temporal evolution of the spectral properties of the chromospheric brightenings. Here we show, for six consecutive time steps (about 22 s apart) during the brightenings (the intensity in the Ca II K line core is shown in the top panels for each time step), the spatial distribution (bottom panels for each time step) of the few clusters occurring in the footpoint regions, corresponding to the representative spectral profiles shown in Figure 6 (right panel).

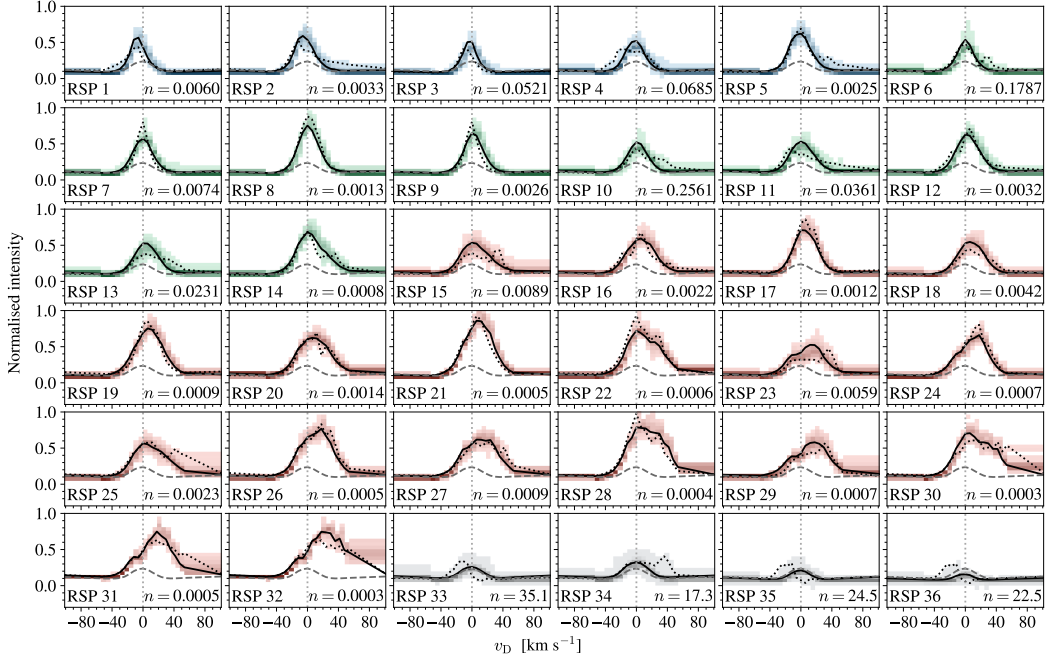


Figure 8. Thirty-six RSPs from the k -means clustering of the Ca II K line profiles from a reduced data set focused on the ribbon (see also Figure 10). Each panel shows the RSPs (solid black), the average profile in the reduced data (dashed gray), and the Ca II K profile that have the largest Euclidean distance to the RSP (dotted black). All profiles have been normalised from the lowest to the highest intensity of the reduced data set. The panels include the density distribution of all profiles within a cluster, where darker color indicates higher density. The color of the density distributions in RSPs 1–32 also represent the Doppler shift of the RSPs to indicate blueshifts (blue), redshifts (red), and weak to no shifts (green). RSPs 33–36 are clusters of profiles outside the flare ribbon, and the gray shading is the density distribution of all profiles in the clusters. RSPs 1–32 are sorted by the Doppler shift of the Gaussian profiles that were fitted to the RSPs, and RSPs 33–36 are placed at the end of the sorting. n represents the number of profiles in a cluster as a percentage of the total amount of profiles in the reduced data set ($\sim 2.25 \times 10^7$ profiles).

set two different thresholds on the RSPs characterized by redshifts and blueshifts: $+5 \text{ km s}^{-1}$ and -1 km s^{-1} , respectively (see red and blue dashed lines in Figure 9). Following these thresholds, Figure 8 shows that RSPs 1–5 are shifted to the blue, RSPs 6–14 have weak to no Doppler shifts, and RSPs 15–32 are shifted to the red. RSPs 33–36 are large clusters containing the profiles from outside the ribbon, and their respective RSPs have 0 km s^{-1} Doppler shift. We note that the profiles in the latter clusters are only used as a reference and are not included in the rest of the analysis, hence the corresponding RSPs are placed at the end of the sorting. The figure shows that the k -means clustering is able to identify and properly cluster specific features. This is seen from the density distributions, showing that the

majority of profiles in each cluster are centered around or close to the RSPs.

Figure 9 shows two scatter plots between the Doppler shift and RSP line core widths (left) and the Doppler shift and maximum intensity of the RSPs (right). The color of the ellipses follows the respective Doppler shift of the RSPs. The vertical radii of the ellipses in the left panel is proportional to the maximum intensity of the RSPs, while the horizontal radii of the ellipses in the right panel is proportional to the width of the RSP line cores. The left panel shows that there is a correlation between the Doppler shift and the line core width, where larger Doppler shifts mostly result in broadening of the line cores. This is also clearly seen from the horizontal radii of the ellipses in the right panel. This panel also

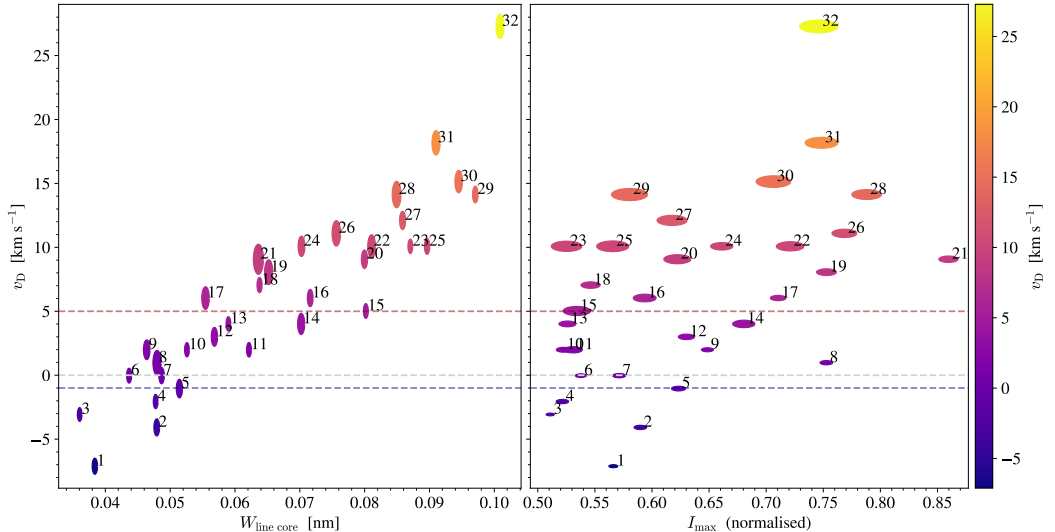


Figure 9. Scatter plots between the Doppler shift and RSP line core widths (left), and Doppler shift and maximum intensity of the RSPs (right). The points are marked with their respective RSP index (see Figure 8), and colored based on their Doppler shift. The vertical radii of the ellipses in the left figure reflect the magnitude of the maximum intensity of the RSPs, while the horizontal radii in the right figure represent the RSP line core widths. The red dashed line at $+5 \text{ km s}^{-1}$ and blue dashed line at -1 km s^{-1} indicate the boundaries for the RSP sorting.

shows that the maximum intensity of the RSPs is not strongly correlated to the Doppler shift.

The Doppler shift of the flare profiles is further explored in Figure 10, showing intensity maps of the *SST*/CHROMIS Ca II K line core at six consecutive time steps during the flare. While the top panels of each time step are overplotted with contours marking the threshold for the *k*-means training sampling, the bottom panels show the Doppler shift of every profile in RSPs 1–32. The results are similar to those found in Figure 7, where blueshifted profiles are exclusively found in low-intensity areas in the lower part of the ribbon and are not present until $t = 19$. The most redshifted profiles (RSPs 31 and 32) only occur at $t = 18$ in the top part of the ribbon. Even though the profiles in these clusters exhibit the strongest redshifts, they are generally not the most intense profiles found in the flare. While there indeed are a few profiles in these clusters with high intensity (see density distribution in Figure 8), RSP 21 contains profiles with significantly higher intensities but much lower Doppler shifts (approximately $+9 \text{ km s}^{-1}$). This cluster is also a clear outlier in the right panel in Figure 9. We generally see that the regions with high Ca II K intensity are characterized by redshifted profiles, but we note that there are still lower-intensity regions with profiles that are significantly redshifted and broadened (for ex-

ample RSPs 23, 25, 27, and 29) as well as high-intensity regions with profiles that are less redshifted and not as broad (for example RSPs 8, 17, 19, and 21).

3.4. *IRIS* and *SST* Spectra

IRIS can provide additional chromospheric and TR diagnostics. Although the brightest portion of the ribbon-like region is unfortunately not under the *IRIS* slit, the slit crosses a weaker portion of the ribbon, where we can analyze the *IRIS* and CHROMIS spectral profiles. In Figure 11 we highlight this weak ribbon region by showing base difference and running difference *IRIS* SJI time series: for the base difference we subtract the initial emission (we chose 2016-09-04T08:19:35 as reference time), whereas for the running difference we subtract the image of the immediately preceding time step. These figures show the presence of a “tail” of the ribbon extending from $(x,y) \approx (-387'', 22'')$ to $(x,y) \approx (-382'', 18'')$, where the latter is in the *IRIS* spectrograph f.o.v. Another location under the *IRIS* slit, around $(x,y) \sim (-382'', 17'')$, is also undergoing short-lived brightenings a couple of minutes earlier, and appears to be associated with the early brightening of the shorter coronal loops (see left panel of Figure 3). In Figure 12 we show the timeseries of the spectral profiles in some of the strongest *IRIS* TR and chromospheric lines,

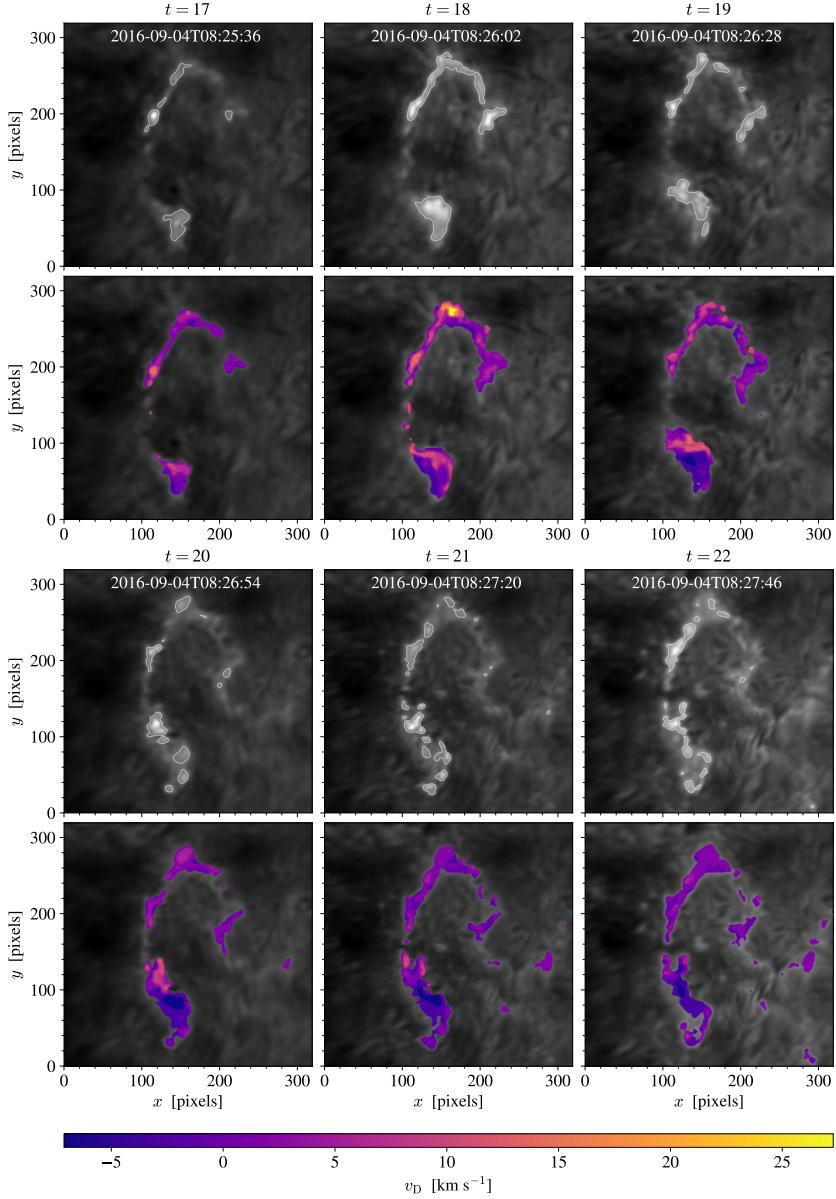


Figure 10. Intensity maps of the SST/CHROMIS Ca II K line core for six consecutive time steps during the flare. The contours in the top panels of each time step show the threshold (contours) used for the sampling of the k -means training data, for the analysis focused on the ribbon spectra. In the bottom panels of each time step we overplot, on the intensity maps, the map of Doppler shift of the RSPs (clusters 1–32 shown in Figure 8). The f.o.v. has been reduced to mostly cover the ribbon.

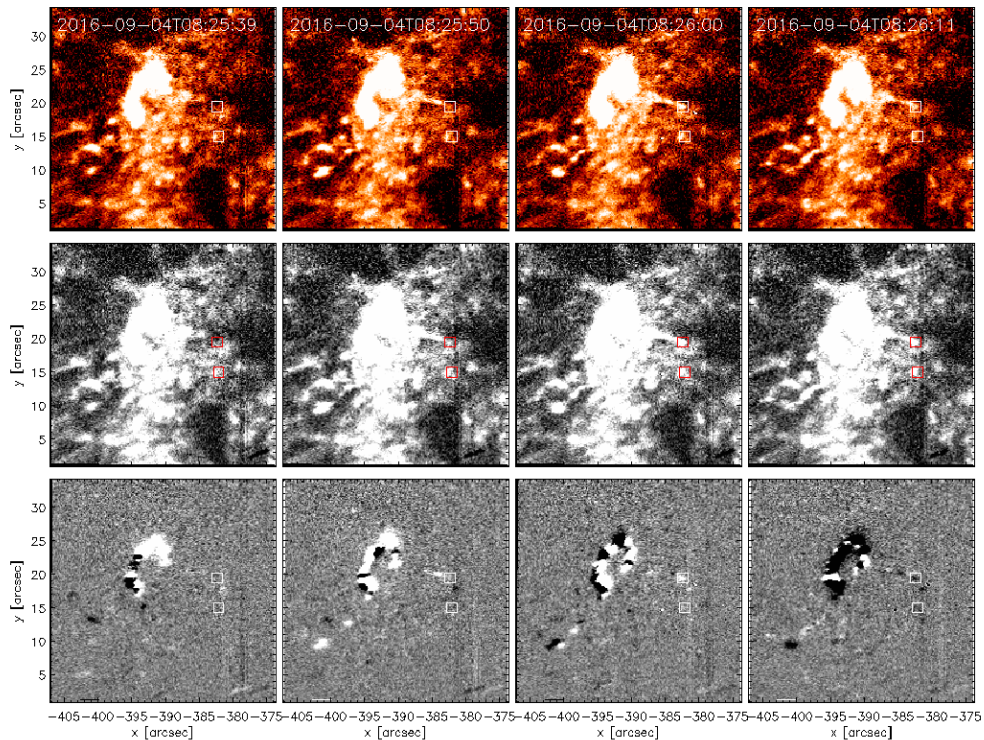


Figure 11. *IRIS* SJI time series around a time when part of the ribbon is under the *IRIS* slit. From top to bottom: *IRIS* 1400Å SJI emission (top); base difference (i.e., the emission subtracted of the image at a reference time, which we chose to be 2016-09-04T08:19:35; middle); and running difference (i.e., the difference between the current SJI image and the SJI image from the immediately preceding time step; bottom). The two squares indicate the position for which we show the *IRIS* and CHROMIS Ca II spectra in Figure 12 (for better contrast we use a red color for the boxes in the middle panels). The emission of the ribbon is quite weak at those locations, motivating the saturated color scales we used in the plots of this figure to highlight their emission as much as possible.

and in the CHROMIS Ca II K, for these two locations (note that we average the *IRIS* spectra over 3 *IRIS* pixels along the y axis to improve the signal-to-noise). The earlier brightening (bottom row of Figure 12, and southernmost square marked in Figure 11) shows: (1) a significant increase in the Si IV TR emission lasting about a minute and characterized by a blueshift of $\sim 20\text{km s}^{-1}$ (relative to the pre-event spectrum), and a broad (multi-peaked) profile with a small red tail; (2) a very modest increase in C II emission; (3) modest increase in chromospheric Mg II emission, which is mostly characterized by limited central reversal, and a blue peak slightly more pronounced than the red peak; (4) the CHROMIS Ca II K profiles are similar to the profiles observed in the regions of the main ribbon with weaker emission, i.e., they

are single peaked, narrow, and with modest Doppler shift (e.g., RSPs 17, 36 of Figures 5 and 6, or RSPs 7–13 of Figure 8 and 9). The second brightening, in the weak “tail” of the ribbon, (top row of Figure 12, and northernmost square marked in Figure 11), is slightly longer lasting (about a couple of minutes), and it shows: (1) Si IV emission without significant Doppler shift with respect to the pre-event profile (but redshifted in absolute terms), (2) C II emission with relative increase, with respect to the pre-event profile, comparable to the Si IV emission; (3) the chromospheric Mg II and Ca II emission are similar to the other brightening, with largely single-peaked profiles and CHROMIS Ca II K profiles similar to the weaker ribbon regions. For both brightenings there is no significant Mg II triplet emission detected. In

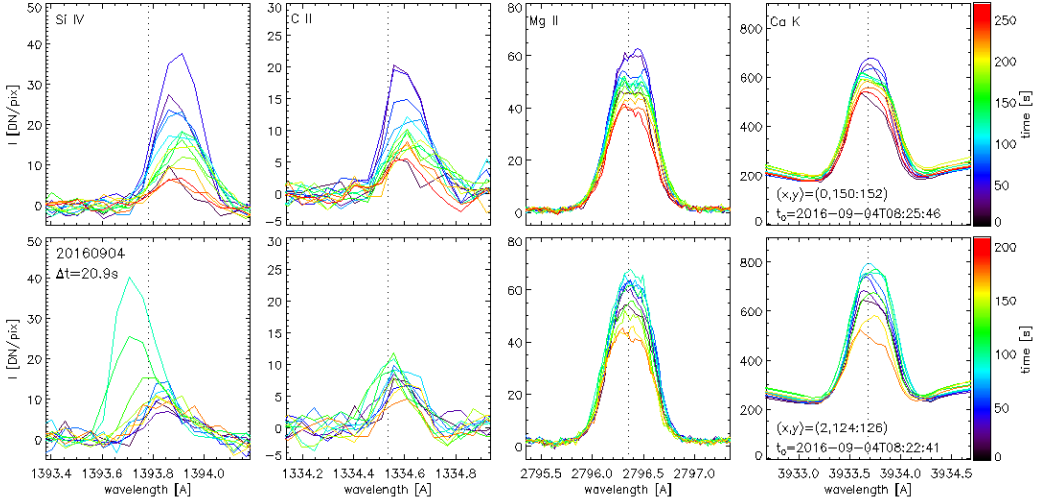


Figure 12. Temporal evolution of the spectral emission in *IRIS* TR and chromospheric lines and in the *SST/CHROMIS* Ca II K line (from left to right: Si IV 1393Å, C II 1334Å, Mg II 2796Å, Ca II 3934Å) for two locations (one in each row) where faint part of the ribbons is under the *IRIS* slit. For the *CHROMIS* Ca II spectra we use 3933.684Å as a reference wavelength (see section 2 for details). The top and bottom row correspond respectively to the northernmost and southernmost boxes of Figure 11. Note that the two time series have different timescales (see colorbars to the right) and start time (t_0 is noted in the right plot).

the following subsection (Section 3.5) we will compare the observed profiles with predictions from 1D RADYN models of impulsively heated loops.

3.5. Comparison with Numerical Simulations

Numerical simulations can provide a great deal of insight when interpreting observations. In previous work (Polito et al. 2018; Testa et al. 2020; Bakke et al. 2022) we used 1D flare simulations to investigate the atmospheric response to heating by nanoflares. Several models were carried out using the RADYN numerical code (Carlsson & Stein 1992, 1995, 1997; Allred et al. 2015), which models plasma magnetically confined in a 1D loop structure, by solving the equation of charge conservation and the level population rate equations. RADYN also solves the non-local thermodynamic equilibrium (non-LTE) radiation transport for H, He, and Ca II which is necessary when modeling chromospheric emission. The RADYN version described in Allred et al. (2015) includes the effect of non-thermal electrons, using the Fokker-Planck equations, and the electron energy distribution is assumed to follow a power-law. Details on the RADYN numerical code and the simulations of nanoflare-heated loops are discussed in Polito et al. (2018). In the following we provide a brief description of the models.

The RADYN simulations of nanoflare-heated loops investigate a broad parameter space including different nanoflare energies, loop-top temperatures, and half-loop lengths. The simulations also include different heating models, such as thermal conduction, electron beam heating with varying low-energy cutoff values E_C , as well as hybrid models of both thermal conduction and electron beams. In Bakke et al. (2022), we focused our efforts on selected models with transport by non-thermal electrons, where the chromospheric lines were synthesized using the RH1.5D radiative transfer code (Uitenbroek 2001; Pereira & Uitenbroek 2015). By comparing the Ca II K, H α , and Ca II 8542Å synthetic spectra from these models to the flare profiles from the observations, we find that the RADYN model most capable of reproducing the observed spectra is the model with 15 Mm half-loop length and initial loop-top temperature of 1 MK. This particular model has a low-energy cutoff value $E_C = 5$ keV (representing an electron beam with low-energy electrons in the distribution), a spectral index $\delta = 7$ for the power-law energy distribution, and total energy $E = 6 \cdot 10^{24}$ erg deposited in the loop. Figure 13 shows the time evolution of Ca II K, H α , and Ca II 8542Å from the RADYN simulation and at three different locations in the flare ribbon, where the latter is given in the top row panels. The locations were chosen

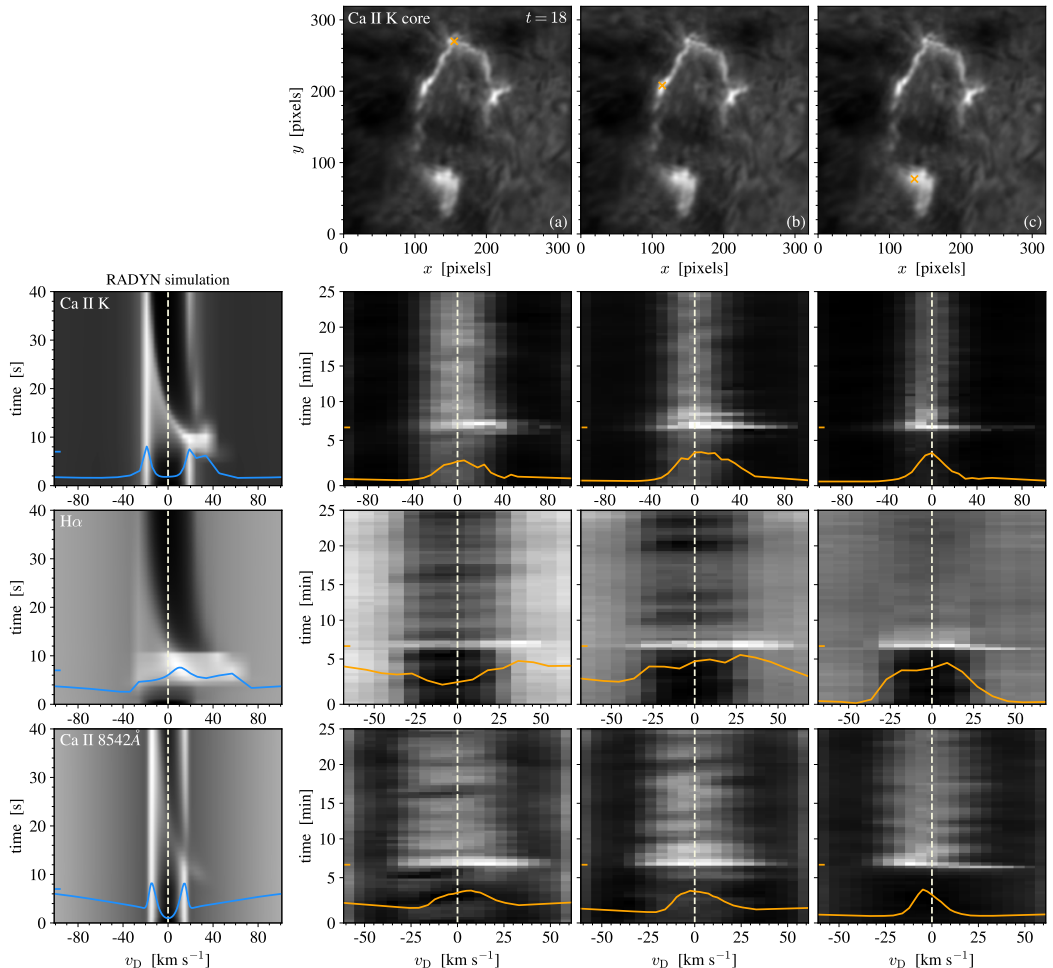


Figure 13. Spectral evolution of Ca II K, H α , and Ca II 8542Å in a RADYN simulation of a nanoflare heated loop and from *SST* observations at different locations in the ribbon. The top panels show intensity maps of the *SST*/CHROMIS Ca II K line core at $t = 18$, where the ribbon locations at which the spectra are taken are marked as orange crosses. Each spectral evolution panel (the three bottom rows) shows the line profile at a time step during the flare phase. For the RADYN simulation, the time step is chosen at 7 s while the line profiles from the observations are chosen at 6.8 min (which is at $t = 18$). These time steps are marked along the y -axis. We note that the scaling of the x -axes varies between the observational datasets.

in order to show the time evolution of the profiles in a region of strong redshifts (panel a), a region of high intensity (panel b), and a region of blueshifts (panel c). We note that there is a discrepancy between the flare time scales of the RADYN simulation and the observation. In the RADYN model, the flare lasts for 10 s, while in the observation the flare lasts for minutes. The RADYN model was originally meant to simulate short-lived (10–

30 s) footpoint brightenings in TR moss as observed with *IRIS* (Testa et al. 2013, 2014, 2020; Cho et al. 2023). Even though the observed flare is a sequence of many short-lived brightenings, it becomes difficult to make a temporal comparison between the profiles because the time between each observed frame is about half the total simulation time. The comparisons made in this work

are therefore focused on the shape and features of the profiles rather than the time scales.

The shape of the RADYN Ca II K and Ca II 8542Å profiles does not resemble that of the observations, especially since the absorption feature of the synthetic spectral lines is not seen in the observed flare profiles. However, the strong redshift of the Ca II K profile is consistent with the observation at the peak of the flare (around 6.8 min) at the the locations marked in panels (a) and (b) of Figure 13. The largest Doppler shift of the Ca II K line observed in the northern part of the ribbon (panel a) is comparable to that of the RADYN simulation, where the lines from both the observation and simulation have components that are redshifted to a value between 30 and 35 km s⁻¹.

H α is the synthetic profile from RADYN that is most similar to the observational profiles. In particular, the H α profile from the location marked in panel (b) has an almost identical shape to the one from RADYN, although with a slightly smaller range of velocity on the red side of the line profile. The evolution of the profiles is also similar, where the initial profiles are in absorption until the flare phase during which both profiles are in emission and characterized by a redshifted component with multiple peaks. In RADYN, the H α profile eventually returns back to being in absorption during the post-heating phase (after 10 s). The heating mechanisms of the actual flare are more complicated, and after the peak of the flare there is still ongoing heating that continuously changes the shape, width, and intensity of the profiles over time. However, at the northern (column a) and central (column b) locations of the ribbon, the profiles seem to slowly revert back into absorption, which is consistent with the simulation. The location in the southern region of the ribbon (column c) shows less variation of the H α intensity and profile features after 8 min compared to the other locations.

The comparison of the *IRIS* spectral properties during the brightenings, with the expectations from RADYN models, can guide us in the interpretation of the observations and how they constrain the heating properties. As discussed at length in previous work (Testa et al. 2014; Polito et al. 2018; Testa et al. 2020), the grid of RADYN simulations of impulsively heated loops that we have carried out, provide diagnostics of the presence of non-thermal particles and their properties. In particular, blueshifts in the Si IV profiles, or Mg II triplet emission, are signatures of accelerated particles. The *IRIS* spectral properties of the earlier brightening are overall reminiscent of model H1 (which is a hybrid model, with half-length of 15 Mm, where half of the energy is transported by thermal conduction and half goes into

nonthermal particles) of Testa et al. (2020), in particular, the multicomponent nature of the Si IV profile with a blueshifted peak, the slightly higher blue peak in the Mg II profiles, and the lack of significant Mg II triplet emission. We can speculate that the *IRIS* profiles, and modest intensities of the brightenings, suggest that the heating is due to a mix of direct heating with thermal conduction and non-thermal particles, characterized by low energy (likely around 5 keV) and total energy and flux likely smaller than in our existing simulations. In fact, as we discussed in Polito et al. (2018), impulsive heating with non-thermal particles can produce Si IV blueshifts for lower energy cutoff values when the total energy is reduced (their Figure 15). As discussed earlier in this section, such a model produces H α profiles also similar to the observed ones. For the second brightening, the spectral profiles do not clearly point to the presence of non-thermal particles, but also for this case some of the observed spectral properties are qualitatively similar to the models with low energy non-thermal electrons ($E_C \sim 5$ keV), in particular in terms of the lack of significant Doppler shift in Si IV and of significant Mg II triplet emission (see also Fig. 2 of Cho et al. 2023).

There are a few caveats to keep in mind when using the RADYN simulations of impulsively heated loops to interpret the observations we are analyzing here. First, these simulations do not reproduce the observed Mg II and Ca II (and often also the C II) profiles, in particularly failing to reproduce the often observed single-peak profiles, as discussed above (and in previous works, such e.g., Testa et al. 2020). The mismatch between modeled and observed chromospheric profiles occurs also in quiescent plasma (e.g., Carlsson et al. 2015; Hansteen et al. 2023), and suggests that the background atmosphere might be a non-negligible cause of the problem. Furthermore, these simulations, as described earlier in this section, were developed to match short-lived brightenings typically observed to last less than one minute, and therefore might not be an ideal comparison for the observations in this paper which have longer duration (~ 2 –4 min) footpoint brightenings. Also, the observations we analyzed have about 21 s cadence (and only ~ 0.5 s exposure time) therefore the temporal sampling is such that it might have missed a crucial initial phase of the brightening(s), including possibly the peak of the emission.

4. DISCUSSION AND CONCLUSIONS

In this paper we have analyzed coordinated imaging and spectroscopic observations of a small heating event in the core of an active region, observed with *IRIS*, *SDO/AIA*, and the *CHROMIS* instrument at *SST*. The

atmospheric response to the heating includes the initial brightening at the footpoints of the coronal loops, visible in the chromospheric and TR emission in *IRIS*, *SST*, and AIA data, and the subsequent brightenings of the coronal loops, first in the hot AIA 131Å (FeXXI) emission, followed by the 94Å (FeXVIII) and other cooler channels during the cooling phase.

The morphology of the hot coronal loops, with sets of transient loops crossing at a significant angle, is reminiscent of what is generally observed in other similar heating events in AR cores (e.g., Testa et al. 2013, 2014; Reale et al. 2019a; Testa et al. 2020; Testa & Reale 2020), suggesting such events might be driven by large-scale photospheric motions or large-scale magnetic flux emergence (see also Asgari-Targhi et al. 2019). The coronal emission points to high temperatures up to ~ 10 MK, analogous to other small heating events in AR cores (see e.g., Brosius et al. 2014; Ishikawa et al. 2017; Ishikawa & Krucker 2019; Reale et al. 2019a,b; Testa et al. 2020; Testa & Reale 2020; Cooper et al. 2021). During the overall heating event, a first set of footpoint brightenings are observed (around 8:24UT) including one location under the *IRIS* slit (bottom row of Figure 12, and southernmost location marked in Figure 11) and the footpoints of a set of short loops (sampled by location A of Figure 3). The brightest chromospheric/TR brightenings are observed about two minutes later at the footpoints of a longer set of loops (sampled by location B of Figure 3), and are well observed by CHROMIS and the *IRIS* SJI (see e.g., Figure 1), while only a weaker tail of this ribbon is observed under the *IRIS* slit (top row of Figure 12, and northernmost location marked in Figure 11).

The simultaneous *IRIS* and CHROMIS observations provide complementary diagnostics of the heating event. This CHROMIS dataset is in particular characterized by exceptional spatial resolution down to ~ 100 km. The spatial analysis of the *SST* observations of the ribbon indicates spatial scales of ~ 150 – 200 km (measured FWHM $\sim 0''.2$ – $0''.3$) for the chromospheric emission. There is a small observed spatial offset ($\sim 0''.2$) between the *SST* chromospheric emission and the TR *IRIS* SJI emission in a direction compatible with the observed geometry, i.e., with the coronal loops extending in the E direction, and therefore the TR also extending to the E of the lower atmospheric emission observed by *SST*, although we cannot completely rule out small misalignment errors (see discussion in Section 3.2). The relative intensity of the TR (*IRIS* SJI 1400Å) to lower chromospheric emission (observed with CHROMIS) is observed to vary over the ribbon, in particular with relatively weaker TR emission close to the two ends of the ribbon

(i.e., S of $y \sim 45$, or W of $x \sim -390$, such as e.g., location C of Figure 4), which suggests (see e.g., Fig. 5, and discussions in Testa et al. 2020) that in those locations the heating and energy transport mechanisms might less efficiently heat the TR, indicating for instance less direct heating and thermal conduction, and/or harder non-thermal electrons, compared to other ribbon locations.

CHROMIS provides simultaneous spectral data in every spatial pixel, and therefore a trove of constraints for the spatial and temporal properties of the heating. In order to more efficiently exploit this information, we applied machine learning methods to the CHROMIS Ca II K data, and in particular k -means clustering analyses which can efficiently sort the observed spectra into groups with similar spectral properties (Representative Spectral Profiles, RSP). This analysis reveals that the chromospheric emission is characterized by spatial and temporal coherence, in turn suggesting spatial and temporal coherence of the heating properties. In particular, in most ribbon locations the Ca II spectra rapidly evolves from initial narrower profiles with modest Doppler shift toward redshifted and broader profiles (see Figures 7 and 10), as the ribbon evolves and moves, mostly northward. This connection between spectral evolution and ribbon motion puts tight constraints on models. The observed spectral evolution can likely be ascribed to either an evolution of the heating properties (e.g., harder non-thermal electron distributions in newly reconnected lines) and/or the evolution of the atmosphere as it gets denser and hotter, in response to the heating. A small fraction of Ca II spectra is blueshifted, and those blueshifted profiles are mostly concentrated in the southern region of the bright ribbon. The blueshifted profiles are generally narrower, and with lower intensities, than the redshifted profiles (see Figure 9). The very interesting correlations between Ca II Doppler shift, line width, and intensity provide valuable constraints for models. If the Doppler shifts of the Ca II spectral profiles are linked to plasma bulk velocities in the lower chromosphere, the correlations between the Doppler shift and line width could indicate a relationship between the plasma flows and the causes of line broadening (e.g., opacity broadening, superposition of plasma flows along the line-of-sight).

For a couple of low brightness ribbon locations, we obtained *IRIS* and CHROMIS spectra that could be used for a more constraining comparison with predictions from RADYN models of impulsively heated loops. For these locations, the Ca II K profiles are similar to what is observed in the low intensity regions of the main ribbon, and in *IRIS* no significant Mg II triplet emission is observed (which would have been a clear signature of

high energy non-thermal particles), and the Mg II spectra show mostly single-peaked profiles. The *IRIS* Si IV and C II emission shows slightly different properties in the two locations, with the earlier brightening showing blueshifted Si IV spectra and small C II enhancement, and the later brightening characterized by no significant Doppler shift change during the heating event and comparable increase of emission in Si IV and C II.

The comparison of these observed spectral properties with the prediction from models generally suggests the presence of low energy non-thermal particles (with low-energy cutoff $\sim 5 - 10$ keV), likely accompanying direct heating in the corona transported by thermal conduction. We note however that the grid of models we are using (Polito et al. 2018; Testa et al. 2020; Bakke et al. 2022) was developed to reproduce observed brightenings with shorter duration (< 1 min) than the ones observed here. Also, as we discussed in detail in Section 3.5, the synthetic profiles from these models generally fail to reproduce some of the chromospheric line shapes, particularly the single-peaked profiles in C II, Mg II and Ca II, so we carried out only a qualitative comparison with the observations (e.g., in terms of Doppler shifts).

Magnetic reconnection is generally accepted to play a significant role in small heating events, especially in the core of active regions. The specific properties of these events, and, for instance, whether they behave like scaled-down versions of larger flares, is highly debated. In this context, the study of accelerated particles in these events can shed light into the nature of the heating mechanisms and of particle acceleration processes as well. Recent works have revealed the presence of accelerated particles in very small heating events, although typically these are characterized by smaller low-energy cutoff and steeper slopes ($E_C \sim 5-15$ keV, $\delta \gtrsim 7$) compared with larger flares (e.g., Hannah et al. 2008; Testa et al. 2014; Wright et al. 2017; Testa et al. 2020; Glesener et al. 2020; Cooper et al. 2021; see also review of Testa & Reale 2022, and references therein). These findings were based on diagnostics from direct detection of non-thermal particle emission at hard X-ray wavelengths (e.g., with RHESSI, FOXSI, NuSTAR; Lin et al. 2002; Glesener et al. 2016; Harrison et al. 2013), or spectral diagnostics from the indirect detection of the effect of non-thermal particles in the lower atmosphere where they can deposit most of their energy (e.g., with *IRIS*, and with ground-based data such as the *SST* data analyzed here). Recent work by Polito et al. (2023) presented rare simultaneous observations with *IRIS* and NuSTAR, which provided independent diagnostics of non-thermal particles and found concordant results from both ap-

proaches. Also in this latter case the non-thermal particle distribution was characterized by relatively low energies ($E_C \sim 8$ keV) and steep slopes, analogous to the properties of the heating event we studied here, as inferred from the comparison of *IRIS* and *SST* spectra with RADYN simulations.

The observations analyzed here put tight constraints on the models, but also highlight the shortcomings of the models. In fact, although they provide a good match for the observed TR Si IV profiles (and occasionally reproduce some chromospheric spectral profiles, such as the H α case discussed in Section 3.5), they generally fail at producing chromospheric spectral line shapes similar to the observations as also discussed in previous work (e.g., Polito et al. 2018; Testa et al. 2020; Cho et al. 2023). We note that these discrepancies between models and observed profiles occur also in quiescent atmosphere (see e.g., Hansteen et al. 2023, and references therein). A necessary next step is therefore to investigate in detail the cause of these discrepancies and improve the model to remediate them, and allow us to fully exploit these diagnostics.

We thank the referee for a careful review of the paper and several suggestions that have helped improve the paper. PT is funded for this work by contracts 8100002705 (*IRIS*), and NASA contract NNM07AB07C (*Hinode*/XRT) to the Smithsonian Astrophysical Observatory, and by NASA grant 80NSSC20K1272. BDP is supported by NASA contract NNG09FA40C (*IRIS*). This research has made use of NASA's Astrophysics Data System and of the SolarSoft package for IDL. *SDO* data were obtained courtesy of NASA/*SDO* and the AIA and HMI science teams. *IRIS* is a NASA small explorer mission developed and operated by LMSAL with mission operations executed at NASA Ames Research Center and major contributions to downlink communications funded by ESA and the Norwegian Space Centre. The Swedish 1-m Solar Telescope is operated on the island of La Palma by the Institute for Solar Physics of Stockholm University in the Spanish Observatorio del Roque de los Muchachos of the Instituto de Astrofísica de Canarias. The Institute for Solar Physics is supported by a grant for research infrastructures of national importance from the Swedish Research Council (registration number 2021-00169). This research is supported by the Research Council of Norway, project numbers 250810, 325491, and through its Centres of Excellence scheme, project number 262622.

REFERENCES

- Allred, J., Kowalski, A., & Carlsson, M. 2015, in AAS/AGU Triennial Earth-Sun Summit, Vol. 1, AAS/AGU Triennial Earth-Sun Summit, 302-07
- Antiochos, S. K., Karpen, J. T., DeLuca, E. E., Golub, L., & Hamilton, P. 2003, *ApJ*, 590, 547
- Arthur, D., & Vassilvitskii, S. 2007, in Proceedings of the eighteenth annual ACM-SIAM symposium on Discrete algorithms, Society for Industrial and Applied Mathematics, 1027–1035
- Asgari-Targhi, M., van Ballegoijen, A. A., & Davey, A. R. 2019, *ApJ*, 881, 107
- Bakke, H., Carlsson, M., Rouppe van der Voort, L., et al. 2022, *A&A*, 659, A186
- Berger, T. E., De Pontieu, B., Schrijver, C. J., & Title, A. M. 1999, *ApJL*, 519, L97
- Boerner, P., Edwards, C., Lemen, J., et al. 2012, *SoPh*, 275, 41
- Boerner, P. F., Testa, P., Warren, H., Weber, M. A., & Schrijver, C. J. 2014, *SoPh*, 289, 2377
- Bose, S., Henriques, V. M. J., Joshi, J., & Rouppe van der Voort, L. 2019, *A&A*, 631, L5
- Brooks, D. H., Warren, H. P., Williams, D. R., & Watanabe, T. 2009, *ApJ*, 705, 1522
- Brosius, J. W., Daw, A. N., & Rabin, D. M. 2014, *ApJ*, 790, 112
- Carlsson, M., Leenaarts, J., & De Pontieu, B. 2015, *ApJL*, 809, L30
- Carlsson, M., & Stein, R. F. 1992, *ApJL*, 397, L59
- . 1995, *ApJL*, 440, L29
- . 1997, *ApJ*, 481, 500
- Cho, K., Testa, P., De Pontieu, B., & Polito, V. 2023, *ApJ*, 945, 143
- Cooper, K., Hannah, I. G., Grefenstette, B. W., et al. 2021, *MNRAS*, 507, 3936
- de la Cruz Rodríguez, J., Löfdahl, M. G., Sütterlin, P., Hillberg, T., & Rouppe van der Voort, L. 2015, *A&A*, 573, A40
- De Pontieu, B., Title, A. M., Lemen, J. R., et al. 2014, *SoPh*, 289, 2733
- Everitt, B. 1972, *The British Journal of Psychiatry*, 120, 143
- Fletcher, L., & De Pontieu, B. 1999, *ApJL*, 520, L135
- Glesener, L., Krucker, S., Christe, S., et al. 2016, in Society of Photo-Optical Instrumentation Engineers (SPIE) Conference Series, Vol. 9905, Space Telescopes and Instrumentation 2016: Ultraviolet to Gamma Ray, ed. J.-W. A. den Herder, T. Takahashi, & M. Bautz, 99050E
- Glesener, L., Krucker, S., Duncan, J., et al. 2020, *ApJL*, 891, L34
- Hannah, I. G., Christe, S., Krucker, S., et al. 2008, *ApJ*, 677, 704
- Hansteen, V. H., Martinez-Sykora, J., Carlsson, M., et al. 2023, *ApJ*, 944, 131
- Harrison, F. A., Craig, W. W., Christensen, F. E., et al. 2013, *ApJ*, 770, 103
- Ishikawa, S.-n., Glesener, L., Krucker, S., et al. 2017, *Nature Astronomy*, 1, 771
- Ishikawa, S.-n., & Krucker, S. 2019, *ApJ*, 876, 111
- Klimchuk, J. A. 2006, *SoPh*, 234, 41
- . 2015, *Philosophical Transactions of the Royal Society of London Series A*, 373, 20140256
- Kobayashi, K., Cirtain, J., Winebarger, A. R., et al. 2014, *SoPh*, 289, 4393
- Lemen, J. R., Title, A. M., Akin, D. J., et al. 2012, *SoPh*, 275, 17
- Lin, R. P., Dennis, B. R., Hurford, G. J., et al. 2002, *SoPh*, 210, 3
- Löfdahl, M. G., Hillberg, T., de la Cruz Rodríguez, J., et al. 2021, *A&A*, 653, A68
- Martens, P. C. H., Kankelborg, C. C., & Berger, T. E. 2000, *ApJ*, 537, 471
- Neckel, H. 1999, *SoPh*, 184, 421
- Panos, B., Kleint, L., Huwlyer, C., et al. 2018, *ApJ*, 861, 62
- Pereira, T. M. D., & Uitenbroek, H. 2015, *A&A*, 574, A3
- Peres, G., Reale, F., & Golub, L. 1994, *ApJ*, 422, 412
- Pesnell, W. D., Thompson, B. J., & Chamberlin, P. C. 2012, *SoPh*, 275, 3
- Polito, V., Peterson, M., Glesener, L., et al. 2023, *Frontiers in Astronomy and Space Sciences*, submitted
- Polito, V., Testa, P., Allred, J., et al. 2018, *ApJ*, 856, 178
- Reale, F. 2014, *Living Reviews in Solar Physics*, 11, 4
- Reale, F., Testa, P., Petralia, A., & Graham, D. R. 2019a, *ApJ*, 882, 7
- Reale, F., Testa, P., Petralia, A., & Kolotkov, D. Y. 2019b, *ApJ*, 884, 131
- Rouppe van der Voort, L., De Pontieu, B., Scharmer, G. B., et al. 2017, *ApJL*, 851, L6
- Rouppe van der Voort, L. H. M., De Pontieu, B., Carlsson, M., et al. 2020, *A&A*, 641, A146
- Scharmer, G. 2017, in *SOLARNET IV: The Physics of the Sun from the Interior to the Outer Atmosphere*, 85
- Scharmer, G. B., Bjelksjo, K., Korhonen, T. K., Lindberg, B., & Petterson, B. 2003a, in *Society of Photo-Optical Instrumentation Engineers (SPIE) Conference Series*, Vol. 4853, Innovative Telescopes and Instrumentation for Solar Astrophysics, ed. S. L. Keil & S. V. Avakyan, 341–350

- Scharmer, G. B., Dettori, P. M., Lofdahl, M. G., & Shand, M. 2003b, in *Society of Photo-Optical Instrumentation Engineers (SPIE) Conference Series*, Vol. 4853, *Innovative Telescopes and Instrumentation for Solar Astrophysics*, ed. S. L. Keil & S. V. Avakyan, 370–380
- Scharmer, G. B., Narayan, G., Hillberg, T., et al. 2008, *ApJL*, 689, L69
- Testa, P., Polito, V., & Pontieu, B. D. 2020, *ApJ*, 889, 124
- Testa, P., & Reale, F. 2020, *ApJ*, 902, 31
- . 2022, arXiv e-prints, arXiv:2206.03530
- Testa, P., De Pontieu, B., Martínez-Sykora, J., et al. 2013, *ApJL*, 770, L1
- Testa, P., De Pontieu, B., Allred, J., et al. 2014, *Science*, 346, B315
- Tripathi, D., Mason, H. E., Del Zanna, G., & Young, P. R. 2010, *A&A*, 518, A42
- Uitenbroek, H. 2001, *ApJ*, 557, 389
- van Noort, M., Rouppe van der Voort, L., & Löfdahl, M. G. 2005, *SoPh*, 228, 191
- Vissers, G. J. M., de la Cruz Rodríguez, J., Libbrecht, T., et al. 2019, *A&A*, 627, A101
- Wright, P. J., Hannah, I. G., Grefenstette, B. W., et al. 2017, *ApJ*, 844, 132

